DOCTORAL THESIS
2019

DYNAMICS OF POSIDONIA OCEANICA MEADOWS

Daniel Ruiz-Reynés

DOCTORAL THESIS
2019

Doctoral Program in Physics

DYNAMICS OF POSIDONIA OCEANICA MEADOWS

Daniel Ruiz-Reynés

Director: Dr. Damià Gomila
Tutor: Prof. Dr. Emilio Hernández-García

Doctor by the Universitat de les Illes Balears

Dr. Damià Gomila Villalonga, Científico Titular at IFISC (CSIC-UIB),

I DECLARE

That the thesis entitled "DYNAMICS OF POSIDONIA MEADOWS", presented by Daniel Ruiz Reynés to obtain a doctoral degree, has been completed under my supervision and meets the requirements for an International Doctorate.
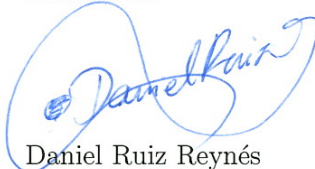
Palma de Mallorca, Monday 11th November, 2019.

Director:

Dr. Damià Gomila Villalonga

Candidate:

Daniel Ruiz Reynés

Time is finite, knowledge... Who knows

Abstract

In this thesis we study the dynamics of vegetation patterns in *Posidonia oceanica* meadows. The first introductory chapter presents a review of vegetation patterns in different ecosystems, the methodologies used in the literature to study each case, and the previous works of *Posidonia oceanica* with implications in the description of the meadows growth.

In the second chapter of the thesis, based on previous knowledge of clonal-growth plants, we develop a coarse grained model that describes the evolution of the meadows. We show that long-range competition is the mechanism responsible for the formation of patterns and we are able to infer the interaction distance. The model allows to reproduce the spatial features of vegetation approaching to the coast, where mortality increases. Additionally, we study the relevance of the dependence on the angle of the model in the spatiotemporal dynamics. We conclude that the density of apices in different directions of growth homogenizes with time, only being enhanced those particular directions growing at the front facing outwards the meadow.

The third chapter presents a systematic derivation of a simplified equation from the original model, reducing substantially the difficulty of the problem. We discuss the different approximations made and the validity of the equations derived.

The fourth chapter focuses on an intermediate equation obtained from the derivation, that provides quantitative agreement with the original model. We study in detail its bifurcation diagram characterizing different patterns and localized structures. In the last part of this chapter we study the dynamics of vegetation fronts in the simplest one dimensional case.

The last chapter tries to determine if the presence of hydrogen sulfide in the sediment, result of the spreading of organic matter due to water movement that later decomposes, is a valid long-range competition mechanism able to explain the formation of patterns. We conclude that patterns form as a result of this interaction. Furthermore, the model predicts an oscillatory instability of the homogeneous solution which creates a very rich phase diagram with different dynamical behaviors still to explore.

Resumen

En esta tesis se desarrolla el estudio de la dinámica de los patrones de vegetación en las praderas de *Posidonia oceanica*. El primer capítulo presenta diferentes casos de formación de patrones de vegetación en diferentes ecosistemas, las metodologías utilizadas para el estudio de dichos patrones y de forma más concreta se presentan los trabajos sobre *Posidonia oceanica* relevantes para el crecimiento de la pradera. El segundo capítulo, se basa en el conocimiento previo sobre plantas clonales para desarrollar un modelo continuo que describe la evolución del crecimiento de la pradera. En este se muestra que el mecanismo necesario para la formación de patrones es la competición de largo alcance. Además, el modelo reproduce las características principales de las praderas a medida que nos acercamos a la costa. En la última parte del capítulo estudiamos la relevancia que tiene la dependencia con el ángulo de crecimiento para la dinámica espacial. Se concluye que la densidad de ápices creciendo en diferentes direcciones tiende a homogeneizarse con el tiempo, de tal forma que solo en los bordes de la pradera hay más plantas creciendo hacia fuera que hacia dentro de la misma. El tercer capítulo presenta la derivación de una ecuación sin dependencia angular a partir del modelo original reduciendo sustancialmente la dificultad del problema. Seguidamente se analizan las aproximaciones y la validez de las ecuaciones derivadas. En el capítulo cuatro se analiza con más detalle una ecuación intermedia de la derivación del capítulo anterior, la cual proporciona resultados cuantitativamente similares al modelo original. La última parte del capítulo se centra en el estudio de frentes de vegetación en la versión unidimensional del modelo. Finalmente, en el último capítulo se intenta determinar si la presencia de sulfuro de hidrógeno en el sedimento, resultado de la difusión de materia orgánica más tarde descompuesta, es un mecanismo válido para explicar la formación de patrones. Concluimos que este mecanismo puede generar patrones de vegetación pero además el modelo predice que la vegetación homogénea es susceptible a desarrollar oscilaciones temporales, dando lugar a nuevos regímenes dinámicos que explorar.

Resum

Aquesta tesi conté l'estudi de la dinàmica de patrons de vegetació a les praderes de *Posidonia oceanica*. El primer capítol presenta diferents casos de formació de patrons de vegetació a diferents ecosistemes, les metodologies emprades per l'estudi d'aquests patrons i els treballs sobre *Posidonia oceanica* directament relacionats amb el creixement de les praderes. El segon capítol, es basa en el coneixement previ sobre plantes clonals per desenvolupar un model continu que descriu l'evolució de la pradera. A continuació es mostra que el mecanisme necessari per a la formació de patrons de vegetació és la competició a llargues distàncies. A més el model és capaç de reproduir les característiques principals de les praderes a mesura que ens aproximem a la costa. La darrera part del capítol intenta clarificar el paper que té la dependència del model amb la direcció de creixement en la dinàmica espacial. Essencialment s'arriba a la conclusió que la densitat en diferents direccions tendeix a homogeneïtzar-se amb el temps, de tal manera que només als límits de la pradera hi ha més plantes creixent cap a l'exterior de la pradera que cap a l'interior. El tercer capítol presenta la derivació d'una equació simplificada sense dependència en la direcció de creixement a partir del model original reduint substancialment la dificultat del problema. Seguidament s'analitzen les aproximacions realitzades i la validesa de l'equació derivada. El quart capítol està dedicat a una anàlisi més detallat d'una equació intermèdia de la derivació del capítol previ que proporciona resultats quantitativament similars al model original. La darrera part es centra en l'estudi de la propagació de fronts de vegetació en la versió unidimensional del model. Finalment el darrer capítol pretén determinar si la presència de sulfur d'hidrogen en el sediment, resultat de la difusió de matèria orgànica més tard descomposta, és un mecanisme vàlid que explica la formació de patrons. Es conclou que aquest mecanisme és compatible amb la formació de patrons i a més preveu que la pradera homogènia és susceptible a desestabilitzar i desenvolupar oscil·lacions temporals les quals són l'origen de nous règims dinàmics encara per explorar.

List of publications

- Daniel Ruiz-Reynés, Damià Gomila, Tomàs Sintes, Emilio Hernández-García, Núria Marbà and Carlos M. Duarte. Fairy circle landscapes under the sea. Science Advances, 3(8):e1603262, 2017.

- Daniel Ruiz-Reynés, and Damià Gomila. Distribution of growth directions in meadows of clonal plants. To appear in Physical Review E.

- Daniel Ruiz-Reynés, Francesca Schönsberg, Emilio Hernández-García and Damià Gomila. A simple model for pattern formation in clonal-growth plants. Submitted to Physical Review Letters.

- Daniel Ruiz-Reynés, Luis Martin, Emilio Hernández-García, Damià Gomila and Edgar Knobloch. Vegetation dynamics in a simplified model of clonal growth. In preparation.

- Daniel Ruiz-Reynés, Damià Gomila, Tomàs Sintes, Emilio Hernández-García, Núria Marbà and Carlos M. Duarte. Sulfide concentration as a mechanism for pattern formation in seagrass ecosystems. In preparation.

Acknowledgements

At the end of the class of Statistical mechanics Maxi San Miguel said to me, there is no future outside IFISC. I do not know if he was right, but he certainly made me take the right decision and I am very thankful for that. To all the people that contribute to this project, I want to express them my gratitude, which for a young physicist was light in the darkness.

I want to thank the teachers of the master because along this time I felt I was prepared. I also want to give thanks to all my colleagues of the master and of S07 from which I have enjoyed and learned a lot. A special thanks to Antònia, Rubén and Edu, without their technical support this thesis will not be what it is. They have taught me to compute faster, more efficiently and many interesting things about computers.

I really appreciate fruitful discussions with Dr. Pedro Parra-Rivas, Dr. Tomàs Sintes, Dr. Núria Marbà and Prof. Emilio Hernández-García from which I have many things still to learn. I really hope our collaboration lasts for many years.

Thanks to Prof. Edgar Knobloch for receiving me at the University of Berkeley, where I had a very enriching experience which I will never forget.

Thanks Damià, you have taught me, you have advised me and the most important, you have given me the motivation to overcome the challenges I found, to be better and more capable.

I want to dedicate this thesis to my friends and family, who have been there giving me support. Especially to my little sister for being with me since my childhood. To my father for teaching me the value of hard work. To my mother for transmitting me the patience and the love for maths. And finally to Neus, the most important person in my life, who is with me all the time and helps me when the sun does not shine.

Contents

Introduction

The emergence of order in nature is a puzzling phenomenon that immediately captures the attention of the observer. Non equilibrium is the key to understand a process that seems to violate the second law of thermodynamics. The work of Alan Turing in the fifties [1] introduced the essential mechanism to provide spatial differentiation. In this way, similar geometrical patterns in very different systems can be understood by the same theoretical framework. Although not all systems are equivalent and the interactions may be specific of each case, pattern formation is a ubiquitous phenomenon, being present from lasers dynamics, chemical reactions, convection in fluids to morphogenesis. Thus, pattern formation is a universal phenomenon that can only be explained as a result of interactions [2, 3].

Vegetation is not an exception. On long time scales vegetation self-organizes driven by different mechanisms in different habitats. Thus, vegetation forms spatial patterns which generally cover large extensions, modifying not only the landscape but the fluxes of nutrients and ecosystem functionality. From this perspective the plants act as ecosystem engineers that modify the fluxes of matter and energy improving the growth conditions and increasing their resilience [4–6]. As a consequence, spatial heterogeneity of vegetation coverage is a key factor in the diagnostic of ecosystem health. In fact, spatial distribution has been proposed as an early indicator of critical thresholds which may lead to sudden losses producing desertification [4, 6, 7]. However, the transition to the desert state can be less abrupt due to the adaptation of the wavelength as the environmental conditions change [8, 9]. One thing is clear, the spatial distribution provides critical information for monitoring desertification processes.

The pronounced effect the spatial redistribution of vegetation can have on the ecosystems may remain unnoticed to the observer on the ground, however, the availability of satellite images in the last decades has produced a drastic improvement of the scientific study of vegetation at the landscape scale, facilitating the analysis and as a way of identifying new ecosystems exhibiting vegetation patterns.

1.1   Terrestrial ecosystems
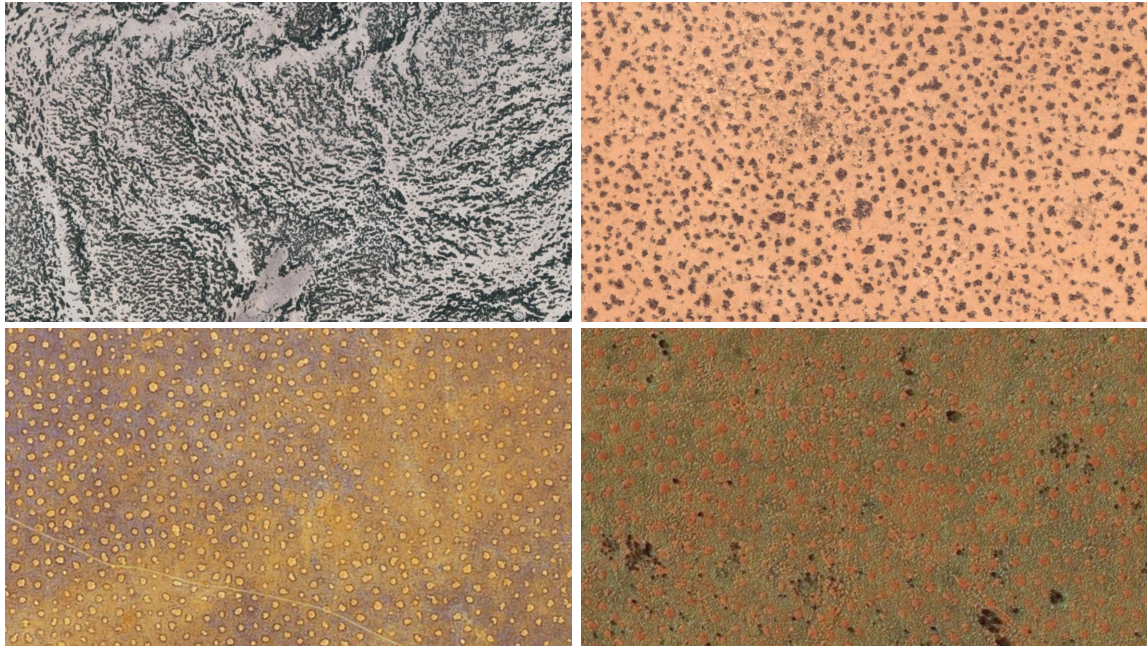
Figure 1.1: Vegetation patterns in arid ecosystems. From left to right top to bottom: Tiger bush in Niger, image from Google maps image (13°07'11.3"N 2°12'41.6"E). Spotted pattern in Sudan, image from Google maps (11°34'57.5"N 27°54'55.8"E. Fairy circles in Namibia, image from ArcGIS Living Atlas (24°57'12.3"S 15°56'12.8"E). Fairy circles in Australia, image from Bing maps (23°27'12.7"S 119°50'57.9"E).

In the last three decades different models have been proposed to explain the origin of extended patterns. One of the first works is the study of tiger bush in Niger. Banded vegetation forms, which adapt its curvature to the terrain morphology, 50 m wide and extending over hundreds of meters to kilometers. The mechanism explaining its formation is based on plant competition by water availability and different approaches have been used to model the evolution of vegetation [10–18]. Some descriptions are simpler, accounting just for vegetation [11] while others describe water and vegetation coevolving simultaneously [13]. Discrete models have also been considered [19], although theoretical work has been more developed for continuous approaches. Not only, theoretical studies have been developed, Fourier analysis of satellite images have been mainly used to characterize the spatial properties of the patterns in relation with climatic variability and anthropogenic pressure [20].

Another important example is formed by different patterns in Sudan [21] where the slope and water availability have a determinant factor in the emergence of each par-

ticular spatial distribution. Gapped, banded, labyrinthine or spotted patterns cover large areas of land. The mechanism is not different from the one in Niger, nevertheless, the emergent patterns are much varied. Mathematically the description is equivalent although different interactions have been considered, some based on second and fourth spatial derivatives which are common in vegetation models. Others are based on integral terms with exponential or Gaussian kernels describing the strength of the interaction. More examples of ecosystems exhibiting pattern forming phenomena have been found around the globe, particularly interesting are those where the spatial distribution adapts to the slope of the terrain and the pattern changes according to the topography [22].

At a very different spatial scale, the same patterns have been shown to appear in water limited ecosystems in the Negev desert [23]. Spatial interactions are described in this case explicitly with water diffusion and plant uptake from the soil creating a positive feedback for regions with vegetation. Reduced infiltration rate due to lack of vegetation is another positive feedback considered as the explanation of long-range interactions [24]. Other alternative explanations have been considered in terms of porous convection [25]. Spatial interactions are the key, although numerous reasons may hinder their identification: Multiple mechanisms may lead to the same effective spatial interaction, different mechanisms can act simultaneously, and the measurement of the interaction is not absent of difficulties, to mention a few. Recently, important scientific discussions about the origin of the well known Namibian fairy circles reached the news. The controversy was precisely about the responsible mechanisms. On one side termite activity was argued to be the responsible of bare circles [26–28] while, other works argue self-organization of vegetation by itself due to competition for water is the responsible mechanism [29–32], mainly because it is the explanation that better explains its dynamic behavior [33] and spatial features of the meadows. Fairy circles in Australia, have been shown to not correlate with termite presence supporting self-organization of vegetation [34].

A common feature of pattern formation is long-range competition mechanisms and the particular sequence of patterns to desertification [35]. According to the theory of pattern formation increasing stressing factors leads homogeneous coverage to develop circular holes arranged in a hexagonal lattice, banded vegetation or stripes, and patches arranged in a hexagonal lattice, which have been claimed as a general path to desertification.

Apart from the fundamental interest in determining the involved mechanisms continuous models have the advantage of being able to predict new behavior. From this perspective vegetation models in arid ecosystems have been widely investigated from the theoretical point of view. Essentially, models allow to investigate the response of the system to different conditions, which allow the identification of critical thresholds or the ranges of parameters in which different spatial distributions are stable,

for example localized structures. Primarily numerical simulations and continuation techniques have been used to determine stationary solutions and its stability against perturbations [15, 36–40]. Other possible applications include for example more applied approaches using time periodic forcing to reproduce seasonal variability [28], secondary instabilities have been shown to reverse desertification [41], response of patterns to environmental change and their resilience features [8, 9] or front propagation of different spatial distributions as recolonization strategy [42].

Totally different from arid ecosystems, peatlands also exhibit large self-organized patterns [43, 44]. Obviously, the mechanisms here are qualitatively different from those acting in arid ecosystems, nevertheless, long-range negative feedbacks are also involved in the spatial arrangements. The spatial distributions are rich, although banded vegetation and holes appear, common patterns exhibit less regular distributions with intricate shapes extending over big areas. Different mechanisms have been hypothesized as the cause of this phenomenon [45–48], peat accumulation in vegetated areas increases acrotelm layer improving local conditions, water ponding by hummocks upslope and nutrient accumulation where vegetation grows are important mechanisms driving self-organization. As a matter of fact, there are different approaches in the literature which account for different mechanisms with a partial reproduction of the physical features. Important efforts have been done to identify the contribution of different processes [49]. Interestingly different mechanisms produce different spatial distributions which allows the identification of the predominant mechanism from numerical simulations [50]. In fact, an important feature that allows to discriminate between different mechanisms is the sign of the correlation between vegetation pattern and other ecosystem variables, such as nutrient concentration. Some mechanisms may lead to a configuration where the two patterns are in phase while others may lead to out of phase patterns, which allow to discard hypothesis. Peatlands have a relevant impact in climate change mitigation. Considered as an important carbon sink its spatial distribution is very relevant to determine the environmental effects of these habitats with presence in different continents [51, 52].

1.2   Marine ecosystems

Pattern formation in marine ecosystems has attracted less attention than its analog phenomenon in terrestrial ecosystems. Different examples have been reported in the literature, although the mechanisms involved and the development of mathematical models describing its origin have not been extensively studied. Patches in bare seascape called *"leopard skin"* [53] and stripes of vegetation [54, 55] have been identified in different seas frequently associated to hydrodynamism. Expanding rings

Figure 1.2: Examples of Fairy circles in *Posidonia oceanica*. Top-Left: Aerial view of a Fairy circle embedded in a homogeneous meadow close to the coast in the Adriatic sea (44°05'37.2"N 14°55'37.0"E). Image reproduced with permission from http://www.dugiotok.hr. Top-Right: Photography of a Fairy circle in Cabrera national park in the Balearic sea (39°08'49.3"N 2°56'07.6"E). Different fairy circles along the coast in the Adriatic sea from Google maps (44°07'18.4"N 14°53'38.0"E).

of vegetation of *Zostera marina* in the Danish Kattegat, instead where found to be correlated with hydrogen sulfide in the sediment, a pythotoxin inhibiting the growth of a broad variety of seagrasses [56]. Fairy circle-like structures also have been found in the Mediterranean coast [57, 58]. In the Adriatic sea similar structures have also been found. This particular case had an important impact on the news because of its supposed mysterious origin. In the national park of Cabrera island, as it can be seen in the Fig. 1.2, a fairy circle-like structure remains barely unchanged from the fifties when first aerial pictures were taken.

It is clear that the technical difficulty of the scientific study of seagrasses coverage is not comparable to terrestrial ecosystems. Neither aerial nor satellite images are completely effective in the characterization of spatial coverage, mainly because reflections on the surface or the depth of seagrasses avoids its identification. Nevertheless, new advances in cartographic technologies for underwater environments have allowed mapping of seagrass coverages. In particular side-scan sonar technology allows to create cartographic data from seagrass coverage with high resolution and covering large regions of the seabottom. LIFE Posidonia project in 2001 was a good example of that, where cartographic data from the Balearic Islands was created and is available

online [1]. In a revision of this data we explain the spatial distribution of vegetation as a result of a pattern formation phenomenon [59]. Thus, to the best of our knowledge patterns in the Balearic Islands are the most important example of vegetation patterns by extension found in marine ecosystems. Primarily produced in the meadows of *Posidonia oceanica* but affecting other species like *Cymodocea nodosa*, the patterns extend over regions of kilometers at the seabottom, where Pollença Bay and Alcudia Bay are the locations with patterns covering the largest extension. Circular holes of vegetation are predominant but elongated shapes like stripes and also patches are easily found.
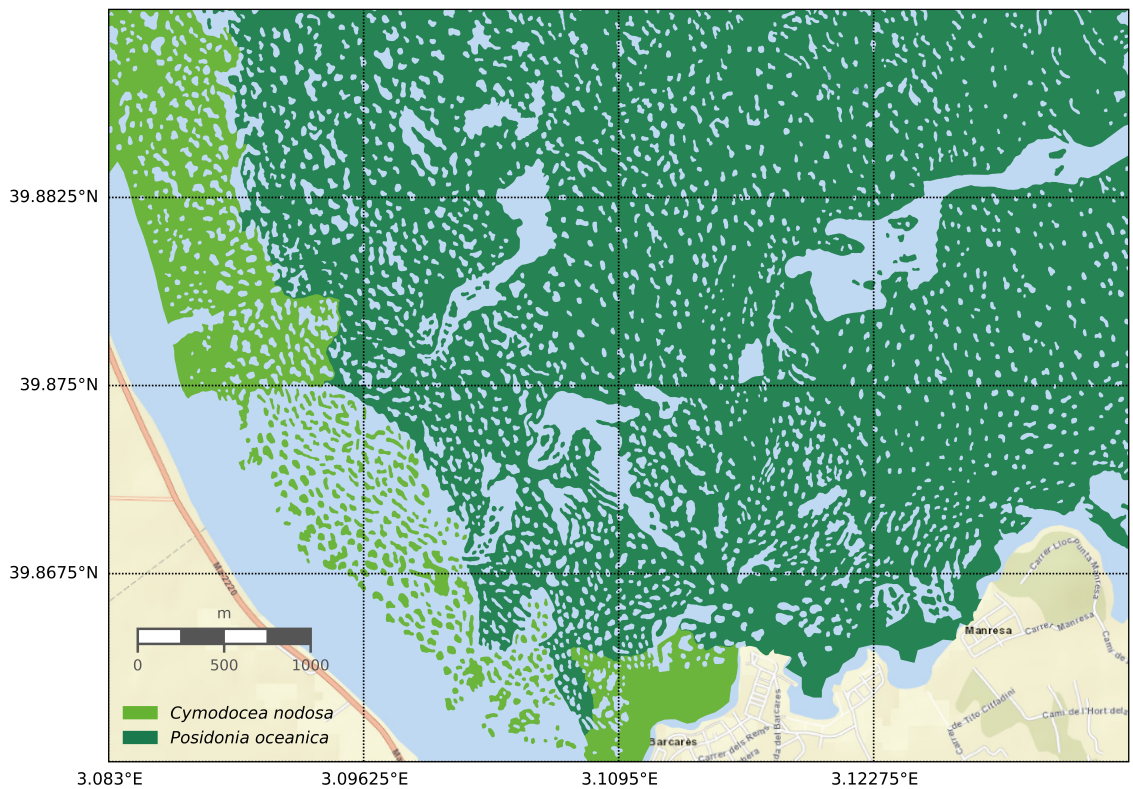
Figure 1.3: Side-scan image of a seagrass meadow in Pollença bay (Mallorca Island, Western Mediterranean) from LIFE Posidonia showing different patterns in meadows of *P. oceanica* and *C. nodosa*.

Further study is needed in the context of pattern formation in marine ecosystems, however, it is clear that interactions determining spatial distribution are also crucial for seagrasses. Thus, the spatial mechanisms need to be properly described to understand the implications they will have in the growth and stability of seagrasses

---

[1]http://lifeposidonia.caib.es

and therefore its implications globally. Seagrasses, with a global presence, provide valuable ecosystem services [60] both globally and locally for nearby communities. They support a great biodiversity [61], thousands of fish and invertebrate species have their habitat in seagrass ecosystems, nevertheless, not only those species are benefited since many others, such as birds or animals living at the coastline also take profit of the presence of seagrasses. Ecosystem services also contribute to produce important economic benefits for local communities, supporting commercial fisheries which produce as much as $3500 $ha^{-1}yr^{-1}$ or an estimated $1.9 trillion in the form of nutrient cycling annually [62]. Moreover, the role of seagrasses in the stabilization of sediment [63] and reduced particle resuspension [64], the biogenic contribution of sediment to the beaches in the form of bivalves and other dead organisms [65], and shoreline protection by wave mitigation [66] create paradisical environments with clear water, which are the basis of the economic activity of many local communities based on tourism.

Seagrasses are considered an important carbon sink [67]. Nutrient ratio of carbon in the tissue is elevated [68, 69]. In addition, an important part of seagrasses remains buried in the sediment or below new layers of seagrass. This important amounts of carbon is not accessible to heterotrophic organisms being preserved for centuries to millennia. Estimates of carbon pools associated with seagrass lie between $4.2 - 8.4$ Pg globally [70]. These numbers are comparable to the amounts captured by terrestrial ecosystems such as forests, whose reforestation and conservation is considered as a useful strategy for climate change mitigation. It has been suggested that the elevated cost of restoration projects is fully recovered by the total CO_2 captured in countries which apply carbon taxes [71]. Thus, seagrass conservation have been claimed as a viable strategy to mitigate the effects of climate change [72], mainly due to the capability of carbon sequestration and to prevent the carbon release of the important actual loss of seagrass coverage around the globe. However, carbon sequestration is not the only reason. The expected increase of sea level, associated to an increment of frequency and strength of storm surges and as a result of flooding and erosive processes, can be importantly damped by the presence of seagrasses, which have been shown to mitigate wave action [73, 74].

Unfortunately, seagrasses are one of the most threatened ecosystems globally. Anthropogenic factors such as direct physical damages and reduced water quality [75, 76] have important effects on seagrass growth. As a matter of fact, since 1980 seagrasses disappear at a rate of 110 km^2yr^{-1}. The rate of loss has increased from around 0.9 $\%yr^{-1}$ before 1940 to 7 $\%yr^{-1}$ since 1990 [62]. *Posidonia oceanica* has also been affected, leading to a loss of 6.9% per year over the past 50 years [77–79]. With its particular slow growth these losses are essentially irreversible. Considering the implications of the negative effects of these losses at different scales it is not surprising that big efforts have been dedicated to restoration projects [80–82]. The reintroduction

Figure 1.4: Schematic representation of a clonal-growth plant.

has been shown to be an effective way to recover ecosystem functions. Nevertheless, restoration is a hard task. The previous removal of threads, water quality and the recovery of neighboring meadows can enhance success [83]. In addition, it has been shown that there is a critical mass for recovery. This minimum threshold in the number of replanted individuals points to facilitative feedbacks acting as self-protection mechanism. This threshold is usually associated to a bistability regime between the populated and the unpopulated state. Although, less investigated the spatial distribution also can be a relevant factor in the recovery rate.

Posidonia oceanica is a clonal-growth plant endemic of the Mediterranean. It is characterized by a very slow horizontal growth of a few centimeters per year. Over long time scales it forms large underwater meadows which support important biodiversity. It is often considered as a bioindicator of healthy ecosystems due to its sensitivity to environmental factors. Salinity, turbidity, pH have been found to affect the development of the meadows [84, 76, 85]. Temperature plays also an important role, increasing mortality and accelerating organic matter decomposition [86] with increasing temperature [87], which can lead to considerable losses under global warming [88]. Irradiance is another important factor influencing the growth, mainly determining the depth limit of establishment of the meadow [89]. However, it can also be relevant in the presence of poor water quality conditions. Otherwise, the limit close to coast for the establishment of the meadow is given by high wave exposure, leading to an increase in mortality close to the coast [74].

Although the studies are carried out in different places of the Mediterranean, they usually have the limitation that census measurements of shoot density are taken in small squares, typically $20 - 40\ cm$ in size. Thus, data of density of shoots generally misses landscape scale features. On the contrary, studies based on meadow cover-
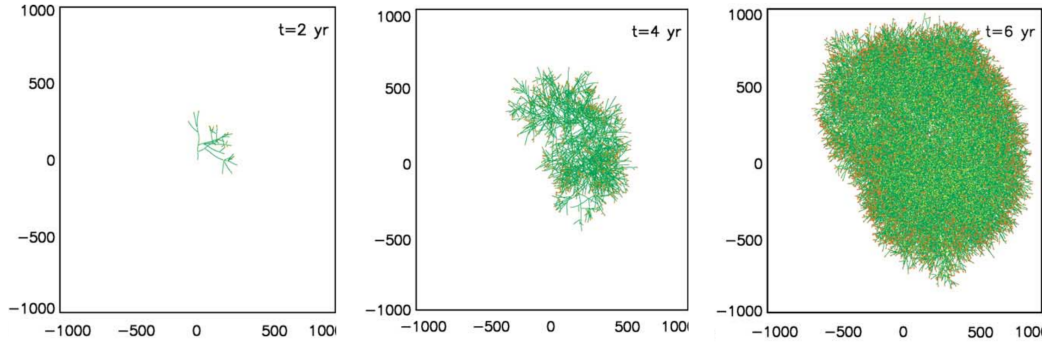
Figure 1.5: Example of a numerical simulation of the evolution of meadow clonal growth plants in space (in meters) from [90] with permission of the author.

age are not usually related to particular effects determining the spatial distribution. From this perspective there is a gap of knowledge between these two approaches. Hence, it is very important to consider the previous knowledge about spatial colonization of clonal growth plants in any spatially extended approach describing the meadow at long spatial scales. Thus, it becomes necessary to introduce previous works of clonal growth.

As a matter of fact, there have been strong efforts to characterize the essential mechanisms of growth of this clonal plant, as well as many other clonal species. In this context the modelization of the growth can provide important guidelines to orient future research.

Clonal plants develop by means of asexual reproduction, where the elongation of the rhizome generates new shoots. The apex, which is the last part of the rhizome, and it is leading the growth, eventually branches generating a new rhizome growing in a different direction. Thus, clonal plants colonize space without the need of seeds. *Posidonia oceanica* in particular has the ability to produce seed, however, the growth is dominated by clonal reproduction. Fig. 1.4 shows a schematic representation of clonal-growth plant.

An important number of studies have been devoted to characterize the rates of each step of clonal spreading. Moreover, different models have been considered in the literature in order to reproduce clonal-growth colonization of space [91–93]. In fact, different approaches have been used, such as models based on lattices, or random walks, sometimes with many parameters which difficult the relation with experimental measurements. In particular the three main mechanisms determining the growth have been identified in [90, 94]. The model, based on limited diffusive aggregation, uses a few features of the plant to characterize the growth. Branching rate and branching angle, spacer length between shoots, rhizome elongation rate, mortality

9

rate and radius of exclusion area are enough to show nonlinear features of the growth such as maximum density of plants or the evolution of patch radius with time. Fig. 1.5 shows an example of a numerical simulation of the model in [90]. In general, these discrete agent based models account for each individual shoot, as a result they are not suitable for large spatial descriptions.

From this point of view questions about the ecological implications on a large spatial and time scales of local effects on the plant require a more interdisciplinary approach that integrates the intrinsic mechanisms of growth in more extended description. This thesis aims to contribute to this challenge.

Pattern formation in *Posidonia oceanica* meadows

Spatial organization of vegetation is driven by mechanisms operating at large distances compared to the development spatial scale of the plant. Pattern formation is the manifestation of this fact. *P.oceanica* meadows are a remarkable example of vegetation patterns which extend over regions of kilometers where the responsible mechanism remains to be clarified. The large scale of these patterns makes it clear that an appropriate description of the growth of the meadow can not account for shoots individually but for the density of shoots for extended regions instead. However, the growth of the individuals will determine the growth of the meadow. Hence, a better approach to the modelization of clonal-growth plants like *P.oceanica* is a coarse grained description. In this chapter we aim to develop a model describing the evolution of clonal plants based on the main mechanisms of growth. Previous models based on individual shoots development [90, 94], have shown that three mechanisms drive the growth of the plant. First, the apex of the plant grows in the horizontal plane elongating the rhizome at velocity ν. As it grows new shoots appear separated by a typical distance ρ between them. The shoots remain rooted at the same position while the apex continues to grow colonizing new space. Second, the apex can develop new branches at a certain rate ω_b, where the new rhizomes grow in a direction forming an angle ϕ_b with the original one. Finally, all shoots have a typical lifetime, which translates into a mortality rate ω_d. In general, the value of the parameters can depend on the density of plants or on the position since environmental factors can have an important influence in plant development. Different clonal plants are characterized by different values of the parameters with some variability due to genetic and environmental conditions [90]. *P.oceanica* in particular has a very slow growth of a few centimeters per year, nevertheless, with clones living extended time periods [95] large meadows are formed in long time scales, over centuries to millennia [96, 92].

The chapter is organized as follows: In the first section we derive a model based on clonal-growth mechanisms. Section two is devoted to the analysis of the model. The third section parametrizes the model to describe the growth of *Posidonia oceanica*. In the fourth section we apply the model to more realistic conditions to reproduce features of vegetation patterns close to the coast. Finally, the last section analyzes the angular dependence of the model on the growth direction of apices.

2.1 Advection-Branching-Death model: A model for clonal growth

Based on the three previous mechanisms driving the growth of the plant we develop a partial differential equation (more precisely an integro-differential equation) describing the evolution of the density of apices and shoots. Thus, the density of apices at position $\vec{r} = (x, y)$ with a growth direction given by the angle ϕ at time t is described by $n_a(\vec{r}, \phi, t)$ and the density of shoots at position $\vec{r}$ and time t by $n_s(\vec{r}, t)$. By convenience, in the derivation, apices are considered to carry a shoot, so the total density of shoots is given by the sum of apices in all directions and shoots $n_t(\vec{r}, t) = n_s(\vec{r}, t) + \int_0^{2\pi} n_a(\vec{r}, \phi, t)d\phi$. Additionally, one should realize that while other parameters are scalar quantities, the velocity of growth has a direction and it can be written as a vector $\vec{v}(\phi) = (\nu \cos\phi, \nu \sin\phi)$. Thus, considering the contributions of the three main mechanisms of growth to the number of shoots in infinitesimal portion of space with area $dxdy$, one can write two equations describing the evolution of shoots and apices respectively. First, the number of apices growing in direction ϕ at $t + dt$ in an infinitesimal surface of area $dxdy$ located at $\vec{r}$ will be the sum of two contributions: (i) the apices that remain alive coming from $\vec{r} - \vec{v}(\phi)dt$ due to rhizome elongation and (ii) new apices developed because of branching from directions of growth $\phi + \phi_b$ and $\phi - \phi_b$, which are the only directions contributing to the growth in direction ϕ. Note that those apices that go away due to rhizome elongation are contributing to position $\vec{r} + \vec{v}(\phi)dt$. Then, we obtain

$$
\begin{aligned}
n_a(\vec{r}, \phi, t + dt)dxdy &= (1 - \omega_d dt)n_a(\vec{r} - \vec{v}dt, \phi, t)dxdy \\
&+ \frac{\omega_b dt}{2}\left(n_a(\vec{r}, \phi + \phi_b, t) + n_a(\vec{r}, \phi - \phi_b, t)\right)dxdy. \quad (2.1)
\end{aligned}
$$

Making a Taylor expansion of Eq. (2.1) and neglecting second-order terms and higher, we obtain

$$
\begin{aligned}
n_a(\vec{r}, \phi, t) + \partial_t n_a(\vec{r}, \phi, t)dt &= (1 - \omega_d dt)n_a(\vec{r}, \phi, t) - \vec{v}dt \cdot \vec{\nabla} n_a(\vec{r}, \phi, t) \\
&+ \frac{\omega_b dt}{2} \left(n_a(\vec{r}, \phi + \phi_b, t) + n_a(\vec{r}, \phi - \phi_b, t) \right), \quad (2.2)
\end{aligned}
$$

where it is possible to simplify (2.2) to obtain an equation that describes the evolution of $n_a(\vec{r}, \phi, t)$.

$$
\begin{aligned}
\partial_t n_a(\vec{r}, \phi, t) &= -\omega_d n_a(\vec{r}, \phi, t) - \vec{v}(\phi) \cdot \vec{\nabla} n_a(\vec{r}, \phi, t) \\
&+ \frac{\omega_b}{2} \left(n_a(\vec{r}, \phi + \phi_b, t) + n_a(\vec{r}, \phi - \phi_b, t) \right), \quad (2.3)
\end{aligned}
$$

where $\vec{\nabla} = (\partial_x, \partial_y)$.

Similarly one can apply the same procedure to obtain the evolution of $n_s(\vec{r}, t)$. Two contributions to the number of shoots are considered: (i) shoots remaining alive at the same position and (ii) surviving apices that go away in any direction leaving a shoot behind.

$$
\begin{aligned}
n_s(\vec{r}, t + dt)dxdy &= (1 - \omega_d dt)n_s(\vec{r}, t)dxdy \\
&+ \frac{\nu}{\rho}dt(1 - \omega_d dt) \int_0^{2\pi} n_a(\vec{r}, \phi, t)dxdyd\phi, \quad (2.4)
\end{aligned}
$$

Again doing a Taylor expansion and keeping first order terms, one obtains

$$
n_s(\vec{r}, t) + \partial_t n_s(\vec{r}, t)dt = (1 - \omega_d dt)n_s(\vec{r}, t) + \frac{\nu}{\rho}dt \int_0^{2\pi} n_a(\vec{r}, \phi, t)d\phi, \quad (2.5)
$$

where its possile to obtain the equation for the temporal evolution of $n_s(\vec{r}, t)$

$$
\partial_t n_s(\vec{r}, t) = -\omega_d n_s(\vec{r}, t) + \frac{\nu}{\rho} \int_0^{2\pi} n_a(\vec{r}, \phi, t)d\phi. \quad (2.6)
$$

Eqs. 2.3 and 2.6, describe the evolution of a meadow, accounting for shoots and apices. We name this model Advection-Branching-Death (ABD) model according to terms derived from the main mechanisms of clonal growth. The first two terms in Eqs. (2.3) and (2.6) are death terms representing the mortality of shoots and apices, which are both considered to occur with the same rate ω_d. The second terms in Eqs. (2.3) and (2.6) are the result of the elongation of the rhizome. In Eq. (2.3) an advection term describes the movement of apices in the respective directions given by $\vec{v}(\phi)$, while in Eq. (2.5) an integral term accounts for all shoots left behind from all

directions of growth. Finally the last term in Eq. (2.3) accounts for the contribution of apices growing in adjacent directions separated by the branching angle ϕ_b that contribute to the direction ϕ. The parameters of the model are susceptible to change due to different reasons. Genotypic differences within the meadow are an intrinsic source of variability of the parameters, nevertheless mean values of the parameters characterizing the growth such as ν, ρ or ϕ_b are representative of each species. External environmental conditions or the presence of plants in the neighborhood are other important sources of variability where not all parameters are affected equivalently. Mortality is indeed considerably affected by all these factors. Thus, for the sake of simplicity, we consider that the mortality rate encompasses all these dependencies. More specifically, three terms contribute to the total mortality

$$\omega_d[n_t(\vec{r}, t)] = \omega_{d0} + b n_t^2(\vec{r}, t) + \int\int \mathcal{K}(\vec{r} - \vec{r}')(1 - e^{-a n_t(\vec{r}', t)})d\vec{r}' \qquad (2.7)$$

On the one hand, the intrinsic mortality rate, $\omega_{d0} > 0$, of an individual shoot at a particular position in the landscape is the contribution to the mortality $\omega_d(n_t)$ which depends only on environmental factors. On the other hand, the mortality $\omega_d(n_t)$ depends on two density-dependent terms: local saturation and nonlocal interaction. The nonlinear term $b n_t^2$ corresponds to local saturation representing high mortality conditions when shoots are very close and the density increases excessively. Thus, the environmental carrying capacity is controlled by the parameter b which determines the maximum density of shoots. On second place, the integral term accounts for nonlocal interactions where shoots at a given position $\vec{r}$ interact with its neighbors carrying the kernel $\mathcal{K}(\vec{r} - \vec{r}')$ the strength and length of the interaction. Nonlocality allow that regions with high density of shoots can affect the growth of its neighbors. Thus, nonlinearity and spatial interaction, known components leading self-organization are included in the model.

The terms contributing to death rate are consistent with previous knowledge of seagrass development. External factors such as temperature, salinity and irradiance regimes have important effects on the intrinsic mortality ω_{d0} [97]. The local saturation of the density is the result of self-shading which explains the decline of biomass with depth as less light is available [98, 89]. Moreover, depletion of other resources can influence mortality leading to an additional limited net growth. Nonlocal interaction encompass different facilitative and competitive process which have been shown to contribute to spatial organization, however, its specific influence with distance have been poorly quantified. Dissipation of wave energy by neighboring plants is an important facilitative mechanism, which reduces stress and prevents shoot removal contributing to trap and stabilize sediments [99, 100]. Other multiple facilitative effects have been argued to contribute to spatial organization [101, 102]. Competitive mechanisms, are for example the result of the spreading of organic matter decompo-

sition by sulfate-reducing bacteria, increasing sulfide concentration in the sediment leading to the appearance of fairy rings [56]. Additionally, the depletion of nutrients by plants up-current [103] can also contribute to negative interactions. The evidences suggest both competitive and facilitative nonlocal effects are important in the development of the meadow, driving the process of self-organization. Hence, we consider a kernel $\mathcal{K}$ with two terms of Gaussian shape

$$\mathcal{K}(\vec{r}) = \kappa \mathcal{G}(\sigma_\kappa, \vec{r}) - \mu \mathcal{G}(\sigma_\mu, \vec{r}) \tag{2.8}$$

where $\kappa > 0$ is the strength of the competitive interaction with width σ_κ, and $\mu > 0$ is the strength of facilitation with width σ_μ, where the widths of the Gaussians correspond to the spatial extension of each interaction. Both interaction terms in Eq. (2.8) are considered to have a Gaussian shape $\mathcal{G}(\sigma, \vec{r}) = e^{-r^2/(2\sigma^2)}/(\sigma^2 2\pi)$, where $r^2 = x^2 + y^2$. Other kernels have been considered in the literature in different contexts [104], although qualitatively, the pattern formation feature does not depend strongly on the precise shape of the kernel [105, 106], provided it decays faster or equal than exponential [107]. The term $(1 - e^{-an_t})$ can be expanded for low densities as $(1 - e^{-an_t}) \simeq an_t$, leading to the usual nonlocal term in Lotka-Volterra-like models [108]. The exponential has been introduced to saturate the interaction strength for high densities, such that the mortality rate ω_d cannot become negative because of the facilitative interaction leading to the local creation of plants, which is unreal because a new shoot can be created only through the growth of the rhizomes or a branching event. Note that we should have $\mu \leq \omega_{d0}$ to guarantee positive mortality. For simplicity, in the following, we take $\mu = \omega_{d0}$. For low densities, then, parameter a multiplies the strength of the nonlocal interaction. However, the larger the parameter a, the faster the saturation of the interaction as the density grows. Varying a and κ, one can change the relative strength between competition and facilitation. As a result of the two Gaussians with different widths and signs, the kernel has the shape of an inverted Mexican hat, and the interaction is stronger at short distances, decaying very fast with $|\vec{r}|$. The balance between facilitation and competition de-
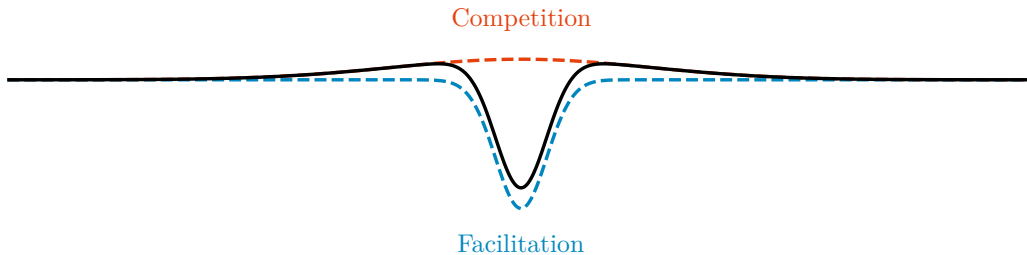
Figure 2.1: Schematic representation of the spatial dependence of the kernel composed by the sum of two Gaussian functions representing facilitation and competition.

termines the coexistence between the populated and the unpopulated states, being

globally facilitative when there is coexistence. As a result of the difference of the two Gaussians with different strengths κ and ω_{d0} and extensions σ_κ and σ_μ, the kernel can take positive and negative values at different distances depending on the parameters. However, long-range competitive interactions are responsible for the formation of patterns [109] sometimes simultaneously with facilitative interactions [6]. It is important to clarify that competition and facilitation are treated in this description independently of each other, while sometimes facilitative and competitive interactions can be the result of a single process, leading to a simultaneous change in the intensity of both. This assumption is justified by the lack of knowledge about spatial interactions for seagrasses.

Thus, observation of spatial patterns suggests the existence of nonlocal competitive interactions. Selecting $\sigma_\kappa > \sigma_\mu$ results in a kernel that is weakly competitive at large distances, yielding to a suitable nonlocal interaction for pattern formation similarly to [6].

2.2 Analysis of the ABD model

Leaving aside the nonlocal part of the model for the moment, the two equations describing clonal growth are interesting by itself and we devote some time to their analysis. First of all, while the equation for the density of shoots has nothing particular, the equation of the density of apices accounts instead for the direction of growth, in such a way we can track the density of apices growing in each direction. These two equations resemble a set of coupled two dimensional fields but since ϕ is a continuous variable, taking values between 0 and 2π, the field for the density of apices is actually three dimensional. The coupling between the densities of apices growing in each direction is given by the branching process and by the mortality through the total density n_t. The branching is a nonlocal term in the angle ϕ, where adjacent directions separated by the branching angle ϕ_b couple one to each other. The mortality affects all directions equivalently. The other particularity of the model is the advection term. This term produces a displacement given by $\vec{v}(\phi)$ of the density of apices growing in the direction ϕ which is different for each direction. This can be confusing to the reader because this does not imply a drift of the meadow in any direction. In fact this mechanism allows the expansion of the meadow colonizing new space. Branching is also important in this process, mainly because one can begin only with apices growing in a particular direction and quickly branching will populate other directions leading to a radial growth of the meadow. Both terms together are responsible for the spreading of vegetation in a way different to the traditional diffusion usually considered in vegetation models. From the mathematical point of view the term $\vec{v}(\phi) \cdot \vec{\nabla} n_a(\vec{r}, \phi, t)$ is non-variational term. Moreover, it is not possible

to integrate the angle and write a single equation for the total density. Regarding numerical integration one usually considers the minimum set of directions compatible with the branching, in the case of *P. oceanica* where $\phi_b = 49.0° \approx 45°$, eight directions are enough to reproduce the dynamics. The advection term does not dampen high wavenumber modes so it can be problematic for computational integration, however, nonlocal interactions resolve this problem damping high wavenumbers. With the simulation shown in Fig. 2.2 one can gain intuition about the explained growth where the density of apices growing in different directions is represented. As the reader will appreciate apices tend to have maximum density in the direction outwards the meadow, showing a directional growth which produces a radial spreading.
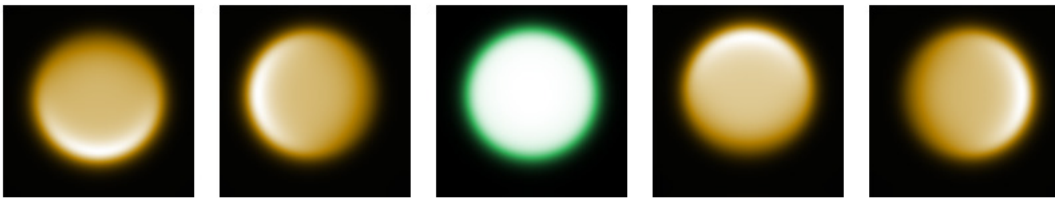
Figure 2.2: Representation of the growth of a meadow in arbitrary units. In the center the shoots density in greenscale where maximum density is represented in white and zero density in black. And the apex density in each direction in the other panels, from left to right $\phi = 270°, 180°, 90°, 0°$ according to yellowscale where black represent zero density and white the maximum density.

Section 2.5 is devoted entirely to studying the dependence of the results on the angle discretization. However, it is necessary to have an intuition of the behavior of these terms before trying to understand the complex dynamics resulting from nonlocal interactions.

The unpopulated solution $n_t^* = n_s^* = n_a^* = 0$ is obviously a stationary solution of the model existing for all parameter regimes. When branching ω_b exceeds intrinsic mortality ω_{d0} the unpopulated solution becomes unstable and the density grows with time to form a homogeneous meadow. The homogeneous stationary solution given by n_t^*, n_s^* and n_a^*, where the total density of apices is $N_a^* = 2\pi n_a^*$, satisfy the stationary condition of branching rate equal to total mortality $\omega_b = \omega_d(n_t^*)$, implying there is a balance between the two processes. This condition leads to an implicit equation for n_t^* and parameters, however, instead of having a closed form for n_t^* one can write

$$\omega_{d0} = \frac{\omega_b - \kappa(1 - e^{-an_t^*}) - bn_t^{*2}}{e^{-an_t^*}}, \tag{2.9}$$

where it is possible to draw the curve $n_t(\omega_{d0})$ numerically. The values of n_s^* and N_a^*

are just fractions of the total density n_t^* determined by the parameters ω_b, ρ, ν.

$$N_a^* = \frac{\rho\omega_b}{\nu + \rho\omega_b}n_t^*, \quad n_s^* = \frac{\nu}{\nu + \rho\omega_b}n_t^*, \quad N_a^* = \frac{\rho\omega_b}{\nu}n_s^*. \tag{2.10}$$

The ratio between apices and shoots is essentially determined by the ratio of the birth rates of each one, where the birth rate of apices is ω_b and the birth rate of shoots is ν/ρ. Thus, the ratio is ussually small for different species leading to a small number of apices as compared to the total, which is in agreement with experimental measurements.

The transition to the populated state becomes subcritical when $\kappa < \omega_b$ and the populated solution coexist with the unpopulated solution for a range of values of $\omega_{d0} > \omega_b$ until a saddle node bifurcation at ω_{d0,SN_1}. In the bistability regime and leaving apart nonlocal interactions an homogeneous initial condition with density above a threshold will grow, while those with less density will die. The threshold determining the survival of the homogeneous meadow is determined by the unstable branch of the solution given by Eq. (2.9). Facilitation is the responsible mechanism for this effect, only those values of the density in which facilitative effects overcome mortality can thrive while those with low density are highly exposed and end up in the unpopulated solution. One can find, easily the saddle node bifurcation looking for the relative maximum of $\omega_{d0}(n_t)$,

$$\frac{\partial \omega_d}{\partial n_{t^*}} = 0 \Rightarrow n_{t,SN_{1,2}}^* = -\frac{1}{a} \pm \sqrt{\frac{1}{a^2} + \frac{\omega_b - \kappa}{b}}. \tag{2.11}$$

One obtains two Saddle-node bifurcations, one has negative density while the other is positive as long as $\kappa < \omega_b$, we are only interested in the second since negative solutions are not physical. Thus, for a given value of competition strength κ and increasing mortality the homogeneous density persist for values of mortality beyond ω_b until $\omega_{d0,SN}$, where there is a sudden loss of vegetation. After this transition it is necessary to decrease mortality below ω_b to recover vegetation. In the opposite case, when $\kappa > \omega_b$, the transition to the populated case is supercritical and the density increases gradually when decreasing mortality below ω_b.

Nonlocal interactions have important effects on the dynamics of the system. A linear stability of the homogeneous solution reveals there is a finite wavelength instability, known as Turing or modulation instability (MI). In the extreme cases, where $\omega_{d0} >> \omega_b$ or $\omega_{d0} << \omega_b$, bare soil or the populated state prevail. On the contrary, when both parameters are similar nonlocal competition plays an important role. Thus, perturbations with higher density compete stronger than vegetation in the neighborhood leading to a decrease in the density. Consequently the perturbation can grow at the expense of the surrounding meadow, generating a feedback process where modulations of the density are amplified and due to nonlinearity, end up forming a regular pattern. The linear stability shows that there is a modulation of the

homogeneous stationary solution at a finite wave number q_c, which has maximum growth $Re[\lambda(q_c)]$ and becomes positive at the MI for the critical value of mortality $\omega_{d0,c}$ as shown in Fig. 2.3. The linear stability analysis does not ensure the formation of a pattern as it only gives information about the growth of small-amplitude perturbations around the homogeneous solutions but gives important information about the evolution of the system.
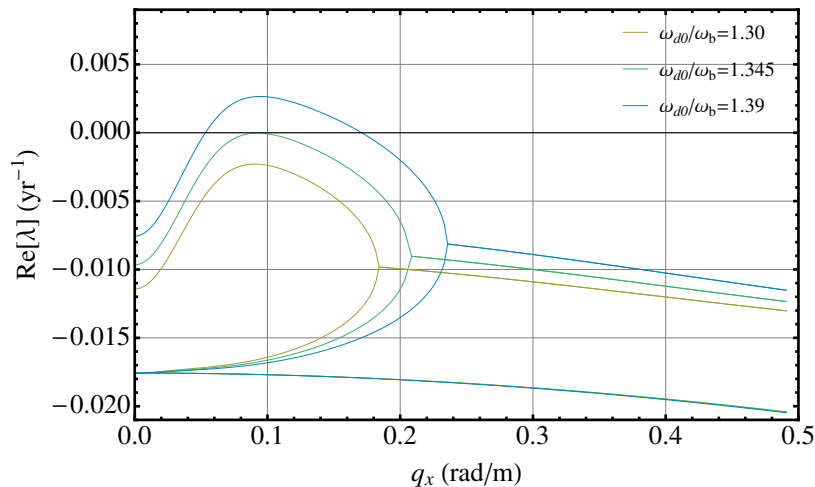
Figure 2.3: Growth rate of perturbations with wavenumber $(q_x, q_y = 0)$ close to the MI. Three different values of mortality are shown, the yellow curve corresponds to a stable case, the green one to the critical point, and finally the blue line corresponds to the unstable case. Here $\omega_b = 0.06 \ year^{-1}$, $\nu = 6.11 \ cm/year$, $\rho = 2.87 \ cm$, $\phi_b = 45°$, $b = 1.25 \ cm^4 year^{-1}$, $\kappa = 0.048 \ year^{-1}$, $\sigma_\kappa = 2851.4 \ cm$, $a = 27.38 \ cm^2$, and $\sigma_\mu = 203.7 \ cm$.

The critical value of $\omega_{d0,c}$ determining the onset of the instability has a complicated dependence with parameters. For decreasing values of κ below ω_b, the critical value approaches to the saddle node bifurcation SN_1, creating a window of instability of the populated solution to patterns from $\omega_{d0,c}$ to ω_{d0,SN_1}. Differently, for higher competition strengths $\kappa > \omega_b$, where the populated is supercritical, the instability region broadens, extending to lower values of mortality. Additionally a second modulation instability appears for larger values of mortality. Thus, increasing mortality the homogeneous meadow becomes unstable to patterns and for further mortality it stabilizes again, producing a region of instability between two Turing bifurcations. Fig. 2.4 shows the region of instability to patterns of the homogeneous populated solution.

After the onset of instability, regular patterns form, different pattern are possible for different values of mortality. Nevertheless, these patterns are not accessible with linear calculation due to nonlinearities in the equations. Numerical simulations instead allow to study the dynamics in the nonlinear regimes. A pseudo-spectral
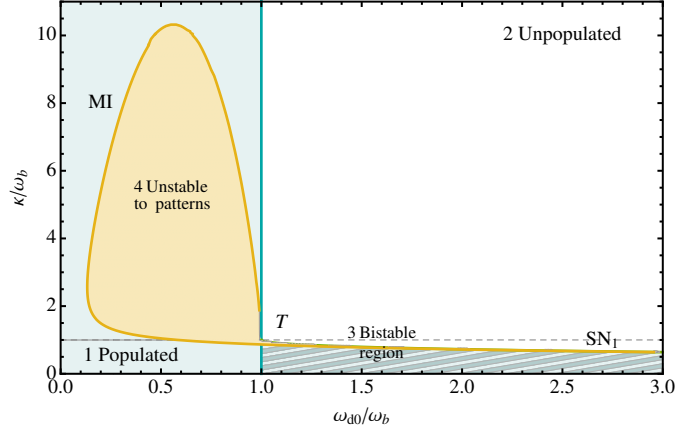
Figure 2.4: Phase diagram of the ABD model for *P. oceanica*. Here $\omega_b = 0.06 \ year^{-1}$, $\nu = 6.11 \ cm/year$, $\rho = 2.87 \ cm$, $\phi_b = 45°$, $b = 1.25 \ cm^4 year^{-1}$, $\sigma_\kappa = 2851.4 \ cm$, $a = 27.38$ cm^2, $\sigma_\mu = 203.7 \ cm$. We represent the region where the populated solution is stable in blue (region 1), where the unpopulated solution is stable in white (region 2), the region where populated and unpopulated coexist is shaded (region 3), and finally the region where the populated solutions is unstable to patterns in yellow (region 4). Note that the patterns arising from the MI extend beyond this region and may coexist with the populated or unpopulated solutions. T stands for the transcritical bifurcation at $\omega_{d0}/\omega_b = 1$, and SN_1 for the saddle-node bifurcation where the subcritical populated solutions ends.

method is used to integrate the time evolution of the Eqs. (2.3) and (2.6). Notice, the model is effectively three dimensional, two spatial dimensions (x, y), and one angular dimension (ϕ) corresponding to the direction of growth of the apices. In the pursuit of computational efficiency we use the minimum number of grid points in ϕ space compatible with the branching angle, mainly because we are interested in the spatial distribution of the population densities. Thus, we consider angles multiple of $\pi/4 = 45°$, which approximates well the branching angle both for *P. oceanica* as for *C. nodosa* [90, 94], which we will use later. This means that we deal with then nine two-dimensional fields: one for the density of shoots and 8 for the density of apices growing in each corresponding direction. The nine fields, that depend on (x, y), are coupled through the branching and the total density in the nonlocal term. The pseudospectral method described in Appendix C is used to integrate the evolution of each one of the nine two dimensional fields. Typical simulations start with the homogeneous solution with a superimposed small random perturbation. In stable regions of parameter space perturbations decay, and the solution remains, while in regions where the homogeneous solution is unstable, perturbations grow, and the nonlinear dynamics send the system to a different stable solution. In order to study the stability of the different spatial patterns changing mortality we have performed simulations continuing ω_{d0}. We start with an initial condition of a pattern, we add

small white noise, and we change the mortality a small amount, letting the system evolve to reach a new stationary state. We use then, the final state as initial condition for the next parameter step. Repeating this procedure we can generate the stable branches shown in the bifurcation diagrams, where the average densities of each final state is plotted (Fig. 2.5).
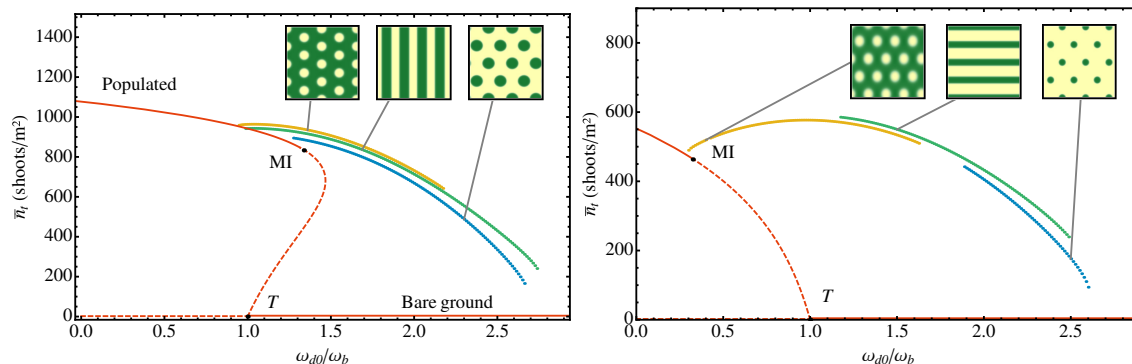

Figure 2.5: Mean shoot density $\bar{n}_t$ (total number of shoots divided by area) as a function of normalized mortality ω_{d0}/ω_b for five different solutions of the ABD model for the subcritical case on the left panel and the supercritical case on the right panel. Homogeneous populated and unpopulated states (red), hexagonal arrangement of fairy circles in yellow, stripes in green, and hexagonal arrangement of spots in blue. Solid (dashed) lines indicate stable (unstable) solutions. The insets show the vegetation patterns in the inhomogeneous cases. Only the stable parts of the pattern branches are shown, as obtained from direct numerical simulations of the model. MI corresponds to the modulational instability of the populated state, and T corresponds to the transcritical bifurcation of the bare soil. Parameter values $\omega_b = 0.06\ year^{-1}$, $\nu = 6.11\ cm/year$, $\rho = 2.87\ cm$, $\phi_b = 45°$, $b = 1.25\ cm^4 year^{-1}$, $\sigma_\kappa = 2851.4\ cm$, $a = 27.38\ cm^2$, $\sigma_\mu = 203.7\ cm$, $\mu = \omega_{d0}$ for both panels. $\kappa = 0.048\ year^{-1}$ for left panel and $\kappa = 0.072\ year^{-1}$ for right panel.

Increasing mortality a particular sequence is observed, first circular holes without vegetation arranged in an hexagonal pattern (negative hexagons), second stripes of vegetation, and third circular spots arranged in an hexagonal pattern (positive hexagons). The sequence between different solution is general for different vegetation models [3, 35] as predicted by the theory of pattern formation. However, the ranges of stability and its coexistence may be different in each model. As can be seen in Fig. 2.5, for different values of κ in the subcritical and the supercritical case, the branches associated to different patterns change its domain of stability. An important aspect is that independently of the parameters, the formation of patterns makes the meadow much more resilient, where patches are the last landscape before desertification, persisting for larger values of mortality. Thus, when desertification is reached, mortality has to be reduced until ω_b to recover the meadow. Alternatively,

21

it is possible to plant a spot of vegetation overcoming a threshold density given by the unstable branch in order to recover vegetation. Moreover, the presence of different patterns for different levels of stress is a very useful diagnostic tool which allows to infer the health conditions of the meadow based on the spatial distribution of vegetation, which is accessible by aerial images, side scan sonar maps, or in a few special cases, from direct view from the coast.

As an additional proof of the formation of patterns and the sequence leading to desertification we provide images of numerical simulations of the discrete model described in [90] introducing the same nonlocal interactions. As we can see in Fig. 2.6 patterns of negative hexagons, elongated shapes resembling stripes, and positive hexagons appear in the same order increasing mortality.
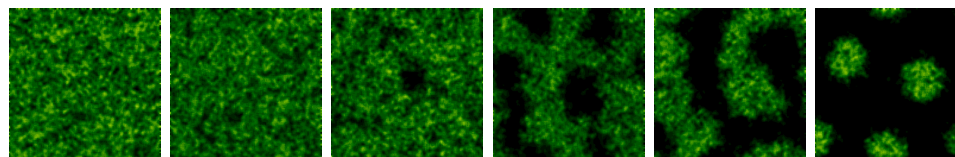
Figure 2.6: Population density for the discrete model showing the standard sequence of patterns for increasing mortality. The density of plants is shown using greenscale where high density is represented in green and zero density in black. We thank T. Sintes for kindly providing these images.

Localized structures are also a result of pattern formation. In particular, isolated spots of vegetation surrounded by bare soil and circular holes without vegetation embedded in an homogeneous meadow are typical examples (Fig. 2.7). The first case appear for large values of mortality usually around the end of the branch of positive hexagons. This spatial distribution is the last step before desertification being the most resilient spatial distribution. This compact forms allow plants to profit from the effects of facilitation and the lack of density in the close proximity. On the second case, appearing for lower mortalities and consist of isolated holes embedded in an homogeneous meadow. These are also stable solutions of the model. They correspond to the circles without vegetation shown in pictures of the Adriatic sea, and the Cabrera Island in the Balearic Sea, which are the marine analog of terrestrial fairy circles. These spatial configuration is frequently characterized by a maximum of density in the perimeter of the circle that profit from the lack of vegetation in the center, moreover, new plants are prevented to grow in the central region because of high competition due to the surrounding density of plants. The formation of isolated holes is generally produced in a particular regime, namely where the solution of negative hexagons is subcritical and coexist with the homogeneous solution. In this region of bistability one can find usually a subrange of mortalities in which isolated holes, are stable [110–113]. These localized structures are an example of dissipative

soliton. The bifurcation structure of such solutions is known as homoclinic snaking [114]. We will devote more efforts in chapter 4 to characterize these structures in detail. It is important to highlight the fact that the degree of bistability of the pattern with the homogeneous solution, understood as the length of the interval of coexistence between the two solutions, promotes the formation of this localized states, and this at the same time is affected by the degree of bistability between the populated and the unpopulated solution.
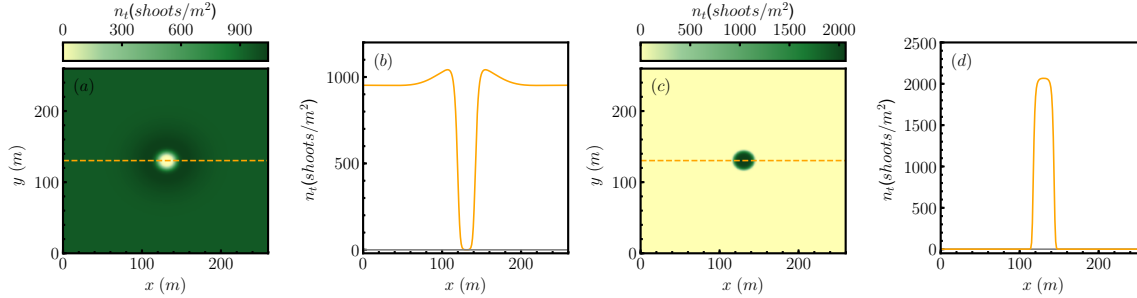
Figure 2.7: Spatial distribution of the shoot density for localized structures (high densities are represented in dark green and low ones in bright yellow). The fairy circle, or dissipative soliton, is clear in the density profile (b) along the transverse cut shown in panel (a) by a dashed line. Here, $\omega_{d0} = 0.057year^{-1}$. The isolated patch is shown in panel (c) where panel (d) shows a transverse cut of the shoot density. Here $\omega_{d0} = 0.162year^{-1}$. Other parameters are the same as in Fig. 2.5 with $\kappa = 0.048\ year^{-1}$.

2.3 Parametrization for *Posidonia oceanica*

We have shown different results that help to understand the dynamical behavior of the model. However, we have not justified the parameters used neither if they represent the growth of *P. oceanica* meadows. Our aim was to provide the necessary understanding of the model necessary to facilitate the explanation of the choice of parameters.

We can distinguish two groups of parameters, first ω_b, ϕ_b, ω_{d0}, ν, ρ which are the parameters associated to clonal-growth rules and are well known in the literature [90, 94]. For *P. oceanica* in particular $\omega_b = 0.06\ year^{-1}$, $\phi_b = 45°$, $\nu = 6.11\ cm/year$, $\rho = 2.87\ cm$, where ω_{d0} is considered here as a control parameter which varies from zero to three fold ω_b. As one may notice the rates are small leading to time scales which extend from decades to millenia, which is the expected lifetime for this plant. The values of the second set of parameters, a, b, κ, σ_κ, σ_μ are unknown but they can be estimated based on observations and data. The parameter b, which fixes the scale of the density of shoots, is determined using typical values of the density of shoots, in

particular we choose the homogeneous density to be around $800 \ shoots/m^2$ [90, 94]. However, the homogeneous density depends additionally on ω_{d0}, κ and a, and we have to fix them first. In order to have isolated holes, we need $\kappa < \omega_b$ to have bistability of the two homogeneous solutions and of patterns and the populated solution. We choose $\kappa = 0.8\omega_b = 0.048 \ year^{-1}$. The parameter a controls the degree of bistability, so choosing $a = 27.38 \ cm^2$ (which in the adimensional units presented in the appendix corresponds to $a = 6$) gives a finite range of bistability which facilitates the presence of isolated holes. Thus, we choose b such that given κ and a for $\omega_{d0}/\omega_b = 1.4$, which is close to the saddle node and the Turing, we have the homogeneous stationary solution around $800 \ shoots/m^2$, which gives $b = 1.2457 \sim 1.25 \ cm^4 year^{-1}$.

The only missing parameters are those related to the spatial extension of the nonlocal interaction, σ_κ and σ_μ. The extension of the facilitation σ_μ does not play an important role in the formation of patterns. In fact, changing the value of this parameter one quickly reaches to the conclusion, based on the results of the linear stability analysis, that the mechanism behind pattern formation is competition. Basically looking at the linear stability analysis one can see that the negative contribution of long-range competition to the eigenvalues damps short wave numbers, while facilitation can not produce a maximum at finite wavelength. Thus, the value of this parameter is quite irrelevant, one may change nonlocal by local facilitation without affecting the results. Even so, we have preserved this term with a small value of $\sigma_\mu = 203.7 \ cm$ (in adimensional units $\sigma_\mu = 2$). Otherwise, σ_κ is a relevant parameter, in fact it determines the wavelength of the pattern. As a matter of fact, it is possible to infer the competition distance based on the wavelength of the pattern. The side-scan cartography of the LIFE Posidonia project in 2001 provides a good data set to measure the typical wavelength. Side-scan cartography shows *P.oceanica* coverage in different places of the Balearic Islands. We have taken samples of the data with ordered patterns, most of them in Pollença and Alcudia bays where the patterns are more abundant and we have performed Fourier transform of these images. The maximum amplitude gives the predominant spatial scale, which is directly related to the wavelength of the pattern. We have removed the homogeneous contribution and we have taken the wave number with maximum amplitude. In Fig. 2.8 we show an example of the Fourier transform of one of the picked samples that clearly shows a typical scale with a clear maximum at $|k| \approx 0.017m^{-1}$, specially visible in the k_y direction. The coordinates location of the left-top corner and right bottom corner of each sample as well as the wave number with maximum amplitude are presented in Table 2.1. We conclude the average wave number is 0.016 ± 0.003 m^{-1} corresponding to typical wavelength of $62.9 \pm 12.7 \ m$.

Next, we use the linear stability analysis to compute the predicted wavelength of the pattern as a function of σ_κ. We use the wavelength with maximum growth rate. Although it is clear that the wavelength of the pattern will be affected by
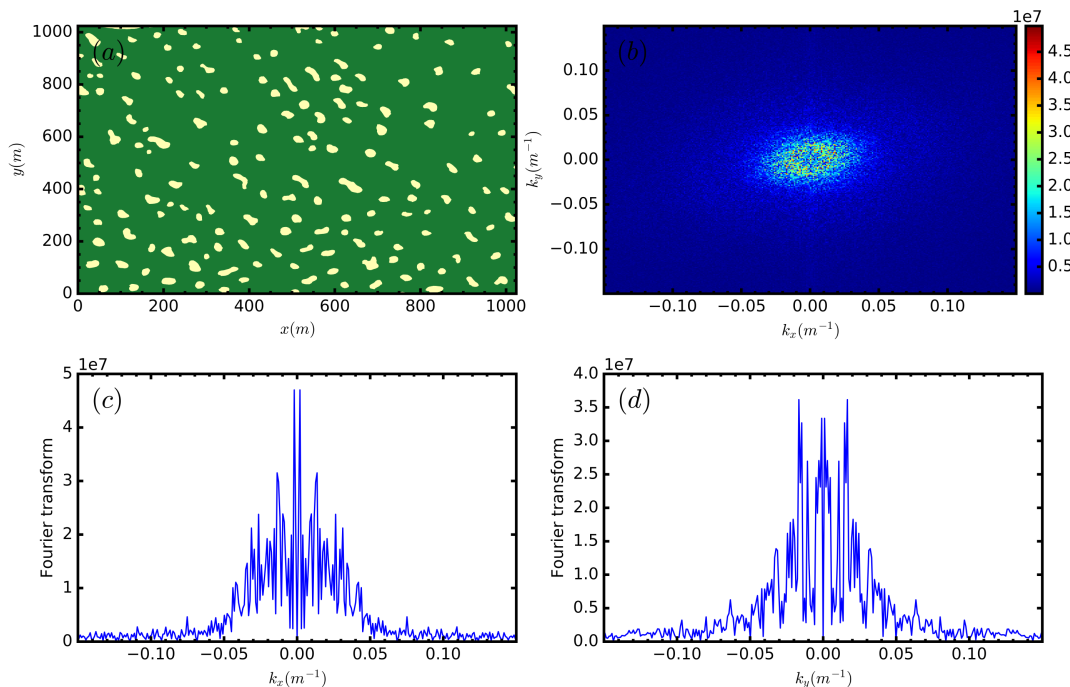
Figure 2.8: Fourier transform of a side-scan cartography image of a rectangular region of a meadow of *P. oceanica*. Panel (a) shows the presence (absence) in green (yellow) of Posidonia in a portion of a meadow. Panel (b) shows the Fourier transform of panel (a). Panels (c) and (d) are cuts at $k_y = 0$ and $k_x = 0$ respectively of panel (b) showing clear peaks at $|k| \approx 0.017$.

nonlinearities, the linear calculation provides a good estimation. As we can see in Fig. 2.9, the wavelength depends almost linearly with σ_κ, facilitating the inference of the competition length. Thus, this result allows us to conjecture a competition length around $20 - 30\ m$, which points to mechanisms related with water movement as the responsible of mediating this competition. We select then $\sigma_\kappa = 2851.4\ cm$ ($\sigma_\kappa = 28$ in adimensional units).

As a result of the selected interaction distances, the kernel has the shape of an inverted mexican hat, being cooperative for short distances and competitive for large distances. Since the strength of competition and facilitation are determined by ω_{d0} and κ and the two Gaussians are normalized, only the contribution of facilitation is noticeable, on the contrary competition that spreads over large distance has a minor amplitude in each location. Although the effect of competition is small at each position the integrated contribution is not negligible, as can be seen in Fig. 2.10. One can also notice using the Fourier transform of the kernel the important effect of competition damping small wave number amplitudes, which has a direct

Table 2.1: Coordinates of analyzed regions and measured wave number. The table shows the coordinates of the vertices of the rectangular regions used to measure the characteristic wave length of patterns in Posidonia meadows an the associated wave number.

Lat_0	Lon_0	Lat_1	Lon_1	Wave number (m^{-1})
39°52'58.5"N	3°07'43.2"E	39°52'25.2"N	3°08'26.2"E	0.017
39°53'31.8"N	3°05'33.9"E	39°52'58.6"N	3°06'16.9"E	0.018
39°53'31.8"N	3°06'17.0"E	39°52'58.5"N	3°07'00.1"E	0.015
39°49'55.6"N	3°09'52.1"E	39°49'22.4"N	3°10'35.1"E	0.016
39°48'49.2"N	3°10'13.4"E	39°48'15.9"N	3°10'56.4"E	0.015
39°47'09.6"N	3°09'08.6"E	39°46'36.4"N	3°09'51.6"E	0.020
39°47'09.6"N	3°09'51.7"E	39°46'36.3"N	3°10'34.6"E	0.019
39°47'11.0"N	3°10'34.7"E	39°46'36.2"N	3°11'17.7"E	0.019
39°45'46.4"N	3°11'39.1"E	39°45'13.1"N	3°12'22.0"E	0.011
39°45'29.7"N	3°12'22.1"E	39°44'56.4"N	3°13'05.0"E	0.010
39°45'46.3"N	3°12'22.1"E	39°45'13.0"N	3°13'05.0"E	0.015
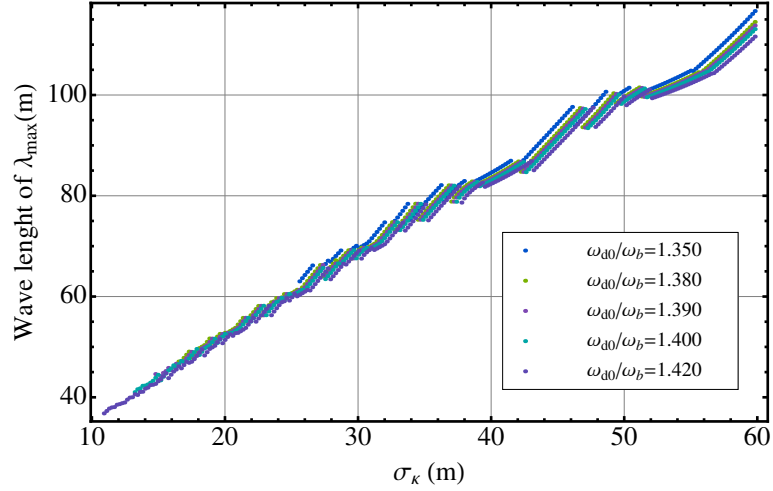
Figure 2.9: Wavelength of the maximum growth rate as a function of the competition range σ_κ for five different values of the intrinsic mortality ω_{d0}. The parameters are $\omega_b = 0.06$ $year^{-1}$, $\nu = 6.11$ $cm/year$, $\rho = 2.87$ cm, $\phi_b = 45$, $b = 1.25$ $cm^4 year^{-1}$, $\kappa = 0.048$ $year^{-1}$, $a = 27.38$ cm^2, and $\sigma_\mu = 203.7$ cm.

effect in the dispersion relation of the system and hence in the critical wave number.
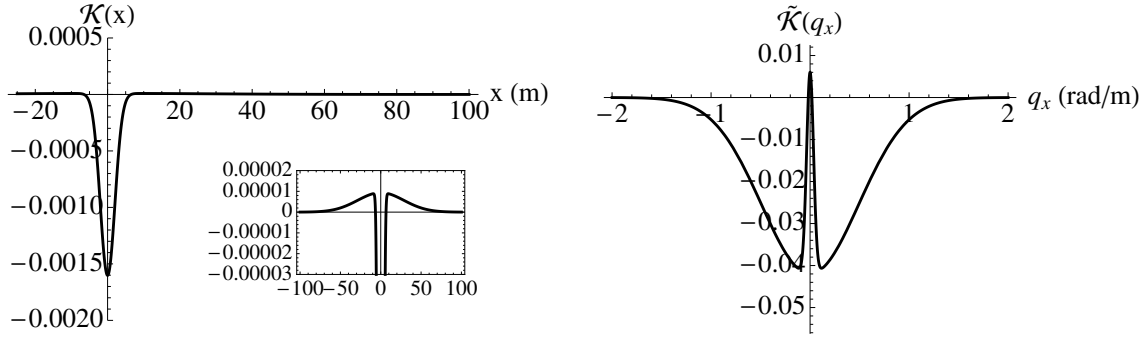
Figure 2.10: Shape of the kernel $\mathcal{K}(\vec{r})$ in real space (left) and Fourier space (right). A cut in the x and q_x directions for $y = 0$ and $q_y = 0$ is shown respectively. Here $\kappa = 0.048$ $year^{-1}$, $\omega_{d0} = 0.042$ $year^{-1}$, $\sigma_\kappa = 2851.4$ cm, and $\sigma_\mu = 203.7$ cm.

2.4 Landscapes of patterns aproaching to the coast

Posidonia oceanica forms meadows between depth limits of $5 - 40$ m. Close to the shoreline high hydrodynamism prevents the growth of new shoots while the limitation of the growth in deep regions is due to a decrease in the availability of light, which reduces photosynthetic activity [89]. Thus, in intermediate regions the meadow develops in suitable conditions. In relation with the model, high mortality regimes are found close to the shore and for deep waters. Hence, smooth increase of mortality close to the coast is expected to explore different regions of the phase diagram where different patterns are expected to appear. We introduce this mortality dependence and perform numerical simulations in order to reproduce the observed landscapes in the meadows. Two elements are necessary to reproduce the spatial distribution of vegetation approaching the coast. First, a mortality profile $\omega_{d0}(x, y)$ where x represents the distance to the coast and y the parallel direction. In order to introduce a mortality profile properly in the simulations we have to take into account two things: i) we have to introduce a matrix with the values of mortality at each position, and ii) since the pseudospectral method needs periodic boundary conditions the introduced profile must be periodic. In the center the profile can have the desired shape but opposite boundaries must connect smoothly. The easiest way to produce a profile is to design it using straight lines and apply a filter to smooth out the corners. For the last step we use a diffusion operator in Fourier space. We apply the Fourier transform to our array and we multiply each component $\vec{q}$ by the diffusion operator, given by $e^{-q^2 t}$, where t controls the softness level. After that we anti-transform to real space. The resulting profile will preserve the initial qualitative shape, but it will be smooth and periodic. The second element to introduce in the simulations is spatial randomness that mimics irregular spatial variability of the parameters due

to the variable conditions at the sea bottom. Spatial noise prevents perfect circular holes or spots to be formed reproducing in a better way the landscapes observed in nature. The generation of spatial noise is done according to the following expression:

$$\chi(x,y) = \mathcal{F}^{-1}\left\{ e^{\frac{-q^2 s^2}{2}} e^{-i2\pi u} \right\} \tag{2.12}$$

where $\mathcal{F}^{-1}$ is the inverse Fourier transform, q is the modulus of the wavevector of each Fourier component, and u is a random number between 0 and 1 with a flat probability distribution. The parameter s controls the typical spatial scale of noise. The Gaussian shape in Fourier space inhibits long wavelength contributions, in such a way the noise is reasonably smooth. In our simulations we take $s = 101.83m$. Fig. 2.11 shows the spatial variability of the noise that is added to the mortality profile with a certain amplitude in each case. The colored noise generated in this way shows
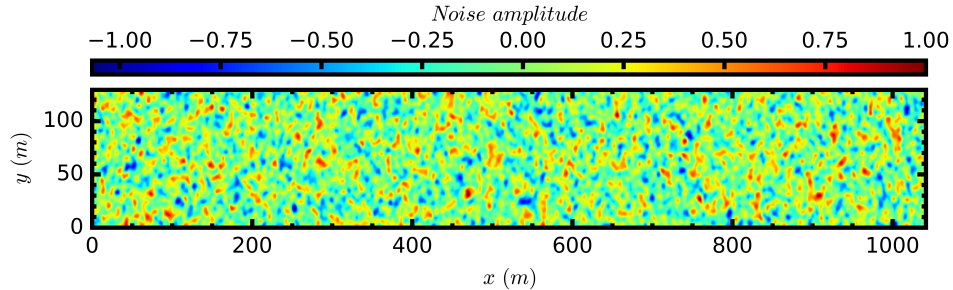

Figure 2.11: Example of the noise distribution used in the numerical simulations. We take $s = 101.83$ m and the number of grid points used in each direction is $N_x = 1024$, $N_y = 128$.

a variability closer to expected one for the seabottom as compared to white noise.

As a result of including a mortality profile reproducing the mortality increase approaching the coast, the numerical simulations reproduce quite accurately the observed features of the spatial distribution. Notice, that patterns in small domains develop a perfect spatial order, on the contrary large domains present more irregular arrangements of the pattern (Fig. 2.12). Elongated vegetation gaps near the shore are present indicating that gaps are close to become unstable to stripes before the sudden increase of mortality very close to the shore. Moreover, scattered gaps close the homogeneous meadow, where there is coexistence of the homogeneous with the hexagonal gaps, are compatible with the formation of localized structures, or fairy cicles. Fig. 2.12 shows a comparison of side scan cartography with numerical simulations.

Another important feature the model can reproduce is the variability of the density measurements approaching the coast observed in meadows along the littoral of
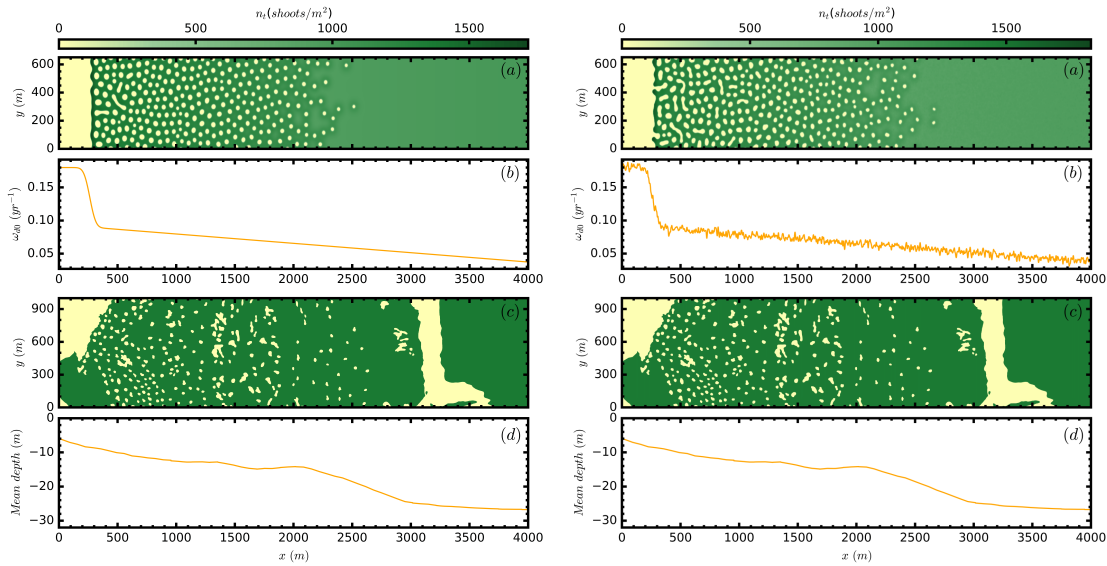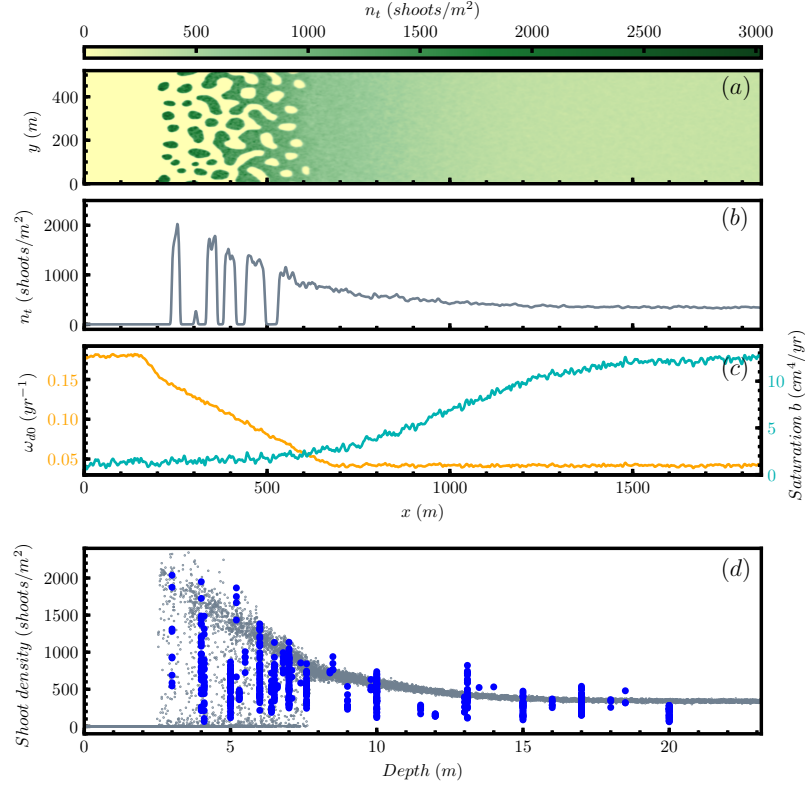
Figure 2.12: Comparison of numerical simulations with patterns in real meadows in absence of noise in the profile (left) and with noise (right). Panel (a) shows the final spatial density distribution of shoots obtained from a numerical simulation of the model in the presence of the mortality profile plotted in panel (b) with the same parameters as in Fig. 2.5. (c) Observed coverage of *P. oceanica* from LIFE Posidonia side-scan cartography in the Balearic coast area limited by the following coordinates: 39° 45'54.1"N 3° 09'49.5 E; 39° 47'25.6"N 3° 11'48.7 E; 39° 47'48.6"N 3° 11'19.0 E; and 39° 46'17.1"N 3° 09'19.9 E. Panel d) shows the mean depth of the water in this region averaged over the y direction.

the Balearic Islands (Fig. 2.13d). Scuba divers measured shoot density at random positions in the meadows without previous knowledge of their spatial distribution. The results consistently showed low shoot density variability at depths $> 10\ m$ compared to high variability at shallower depths ($< 10\ m$), which range from close to 0 to 2000 $shoots/m^2$, a variability much larger than in deeper regions (thick blue dots Fig. 2.13d). The model suggests that the variability associated to density of shoots in shallow waters is a consequence of the presence of complex spatial patterns near the coast. Numerical simulations using as previously noisy and depth-dependent mortality, capture the dispersion of the density close to the coast where patterns form. An additional spatially dependent $b(x, y)$ (see Fig. 2.13c) is considered in these case to account for the decrease in shoot density with depth.

The model also reproduces complex patterns in meadows of *Cymodocea nodosa*, such as the transition from holes to patches observed in one of the meadows (Figs. 1.3, and 2.14c). Because this transition occurs parallel to the coast, that is, at a uniform depth, we infer this pattern to be derived from a sudden increase in the mortality rate along the shore (see Fig. 2.14b). The resulting simulated pattern (Fig.

29

Figure 2.13: Comparison of a numerical simulation with field density measures: (a) Spatial density distribution of *P. oceanica* as obtained from numerical simulations with a custom spatially dependent mortality [orange line in (c)), left scale] and a profile of the saturation strength $b(x,y)$ [blue line in (c), right scale]. (b) Cut of (a) at $y = 102$. (d) Observed *P. oceanica* density measured by scuba divers as a function of depth for different locations spread over the coastline of the Balearic Islands and the density in random locations of the numerical simulation shown in (a) (gray). Parameters as in Fig. 2.5.

2.14a) reproduces very well the observed features of the real meadow, being particularly interesting the effects of the time evolution in the resultant pattern. Holes form from a homogeneous initial condition, while the region with high mortality loses all vegetation at the beginning. From the created front new patches start to develop creating a front that advances covering all the available space with patches and elongated shapes aligned with the direction of growth. Elongated patches are also visible in the cartography giving validity to the model and describing how colonization of this region occurred.

The calibration for *C. nodosa* is equivalent to one presented for *P.oceanica*. The parameters related to clonal growth are well determined in the literature [90, 94] $\omega_b = 2.3 \ year^{-1}$, $\nu = 160 \ cm/year$, $\rho = 3.7 \ cm$, $\phi_b = 46° \sim 45°$. Those related
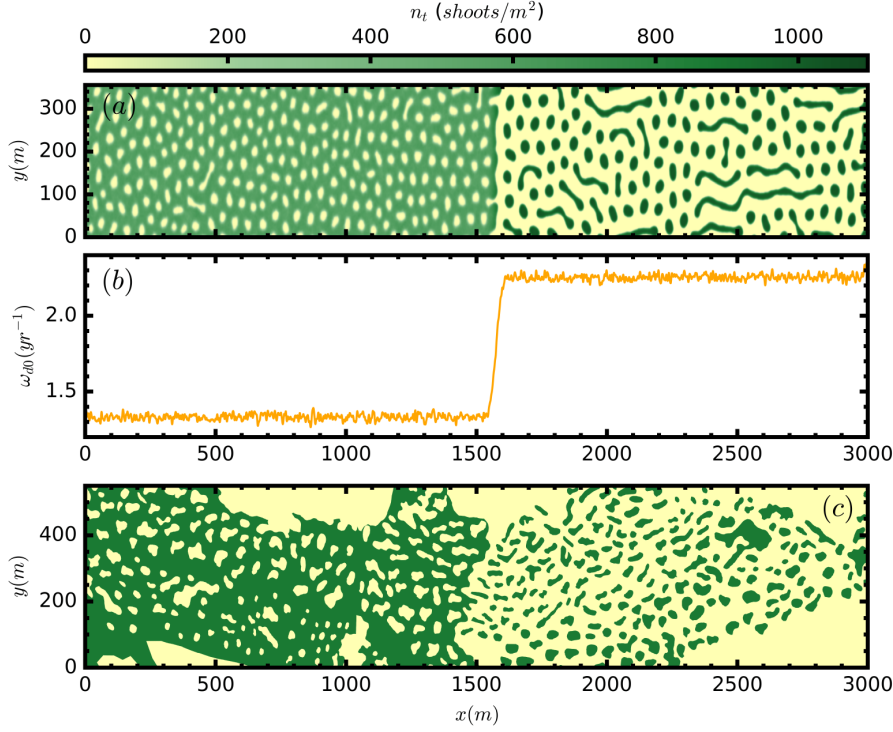
Figure 2.14: Comparison of a numerical simulation with patterns observed by side-scan sonar in a region of coexistence between holes and patches in a meadow of *C. nodosa* in Mallorca Island (Fig.1.3). The set of model parameters for *Cymodocea nodosa* is $\omega_b = 2.3$ $year^{-1}$, $\nu = 160$ $cm/year$, $\rho = 3.7$ cm, $\phi_b = 45°$, $b = 112.71$ $cm^4 year^{-1}$, $\kappa = 2.76$ $year^{-1}$, $\sigma_\kappa = 2226.1$ cm, $a = 21.0$ cm^2, $\sigma_\mu = 139.1$ cm, and the area modeled (a subset of that shown in Fig. 1.3) is bounded by the coordinates: 39° 53'16.4"N 3° 05'12.7 E; 39° 51'52.0"N 3° 06'15.7 E; 39° 51'43.1"N 3° 05'55.6 E; 39° 53'07.5"N 3° 04'52.6 E. (a) Final spatial density distribution of shoots from a numerical simulation of the ABD model using the mortality profile shown in (b). (c) Observed coverage of *C. nodosa* from LIFE Posidonia side-scan cartography in the Balearic coast.

to the homogeneous solution and nonlocal interactions are as follows. $b = 112.71$ $cm^4 year^{-1}$ is chosen to have shoot density around 1000 $shoots/m^2$. There is no particular reason, apart from having a similar wavelength, to choose different values of the other three parameters, as similar results are expected for different values. Then, we take $\kappa = 2.76$ $year^{-1}$, $\sigma_\kappa = 2226.1$ cm, $a = 21.0$ cm^2, $\sigma_\mu = 139.1$ cm. It is important to chose the mortality values on the spatial profile in order to select the appropriate patterns in each region.

2.5 Distribution of growth directions

The ABD model, as explained in the previous sections, describes not only the spatial distribution but the distribution of apices in the angle of growth ϕ. Effectively the model is 3D and numerical simulations with fine discretization are computationally costly. For this reason we choose the minimal discretization compatible with the branching angle. Nevertheless, this situation is artificial and can not describe properly the situation in which the branching angle is not an integer fraction of 2π, neither fluctuations in the direction of growth. Not to mention solutions which have heterogeneous density of apices in the angle, which the angular discretization is not capable of resolving. Here we investigate heterogeneous growth direction distributions in the apices density. We analyze the problem for different branching angles using the linear stability analysis, whereas we perform numerical simulations focusing primarily on $\phi_b = 49° \sim 45°$, which corresponds to the case of *P.ceanica* but it is not limited to this species [94]. Usually most of them range between 30° - 60°. Hence, in this case the minimal discretization is with eight growth directions only. Nevertheless, this minimal discretization is not compatible with solutions modulated in the angle with an azimuthal wave number $q_\phi > 4$. From this perspective, understanding the dynamics in the angle is necessary to determine if heterogeneous solutions can emerge from the intrinsic growth of the plant or on the contrary it is justified to use a minimal approach to describe the growth in space.

2.5.1 Distribution of growth directions in the spatially homogeneous solutions

Two terms depend explicitly on the angle: the branching and the advection. The main parameter that determines the behavior of the system from the perspective of the angular distribution is the branching angle ϕ_b. In other words, ϕ_b is the main scale of the problem in the angle. This fact has its manifestation in the stationary solutions. On the one hand, the stationary homogeneous solutions in space determines the value of the total density n_t^* given by Eq. (2.9). Moreover, the value of n_s^* and N_a^* are also fixed according to the relations in (2.10). On the other hand, stationary solutions heterogeneous in the angle can be found, where one can distinguish two cases. When the branching angle is commensurable with 2π, $\phi_b = 2\pi/m$ ($m = 8$ in the case of 45°), the stationary solutions take the form $n_a^*(\phi) = N_a^*/2\pi + \sum_n b_{q_{\phi,n}} e^{iq_{\phi,n}\phi}$, where $q_{\phi,n} = nm$ with $n = 1, 2, 3...$. Consequently, these solutions can have any distribution of apices in the angle as long as the density of apices is periodic with ϕ_b and the total density of apices is fixed to N_a^*. On the contrary, for the incommensurable case the only stationary solution is the homogeneous in the angle $n_a^*(\phi) = N_a^*/2\pi$. Thus, a linear stability analysis of the stationary solutions homogeneous in space against
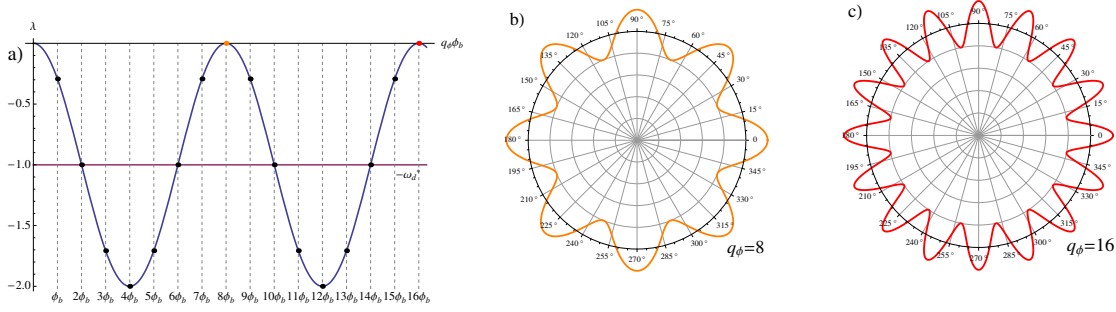
Figure 2.15: Linear stability. Panel a) shows the growth rate λ (blue line) of modulations of the density of apices in the angular dimension with wavenumber q_ϕ for solutions homogeneous in space. Dashed lines indicate modes compatible with the system size 2π. The solid orange and red points correspond to the neutral modes shown in panels b) an c) respectively.

perturbations of the form $e^{iq_\phi\phi}$ with $q_\phi = 1, 2, 3...$ and $q_\phi \neq 0$, leads to the following growth rate, for both the unpopulated and the populated solutions

$$\lambda(q_\phi) = \cos(q_\phi\phi_b) - \omega_d^*, \tag{2.13}$$

where $\lambda(q_\phi)$ corresponds to the eigenvalue of the mode with azimuthal wavenumber q_ϕ expressed in adimensional units. ω_d^* corresponds to the stationary and homogeneous value $\omega_d^* = \omega_d(n_t^*)/\omega_b$. For the unpopulated solution $\omega_d^* = \omega_{d0}/\omega_b$, and for the populated one $\omega_d^* = 1$.

For the stability around the unpopulated solution $n_t = 0$, on the one hand, if the branching rate is smaller than the mortality rate, all modes have negative real eigenvalues and any small perturbation decays. On the other hand, in the case $(\omega_b > \omega_{d0})$, we distinguish between two cases. First, if the branching angle is incommensurable with 2π, the unpopulated solution becomes unstable at $\omega_b = \omega_{d0}$ being the homogeneous mode with eigenvalues $\lambda = -\omega_d^*, 1 - \omega_d^*$ the first one that becomes unstable, leading after the transition to a homogeneous solution where all directions of growth have the same density. Modulated perturbations have $\cos(q_\phi\phi_b) < 1$, and therefore growth rates smaller than the growth rate of the homogeneous mode. On the contrary, if the branching angle is commensurable with 2π, $\phi_b = 2\pi/m$, at $\omega_b = \omega_{d0}$ all modes with $q_{\phi,n} = n2\pi/\phi_b$, with $n = 1, 2, 3\ldots$ become simultaneously unstable. Thus, above threshold, the solution bifurcating at $\omega_b = \omega_{d0}$, can be written as $n_a^*(\phi) = N_a^*/2\pi + \sum_n b_{q_{\phi,n}} e^{iq_{\phi,n}\phi}$ which is homogeneous in space but not necessarily in the angle. Any arbitrary combination of amplitudes $b_{q_{\phi,n}}$ will be a solution provided the total density of apices N_a^*, given by b_0, takes the proper value determined by n_t^*. In Fig. 2.15b,c we can see two of these modulations. We impose also that not n_a

nor n_s can take negative values, which limits the amplitudes $b_{q_{\phi,n}}$. This degeneracy can be understood easily considering sets of m directions separated by the branching angle ϕ_b. Since the only coupling in the angle is introduced by the branching process any set is uncoupled from the other, hence, any arbitrary combination of these sets is a valid solution provided the total density N_a is fixed. In other words, if one considers the density between ϕ and $\phi + \phi_b$ where each position correspond to the first direction of a different set, the density of apices must repeat after $\phi + \phi_b$ because the second direction of the sets is separated ϕ_b. As a result, since the density between ϕ and $\phi + \phi_b$ is free, the distribution of apices in the angle is not fixed as long as it is periodic with ϕ_b. Depending on the initial condition and if the system is deterministic, the populated solution homogeneous in space appearing above threshold will not necessarily be homogeneous in the angle. The effects of noise can have, however, important consequences which will be considered later.

The distinction between the incommensurable and commensurable case is also necessary when looking at the stability of the populated homogeneous solution. In the first case, all perturbations around the homogeneous solution, which is the only solution in this case, have negative eigenvalues and decay with time. The growth in all directions is equivalent and as a result the populated solution is stable.

In the commensurable case instead, the solution may not be necessarily homogeneous in the angle. Nevertheless, the linear stability analysis (2.13) is independent of the particular stationary solution. Thus, both homogeneous and heterogeneous solutions in the angle are stable. However, there is set of neutral modes, which do not grow nor decay (Fig. 2.15). These modes are precisely those with an azimuthal wavenumber multiple of $2\pi/\phi_b$ ($q_{\phi,n} = n2\pi/\phi_b$ where $n = 1, 2, 3...$). For *P. oceanica* $q_{\phi,n} = 8, 16, 32....$ It is not surprising that perturbations that belong to the eigenfunctions of the stationary solution are neutral since a stationary solution plus a perturbation of this kind is also a stationary solution. Giving a more physical interpretation, one can redistribute the density of apices among the different sets of m directions of growth at no cost, as long as the sum remains constant and the final distribution has the periodicity given by the branching angle. The presence of neutral modes, which appear due to the breaking of the rotational symmetry, have important consequences under the effect of noise.

2.5.2 The role of noise

The effect of noise on the neutral modes has an important role in restoring the symmetry and leading the meadow to the homogeneous configuration in the angle. We explore these effects in the commensurable case where neutral modes are present. The complete model including spatial dynamics is highly demanding, for this reason we focus on the homogeneous case in space preserving the dependence with the angle,

in such a way that we can increase the resolution in this dimension with a reasonable computational cost. The ABD model with no space and with noise takes the form:

$$\partial_t n_a(\phi, t) = \frac{\omega_b}{2} \left(n_a(\phi + \phi_b, t) + n_a(\phi - \phi_b, t) \right)$$
$$-\omega_d n_a(\phi, t) + \sqrt{\epsilon} \xi(\phi, t) \tag{2.14}$$

$$\partial_t n_s(t) = -\omega_d n_s(t) + \frac{\nu}{\rho} \int_0^{2\pi} n_a(\phi, t) d\phi \tag{2.15}$$

$$\omega_d(n_t) = \omega_{d0} + (\kappa - \omega_{d0})(1 - e^{-an_t}) + bn_t^2, \tag{2.16}$$

where $\xi(\phi, t)$ represents a white Gaussian noise with zero mean, variance one, and delta correlated in the angle and in time. ϵ is the strength of the noise. Fluctuations in the dynamics can be the result, for example, of the variability of the branching, leading to an additional multiplicative noise term, which we do not consider for simplicity. Additive noise is justified in the regimes where average density is large and fluctuations are small, which is the case in all the cases we consider, as we analyze the evolution close to the populate homogeneous solution. We have not considered noise in the equation of the shoots (2.15) since shoot population is derived directly from the density of apices.

We perform numerical simulations with $N = 16$ and $N = 256$ directions starting from two initial conditions, a non-uniform and a uniform distributions. The first consists of the homogeneous stationary solution, whereas for the second we add a modulation with $q_\phi = 8$ in the growth direction, as the one shown in Fig. 2.15b. Average densities and standard deviations are computed from 1000 realizations of the noise for each growth direction and for the real part of the Fourier modes. The amplitude of each mode is computed using the discrete Fourier transform. In Figs. 2.16 and 2.17 we represent the time evolution of the standard deviations and average values respectively. It is important to notice the discrete Fourier transform encompasses the amplitude of b_n and b_{-n} in the last mode for technical purposes, therefore, it is necessary to correct by a factor of two the amplitude of the last mode which is represented in Fig. 2.16. Equivalently, since we use a pseudospectral method, fluctuations in real space are also affected, being the effect more pronounced in Fig. 2.16a, where the major contribution to the fluctuations in real space is due to the fluctuations of the last mode. Consequently we have corrected the prediction for the fluctuations in real space.

Starting with an homogeneous initial condition facilitates the analysis of the evolution of the fluctuations. The standard deviation of the amplitude of all Fourier modes grow initially with time, quickly damped modes saturate following an Ornstein-Uhlenbeck process with zero mean and variance $\frac{\epsilon}{2\pi} \frac{1-e^{2\lambda t}}{-2\lambda}$, where λ corresponds to the eigenvalue. On the contrary, the variance of the neutral modes grows in time as $\frac{\epsilon t}{2\pi}$ following a diffusive process of zero mean. Essentially, fluctuations in real space are
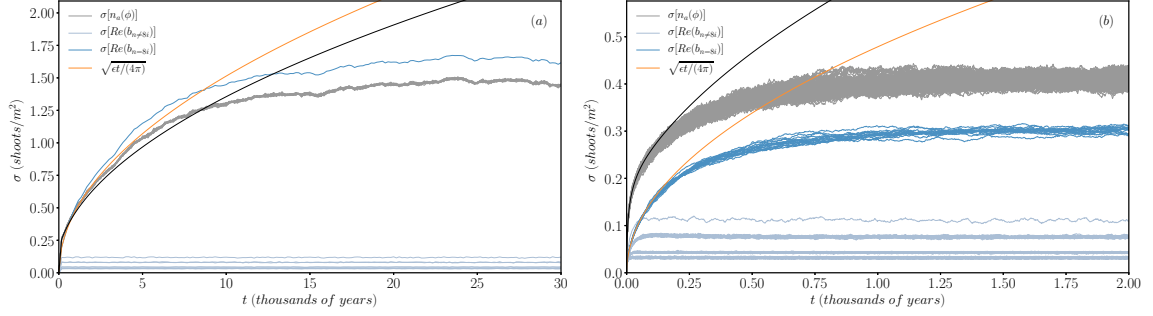
Figure 2.16: Evolution of the standard deviation of the density fluctuations in real and Fourier space. Panel a) corresponds to a numerical discretization $N = 16$ directions, while panel b) $N = 256$, using in both cases 1000 realizations of the noise to compute averages. The standard deviations of the fluctuations in each direction $n_a(\phi)$ are represented in gray. The real part of the amplitudes of the Fourier modes is shown in dark blue for the neutral modes and in light blue for the damped modes. The orange curve is the theoretical prediction of a diffusive process, while the black line corresponds to the theoretical prediction accounting for all the Fourier modes, neutral and damped. Parameters are $\omega_b = 0.06$ $year^{-1}$, $\omega_{d0} = 0.03$ $year^{-1}$, $\nu = 6.11$ $cm/year$, $\rho = 2.87$ cm, $\phi_b = 45°$, $b = 1.25$ $cm^4 year^{-1}$, $\kappa = 0.048$ $year^{-1}$, $a = 27.38$ cm^2 and $\epsilon = 1.728 \cdot 10^{-12}$ $cm^{-4} year^{-2}$

the sum of the fluctuation of all modes, which is clearly dominated by the diffusive process of the neutral modes. As a result of the constraint of positive density, the fluctuations deviate from a perfect diffusive process saturating at $\sigma = \sqrt{\frac{\Delta\phi}{3} \frac{N_a^*}{2\pi}}$, where $\Delta\phi = 2\pi/N$. This limit can be understood considering each growth direction experiences a random walk in a finite interval, where the amplitude is bounded between $[-\frac{N_a^*}{2\pi}, \frac{N_a^*}{2\pi}]$. Therefore, the probability distribution changes in time from a Gaussian to a flat distribution, thus fluctuations are determined by the size of the interval. Fig. 2.16 shows the time evolution of the standard deviation for both discretizations. Note the time scale of the saturation is different for the two discretizations. The fluctuations of each pixel diverge when $\Delta\phi$ goes to zero while the integral of all the noise is independent of the discretization. Thus, fine discretizations have larger fluctuations at each pixel, this together with the constraint of positive density gives as a result a faster saturation of the fluctuations for the case of $N = 256$, mainly because trajectories reach faster to the boundary.

More interestingly is the case starting with a non-uniform initial condition. For $N = 16$ a modulation with $q_\phi = 8$ as initial condition around the homogeneous stationary solution is equivalent to a set of eight directions with density above the average and another set with density below the average. For $N = 256$ instead the modulation is well resolved being a continuous distribution in the growth direction with directions with densities above and below the average. Both cases behave
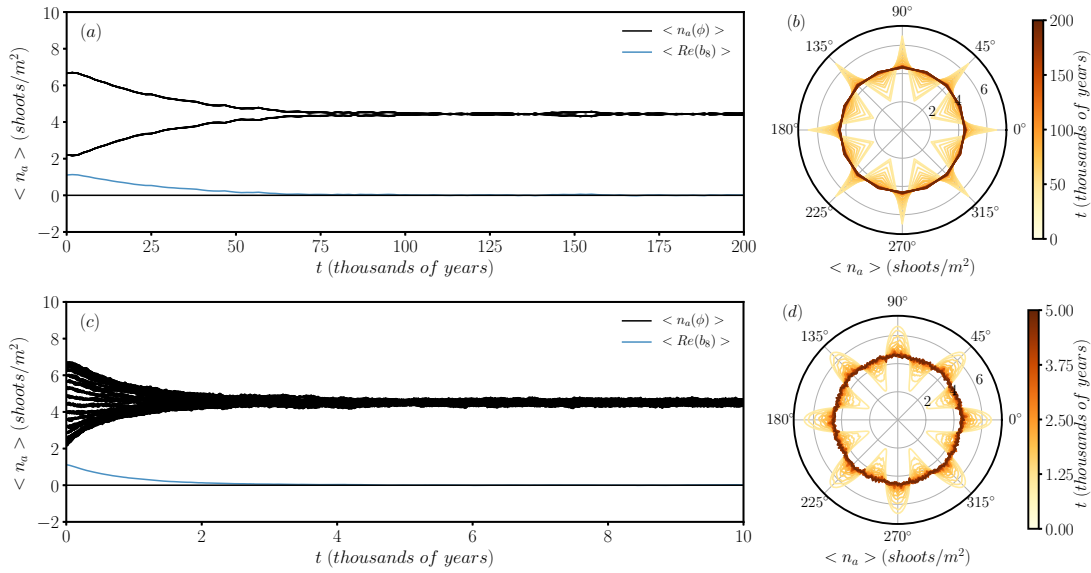
Figure 2.17: Time evolution of the distribution of growth directions. Panel a) and b) correspond to the numerical discretization of $N = 16$ directions of growth. In a) the evolution of the average values of $< n_a(\phi) >$ over 1000 realizations are shown for each direction of growth. Two black curves are visible corresponding to the two sets of 8 directions. The blue curve shows the average of the real part of b_8. Panel b) shows $< n_a(\phi) >$ of each direction, where the colormap indicates the time evolution. Panel c) and d) show the same as in a) and b) for $N = 256$. Parameters as in Fig. 2.16.

similarly. The differences in the densities with ϕ in average vanish with time reaching an homogeneous stationary state. Fig. 2.17 shows the average density for each growth direction as well as the average of the real part of b_8. The figure shows the homogenization of the density with ϕ and accordingly the decay of the mean amplitude of b_8 to zero. Notice the difference between the density in growth directions belonging to the same set are almost null, since these differences are a consequence of the excitation of damped modes. The explanation of the temporal decay of the amplitude of the modulation, which leads to the homogeneous solution, can be given in terms of the fluctuations. Initially the neutral modes follow a Gaussian distribution with a mean around the initial condition, as expected for a diffusive process. As time increases, trajectories in different realizations reach the maximum amplitude allowed by the condition of positive density. Thus, the probability distribution changes to a flat distribution with zero mean. Hence, there is a transient in which the mean value decay to zero from the initial value, as can be seen in Fig. 2.17 for the amplitude b_8. As expected, other neutral modes with initial zero mean remain with this value along the time evolution. These results show how the homogeneous configuration is
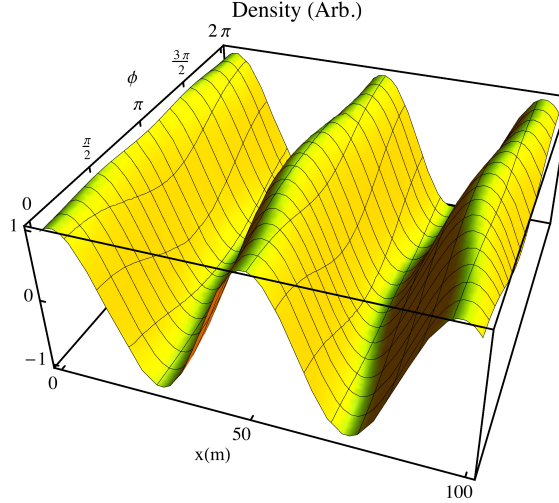
Figure 2.18: Critical eigenmode. Eigenstate corresponding to the critical wave number $q_{x,c} = 0.1357 \ m^{-1}$ showing an angular dependence with periodicity 2π. Parameters are $\omega_b = 0.06 \ year^{-1}$, $\omega_{d0} = 0.0846$, $\nu = 6.11 \ cm/year$, $\rho = 2.87 \ cm$, $\phi_b = 45°$, $b = 1.25 \ cm^4 year^{-1}$, $\kappa = 0.048 \ year^{-1}$, $\sigma_\kappa = 1629.3 \ cm$, $a = 27.38 \ cm^2$, $\sigma_\mu = 203.7 \ cm$.

restored by the presence of noise where perturbations vanish on average due to the presence of neutral modes.

2.5.3 Distribution of growth directions in patterns

For the case of pattern formation it is not possible to obtain an analytical expression of the eigenvalues, mainly because the advection term couples the angular part with the spatial part. However, the linear stability can be performed numerically. As we already know a modulation instability at finite wavenumber $q_{x,c}$ appears. The critical eigenmode not only has a modulation in space but also in the angle. The periodicity does not correspond to any of the neutral modes $q_\phi = 8, 16, 32...$, as in the previous case, but to the periodicity of the system $q_\phi = 1$, as it can be seen in Fig. 2.18. The critical mode presents a clear correlation between the pattern and the modulations in the angle ϕ. As explained at the beginning of the chapter, apices growing in the x direction ($\phi = 0$) are shifted to the right, while apices growing in the $-x$ direction ($\phi = \pi$) are shifted to the left, and equivalently in all the other directions. Although, we can not obtain a closed expression for the eigenvalues it is possible to demonstrate the presence of neutral modes in the case with patterns in space. More precisely one can demonstrate that solutions written as $n_a^*(\vec{x}, \phi)(1 + \delta n_a(\phi))$, where $n_a^*(\vec{x}, \phi)$ is the stationary pattern, are neutral provided $\delta n_a(\phi)$ is a superposition of modes with $q_{\phi,n} = 2\pi n/\phi_b$, and $n_a^*(\vec{x}, \phi)\delta n_a(\phi)$ does not change the total density of apices in a
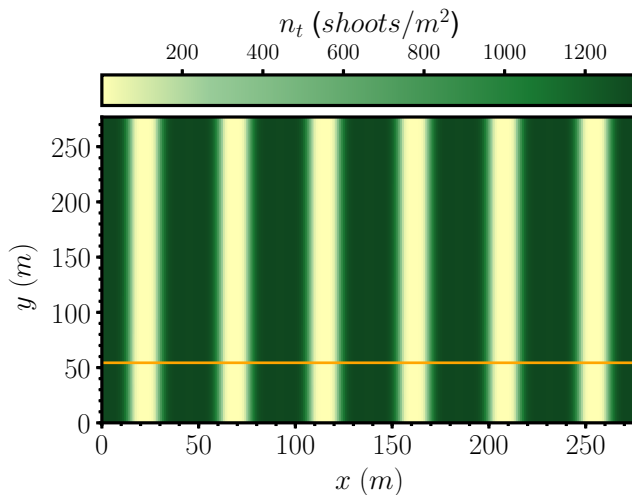
Figure 2.19: Stable solution showing a pattern of stripes with wavenumber $q_{x,c} = 0.1357rad/m$. The total density n_t is shown. The orange line indicates the transect at y constant used in other figures. Parameters as in Fig. 2.18

given position (see Appendix A).

It is straightforward to show this using numerical simulations. We focus in the commensurable case for the solution of stripes pattern, although similar results can be found for positive and negative hexagons. We use the pattern of stripes shown in Fig. 2.19, where in this section a different value of the competition distance has been used for convenience in the numerical simulation. We use the minimal discretization $N = 16$ which allows for the existence of the first neutral mode, in particular the mode with azimuthal wave number $q_\phi = 8$. We design three initial conditions using the pattern in Fig. 2.19 with an extra modulation in the angle $q_\phi = 8$, this allow to determine if these modulated solutions in the angle decay or on the contrary, the modulated distribution is a stationary solution meaning that the density can be redistributed in different directions due to the presence of a neutral mode.

The first initial condition has the intrinsic modulation given by $q_\phi = 1$ associated to the growth of the critical mode above threshold. A transverse cut at y-constant, represented in orange in Fig. 2.19, of the density of apices growing in all directions is shown in Fig. 2.20. As shown previously for the critical eigenmode the maximum of the density is shifted for each growth direction, however the effect is even more pronounced due to nonlinear effects. The second initial condition consists of all the apices redistributed in only one set of 8 growth directions, leaving the densities of the other 8 directions empty. Such initial condition remains stable as shown in Fig. 2.20. Since the branching is not coupling the two sets of 8 directions, no new apices
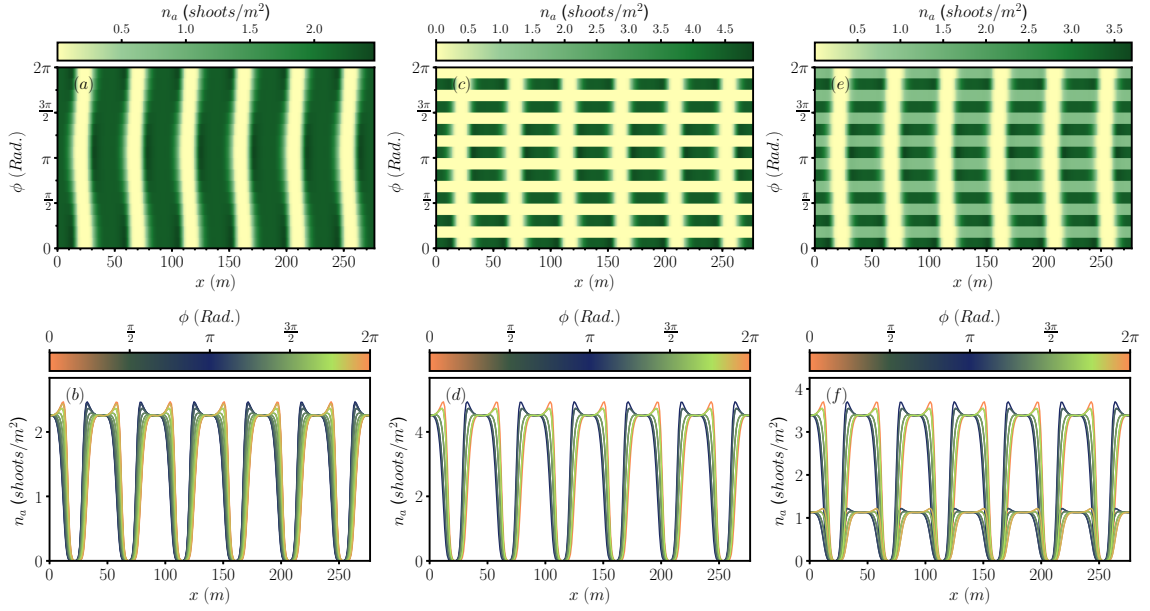
Figure 2.20: Growth direction distributions. All panels show the distribution of growth directions for the patterns of Fig. 2.19, particularly for the cut y constant shown in orange. Panel a) and b) correspond to an initial conditions where all directions of growth have the same density of apices. Panel c) and d) correspond to an initial condition where 8 of the 16 directions of growth have zero density while the other set of eight directions all have the same density of apices. Finally panel e) and f) correspond to an initial condition where one set of 8 directions have 1/4 of the total density of apices and the other set the other 3/4 of the density. The same parameters as in Fig. 2.18 have been used.

appear in the empty directions. Finally we study an initial condition with different densities in both sets of 8 directions, specifically 3/4 and 1/4 of the total density respectively. Such configuration is also a neutral steady state.

The final solutions shown in Fig. 2.20 corroborate the presence of neutral modes which make possible to redistribute the densities of apices in different directions of growth respecting the periodicity of the branching. It is expected that, analogous to the previous section noise will wipe out all modulations in the angle except the modulation inherent to the pattern $q_\phi = 1$ which is robust against noise.

2.6 Conclusions

Along this chapter we have studied vegetation patterns in clonal-growth plant meadows, mainly *P.oceanica*. More precisely we have derived a model from the main mechanisms of growth in clonal behavior based on measured parameters widely ac-

cepted for clonal growth. Introducing long range competitive interactions the model explains the formation of regular patterns as result of Turing or Modulation instability. We have shown that in agreement with pattern formation theory a particular sequence of patterns appears when increasing mortality of the meadow. Being more concrete, patterns of circular holes without vegetation arranged in an hexagonal pattern, stripes and patches arranged in an hexagonal pattern emerge from nonlocal competition. Moreover, isolated circular holes, frequently called fairy circles are explained by the same competitive mechanisms originating pattern formation. In this chapter we have estimated the length of this interaction based on the analysis of LIFEPosidonia cartography giving a competition length around $\sim 20 - 30\ m$, which points to mechanisms mediated through water movement as the explanation of long-range competition. Beyond, explaining pattern formation in *P.oceanica* meadows the model reproduces landscape features of meadows when approaching the coast. As a matter of fact, much higher density variability close to the shore is also compatible with the formation of a pattern. In the last part we have focused in a more technical question regarding the distribution of growth directions. Independently of the branching angle the systems reaches the homogeneous configuration either because of ϕ_b being incommensurable with 2π, or because external fluctuations and the presence of neutral modes lead to homogenization. Interestingly the only heterogeneity in the growth direction is associated to the formation of a pattern, leading to maximum density of apices in the direction facing outwards the meadow. Hence, the model only needs the minimal discretization compatible with the branching to reproduce properly the spatial distributions of vegetation in large regions. From this perspective the model is specially suitable for landscape prediction and as a diagnostic tool based on cartographic data. Beyond that, the description presented in this chapter provides a useful framework to study the effects of environmental changes in the growth of the meadows. Similarly to the analysis of the spatial distribution close to the coast, the model can be used to explore the effects of climatic change on the spatial configuration of the meadows, it can be expected to find a shift of the patterns to different depth due to the increase of sea level. Additionally, temperature rise may lead to an increase in mortality having an important effect on plant development. From this perspective the model opens new possibilities of research.

CHAPTER 3

Derivation of a simplified model for clonal growth

The ABD model provides a description of the growth of clonal plants with great detail, accounting explicitly for the density of apices in different directions and shoots. With this model it is possible to explore the dynamics of the system, find stationary states with heterogeneous spatial distribution and determine the response of the meadows in realistic condition. However, the model has important disadvantages when trying to address more theoretical questions. Both from the numerical and analytical perspective the complicated form of the model limits the possible results. Being more precise, the linear stability analysis, one of the easiest calculations one can perform, does not have an analytical expression already, not to mention using more advanced methods. Moreover, continuation methods which allow the numerical tracking of stationary solutions to obtain unstable parts of the solution branches, which are very important for the dynamics, are also inaccessible. These methods rely on the calculation of the Jacobian, which grows as N^2 being N the number points used for describing the field. For the ABD model the Jacobian needs huge amounts of memory, which slows down the computation dramatically. The ABD model is a big improvement regarding landscape prediction, however, better performance is expected for approaches which do not have to account for apices in different directions [13, 23, 15, 115]. Besides, in the previous chapter we have shown the minor effect the angular part has in the process of pattern formation, where the typical evolution is reaching a homogeneous distribution in the growth direction. The only relevant aspect appears when a pattern in space forces a modulation in the angle generally producing more apices growing outwards the meadow than inwards. Thus, it seem feasible to find a simpler model which only accounts for the total density of apices in space. Immediately, one thinks in integrating the angle $n_a(\vec{r}, \phi, t)$ to obtain $N_a(\vec{r}, t)$ and sum it to shoot density $n_s(\vec{r}, t)$. However, the integral of the advection term can

not be expressed in terms of the total density of apices $N_a(\vec{r}, t)$, so this fact prevents obtaining straightforwardly a closed equation for $n_t(\vec{r}, t)$. In this chapter we attempt to derive an equation for the total density that captures all the relevant dynamics of the full model.

The chapter is organized as follows: In the first section the derivation of a simplified model is presented. This section is separated into two parts, the first part devoted to the derivation regarding clonal-growth mechanisms and the second to the moment expansion. In the second section the simple model is analyzed with the linear stability analysis of the homogeneous solution and using continuation techniques to obtain the branches of localized structures in one dimension and patterns.

3.1 Systematic derivation of a simplified equation

Two different kinds of approximations can be done in order to simplify the model. The first approximation focuses on the simplification of the directional growth given by the advection term to end up with one equation for the total density and avoid the dependence on ϕ. Second, the kernel which accounts for interactions is approximated using a moments expansion. While the first approximation affects the part of the model which is based on the experimentally validated mechanisms of growth, the second one affects only the part of interactions across space where the leading mechanism remains to be clarified.

3.1.1 Simplification of clonal-growth terms

In order to discard the dependence on the angle and describe only the total density one must write first the density of apices as a Fourier series in the angle $\phi \in \{0, 2\pi\}$:

$$n_a(\vec{r}, \phi, t) = \frac{a_0(\vec{r}, t)}{2} + \sum_{n=1}^{\infty} a_n(\vec{r}, t)\cos(n\phi) + b_n(\vec{r}, t)\sin(n\phi), \qquad (3.1)$$

where $\pi a_0(\vec{r}, t) = N_a(\vec{r}, t)$ given that $a_n(\vec{r}, t) = \frac{1}{\pi}\int_{-\pi}^{\pi} n_a(\vec{r}, \phi, t)\cos(n\phi)d\phi$ and $b_n(\vec{r}, t) = \frac{1}{\pi}\int_{-\pi}^{\pi} n_a(\vec{r}, \phi, t)\sin(n\phi)d\phi$ by definition. Thus, using Eq. (2.3) one can find the evolution equations for all amplitude modes a_n, b_n. This gives a hierarchy of infinite coupled equations between them in such a way that modes n are coupled to the modes $n + 1$.

$$\partial_t a_0 = (\omega_b - \omega_d(n_t))a_0 - \nu \nabla \cdot (a_1, b_1), \tag{3.2}$$

$$\partial_t a_n = (\omega_b \cos(n\phi_b) - \omega_d(n_t))a_n$$
$$- \frac{\nu}{2}\vec{\nabla} \cdot (a_{n+1} + a_{n-1}, b_{n+1} - b_{n-1}), \tag{3.3}$$

$$\partial_t b_n = (\omega_b \cos(n\phi_b) - \omega_d(n_t))b_n$$
$$- \frac{\nu}{2}\vec{\nabla} \cdot (b_{n+1} + b_{n-1}, a_{n-1} - a_{n+1}). \tag{3.4}$$

From numerical simulations and the linear stability analysis one can see that modes with $n > 1$ are not contributing much to the dynamics, meaning that $\frac{a_2}{a_1}, \frac{b_2}{b_1} <<$ 1 as can be seen in Fig. 3.1, and these terms can be neglected. We define at this stage the vector $\vec{a} = (a_1, b_1)$ in terms of the amplitudes of the first mode. The first approximation is then to neglect terms higher than the first order in such a way that we reduce an infinite set of coupled partial differential equations to four describing n_s, a_0, a_1, b_1, where the second one can be transformed easily to an equation for N_a using $\pi a_0 = N_a$.
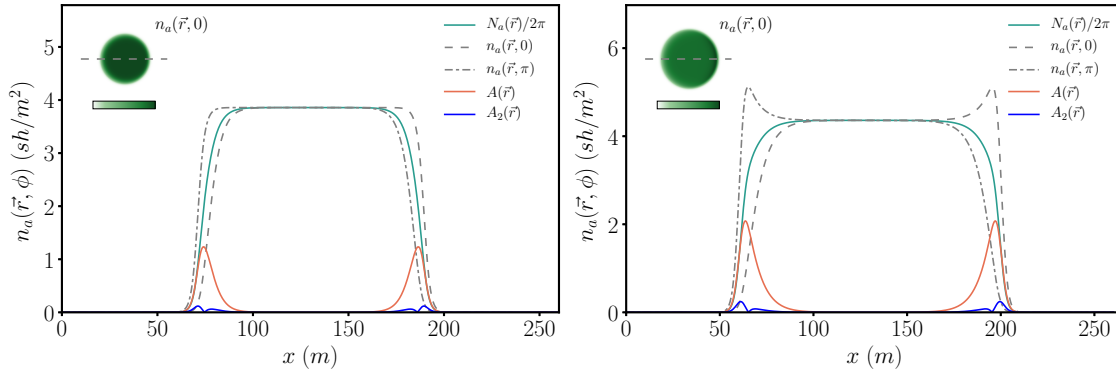
Figure 3.1: Density of apices of a circular front invading the unpopulated solution for the ABD model with $\omega_{d0} = 0.072 \ year^{-1}$ (left) and $\omega_{d0} = 0.038 \ year^{-1}$ (right). Other parameters are the same in both panels, $\omega_b = 0.06 \ year^{-1}$, $\nu = 6.11 \ cm/year$, $\rho = 2.87 \ cm$, $\phi_b = 45°$, $b = 1.25 \ cm^4 year^{-1}$, $\kappa = 0.048 \ year^{-1}$, $\sigma_\kappa = 0 \ cm$, $a = 27.38 \ cm^2$, $\sigma_\mu = 0 \ cm$, $\mu = \omega_{d0}$. The inset in green represents the density in space of apices growing right where the dashed line represents the plotted cut. Green line represents the mean density of apices in the angle ($N_a/2\pi$). Dashed lines represent apices growing right and left according to the legend. Red and blue lines shows the amplitude of the first mode and second mode respectively.

As a second approximation one can make the assumption that the relation in (2.10) between apices and shoots for the homogeneous stationary case is valid for all

$\vec{r}$ and t. Since mortality rate is equivalent for both densities and advection does not create plants, it is reasonable to think that the relation between apices and shoots will be given by the respective rates of birth, which imply precisely the relation in 2.10 and we rewrite as $N_a(\vec{r}, t) \approx \eta n_t(\vec{r}, t)$ where $\eta = \frac{\rho \omega_b}{\nu + \rho \omega_b}$. It is clear that this relation is not exact, however, one can check the accuracy of this approximation using numerical simulations. The maximum error is small compared to the total density of apices as can be seen in Fig. 3.2.
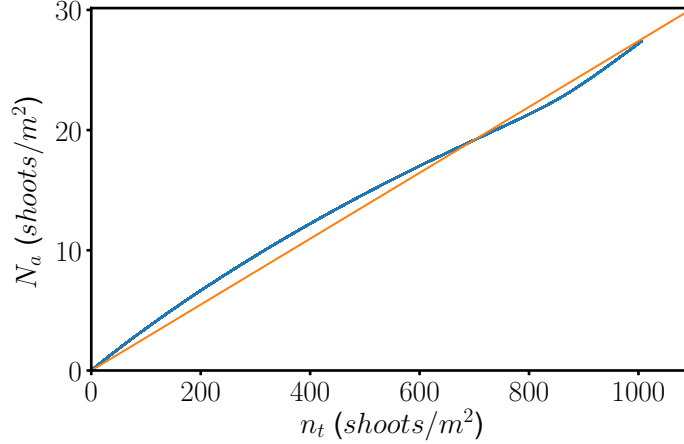
Figure 3.2: Deviations from the proportionality relation $N_a = \eta n_t$. In orange the exact relation is represented while in blue the values of shoots and apices density obtained for the numerical simulation shown in the right panel of Fig. 3.1.

This way, Eq. (3.2), (3.3) and (3.4) can be simplified as three two dimensional equations for n_t, a_1, b_1 that can be written as

$$\partial_t n_t = (\omega_b - \omega_d(n_t))n_t - \frac{\nu \pi}{\eta} \nabla \cdot \vec{a} \qquad (3.5)$$

$$\partial_t \vec{a} = (\omega_b \cos \phi_b - \omega_d(n_t))\vec{a} - \frac{\nu \eta}{2\pi} \vec{\nabla} n_t. \qquad (3.6)$$

Eq. (3.6) can be written in terms of the modulus $A = \|\vec{a}\|$ and the angle $\theta = \arctan(b_1/a_1)$

$$\partial_t A = (\omega_b \cos \phi_b - \omega_d(n_t))A - \frac{\nu \eta}{2\pi} \|\vec{\nabla} n_t\| \cos(\theta - \gamma), \qquad (3.7)$$

$$\partial_t \theta = \frac{\nu \eta}{2\pi} \frac{\|\vec{\nabla} n_t\|}{A} \sin(\theta - \gamma), \qquad (3.8)$$

where $\gamma = \arctan(\partial_y n_t / \partial_x n_t)$ is the angle that the gradient of the total density forms with the x-axis. Now it becomes clear from equation (3.8) that the evolution of the

system will drive the angle θ to the stable fixed point $\theta = \gamma + \pi$. This means that the gradient and the vector $\vec{a}$ have opposite directions, in other words they must be proportional, $\vec{a} = -C\vec{\nabla}n_t$ or $A = C\|\vec{\nabla}n_t\|$ where the constant C in principle can depend on n_t and its derivatives, as it can be seen from Eq. (3.7). Thus, if one introduces this result in the truncated Fourier series, the density of apices takes the following form:

$$n_a(\vec{r}, \phi, t) = \frac{N_a(\vec{r}, t)}{2\pi} + A(\vec{r}, t)\cos(\phi - \gamma(\vec{r}, t) - \pi). \tag{3.9}$$

Essentially the density of apices is driven mostly by the total density of apices plus small modulations that appear in the borders of the meadow. On the one hand, for regions where the density is homogeneous A is zero. Then densities of apices growing in different directions are equal. On the other hand regions where $\vec{\nabla}n_t \neq 0$ the modulation contributes and due to the cosine term, those apices growing outwards the meadow (normal to the front) have a maximum density while those growing inwards have a minimum as it can be seen in Fig. 3.1.

It is important to notice that starting with arbitrary distributions in the angle the system will spend a finite time to reach the configuration given by (3.9) and in this sense the approximation is only valid after this transient.

The value of C related with amplitude of the modulation A will in general be a function $C = C(n_t, \vec{\nabla}n_t, ...)$. This relation will be the result of the evolution of A with time given by Eq. (3.7). In general $C(n_t, \vec{\nabla}n_t, ...)$ can have a very complicated function, but we can consider the most simple expansion with explicit dependence of n_t.

$$\vec{a} = -(c_0 + c_1 n_t)\vec{\nabla}n_t. \tag{3.10}$$

Then introducing this expression in (3.5) one obtains a closed equation for the total density n_t.

$$\partial_t n_t = (\omega_b - \omega_d(n_t))n_t + \frac{\nu\pi}{\eta}(c_0\nabla^2 n_t + c_1 n_t\nabla^2 n_t + c_1\|\vec{\nabla}n_t\|^2). \tag{3.11}$$

We notice that parameters c_0 and c_1 are unknown, however, it is possible to determine its value in the limit in which Eq. (3.6) is equal to zero. This corresponds to assuming that the evolution of $\vec{a}$ has different timescale than the evolution of n_t, in such a way it reaches quickly its stationary state. Thus, substituting the approximation for $\vec{a}$ in this limit one can write

$$\left\{(\omega_b\cos\phi_b - \omega_d(n_t))(c_0 + c_1 n_t) - \frac{\nu\eta}{2\pi}\right\}\vec{\nabla}n_t = 0. \tag{3.12}$$

The easiest way to obtain the two parameters is using the previous equation substituting a moving front connecting the populated solution with the unpopulated

solution. The problem is that the front profile is not known a priori, however, what we do know is that the front connects the populated solution with the unpopulated solution. Thus, considering the one dimensional case for simplicity, at each side one can write the front solution as $n_t = n_t^* + \varepsilon e^{\lambda x}$ where λ is the spatial eigenvalue and $\partial_x n_t = \lambda \varepsilon e^{\lambda x}$, which leads to

$$
\left\{ (\omega_b \cos \phi_b - \omega_d(n_t^*)) \right.
$$
$$
\left. - (2bn_t^* + (\kappa e^{\frac{(\sigma_\kappa \lambda)^2}{2}} - \omega_{d0} e^{\frac{(\sigma_\mu \lambda)^2}{2}})e^{-an_t^*}a)\varepsilon e^{\lambda x})(c_0 + c_1 n_t^* + c_1 \varepsilon e^{\lambda x}) - \frac{\nu \eta}{2\pi} \right\} = 0.
$$
$$
(3.13)
$$

At the lowest order in ε

$$
(\omega_b \cos \phi_b - \omega_d(n_t^*))(c_0 + c_1 n_t^*) - \frac{\nu \eta}{2\pi} = 0, \tag{3.14}
$$

which is essentially Eq. (3.12) evaluated at the fixed point n_t^*. Finally, if one substitutes the unpopulated solution $n_t^* = 0$ one can find c_0 and using the populated solution n_t^* one obtains:

$$
c_0 = \frac{\nu \eta}{2\pi(\omega_{d0} - \omega_b \cos \phi_b)} \tag{3.15}
$$

and

$$
c_1 = \frac{\nu \eta}{2\pi n_t^*} \left(\frac{1}{\omega_b \cos \phi_b - \omega_{d0}} - \frac{1}{\omega_b \cos \phi_b - \omega_b} \right). \tag{3.16}
$$

The factor η/π disappears when introducing the coefficients in Eq. (3.11), so we can rewrite it as follows:

$$
\partial_t n_t = (\omega_b - \omega_d(n_t))n_t + d_0 \nabla^2 n_t + d_1 n_t \nabla^2 n_t + d_1 \|\vec{\nabla} n_t\|^2, \tag{3.17}
$$

$$
d_0 = \frac{\nu^2}{2(\omega_{d0} - \omega_b \cos \phi_b)} \tag{3.18}
$$

and

$$
d_1 = \frac{\nu^2}{2n_t^*} \left(\frac{1}{\omega_b \cos \phi_b - \omega_{d0}} - \frac{1}{\omega_b \cos \phi_b - \omega_b} \right). \tag{3.19}
$$

d_1 depends on parameters through n_t^* which is the solution of (2.9). In particular, it is not surprising the approximation is more accurate at the Maxwell point, where the front is stationary. In the following we are going to test the validity of the approximations. We are going to consider two approaches. First, we consider the

values of d_0 and d_1 vary with the other parameters. And second, we are going to consider both constant using the value at the Maxwell point $d_{0,m}$ and $d_{1,m}$. For the second approach the Maxwell point is calculated using numerical simulations as illustrated in Fig. 3.3. In particular we set $\sigma_\kappa = \sigma_\mu = 0$ to avoid the formation of patterns and simplify the calculation, while other parameters are the same as in chapter 2. Essentially, doing that, we compute $d_{0,m}$ and $d_{1,m}$ as the result of clonal growth only, which is reasonable since other interaction mechanisms have not been calibrated using experimental measures. Using the adimensional units defined in the appendix A where ω_b, ν, $b = 1$, the mortality at the Maxwell point is $\omega_{d0,m} = 1.3194$ and $n_{t,m}^* = 0.3855$, as a result $d_{0,m} = 0.8166$ and $d_{1,m} = 2.3101$ (or in more intuitive units $d_{0,m} = 508.1\ cm^2 year^{-1}$ and $d_{1,m} = 6560.6\ cm^4 year^{-1}$).

In order to give a quantitative description, the model must reproduce different important aspects. It is important to have the same velocity and smoothness of the front representing the advance or recession of a meadow. Using the parameters d_0 and d_1 derived, these two features are well reproduced as can be seen in Fig. 3.3. We use numerical simulations of a homogeneous front in the ABD model and the simplified equation (3.17). We set $\sigma_\kappa = \sigma_\mu = 0$ to prevent the formation of patterns and we compute the velocity of the homogeneous front for different values of the mortality. As one can see the constant value of $d_{0,m}$ and $d_{1,m}$ reproduce better the velocity of the front for different values of mortality. We notice the other approach fails outside the bistable region mainly because both parameters diverge close to $\omega_{d0} = \omega_b \cos \phi_b$.

Another important aspect for reproducing the quantitative behavior of the system is the preservation of the position of the MI in the phase diagram, in other words for which parameters the homogeneous meadow becomes unstable to patterns. As a result of the linear stability analysis of the complete model and the approximated equation given by (3.17), represented in Fig. 3.4 the MI matches almost exactly considering the full dependence with parameters of d_0 and d_1, having small discrepancies for large competition strength κ, which does not correspond with typical values used for *P. oceanica*. We perform the linear stability of Eq. (3.17) in chapter 4 in more detail, however, we notice the linearization in Fourier of the new terms leads to $-(d_0 + d_1 n^*)q^2$, with $(d_0 + d_1 n^*) = \nu^2/(2\omega_b(1 - \cos \phi_b))$. On the contrary when d_0 and d_1 are considered constant $(d_0 + d_1 n^*)$ depends on the value of n_t^* and the linear stability analysis has bigger discrepancies with the original one specially for large κ.

Summarizing, none of the two approaches produces the best results in all cases, however, for $\kappa < \omega_b$ which is the case, which we are interested in, considering constant the values of $d_0 = d_{0,m}$ and $d_1 = d_{1,m}$ the calculations are much more simpler and the divergence is avoided. In the following we are going to use this approach instead of the full dependence of d_0 and d_1.
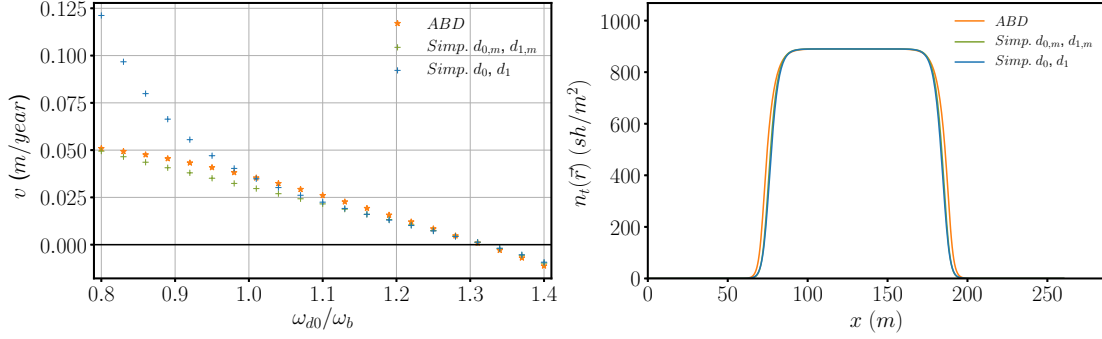
Figure 3.3: Left: Front velocity of the populated solution invading the unpopulated one as a function of the ratio between mortality and branching rates for the ABD model and the simplified version. the results with constant d_0 and d_1 are shown in green, and considering them parameter dependent in blue. Right: Density profile of the density of shoots n_t for the ABD model and the simplified for $\omega_{d0} = 0.072 \ year^{-1}$, green and blue equivalently to left panel. The parameters used are $\omega_b = 0.06 \ year^{-1}$, $\nu = 6.11 \ cm/year$, $\rho = 2.87 \ cm$, $\phi_b = 45°$, $b = 1.25 \ cm^4 year^{-1}$, $\kappa = 0.048 \ year^{-1}$, $\sigma_\kappa = 0 \ cm$, $a = 27.38 \ cm^2$, $\sigma_\mu = 0 \ cm$, $\mu = \omega_{d0}$ and for the simplified model $d_0 = 508.1 \ cm^2 year^{-1}$ and $d_1 = 6560.6 \ cm^4 year^{-1}$.

Focusing on the different terms present in the resultant equation for the total density one can identify the contribution of the different mechanisms to each term. First, it is clear that mortality appears in all terms. Branching instead has become a birth term independent of the growth direction of course. More interesting are the terms coming from the advection of apices in combination with branching and nonlinearity. Three terms appear in the derivation: a diffusion term, a nonlinear diffusion and a modulus square of the gradient, where the last two have the same coefficient determining its intensity. These three terms are the result of apices growing in all directions giving a contribution beyond diffusion and nonlinear diffusion, which are terms present in other vegetation models of pattern formation [115, 15, 41]. Thus, this new description of clonal growth accounts for the usual terms but it predicts a new contribution, $d_1 \|\vec{\nabla} n_t\|^2$, distinctive of clonal growth which is very interesting from the theoretical point of view. It has been shown that this term can displace the Maxwell point favoring the advance of the populated solution [116], which is compatible with the interpretation of this term as a spreading term.

At this stage we have simplified the complete 3-dimensional model with two equations to one equation in 2 dimensions. This description provides accurate quantitative results providing a simpler description for the modelizations of *P. oceanica*. In principle, other species of clonal plants can be well described with this approach although
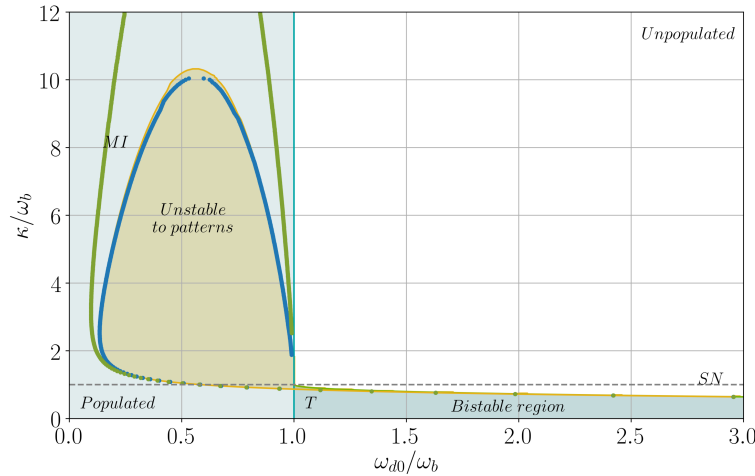
Figure 3.4: Comparison of phase diagram of the complete model and the simplified equation (3.17). In green $d_0 = d_{0,m}$ and $d_1 = d_{1,m}$ are considered constant, and in blue the dependence of d_0 and d_1 with parameters is considered. The parameters are $\omega_b = 0.06$ $year^{-1}$, $\nu = 6.11$ $cm/year$, $\rho = 2.87$ cm, $\phi_b = 45°$, $b = 1.25$ $cm^4 year^{-1}$, $\sigma_\kappa = 2851.4$ cm, $a = 27.38$ cm^2, $\sigma_\mu = 203.7$ cm. We show the region where the populated solution is stable in bright blue, where the unpopulated solution is stable in white, the region of coexistence between the populated and unpopulated in blue, and finally the region where the populated solutions is unstable to patterns in yellow. T refers to the transcritical bifurcation at $\omega_{d0}/\omega_b = 1$, and SN for the saddle-node bifurcation where the subcritical populated solutions ends. Green and blue dots correspond to the modulation instability curve of the simplified equation in each case.

the validity of all approximations remains to be investigated. The simplified model in equation (3.17) approximates quantitatively good the ABD model. In chapter 4 we devote more effort to study the results with the simplified model preserving the interaction terms described by the kernel. Now we analyze further the derivation of the simple model. In [117] a more simple description based on symmetry arguments for the growth of clonal plants is proposed. Here we can derive this equation giving a relation between parameters performing a moment expansion of the kernel. The disadvantage of the next steps in the derivation is that the quantitative agreement is lost. In particular, the spatial scale of the pattern, the density of shoots for the homogeneous solution or the position of the MI are not well reproduced. The advantage is that one can tune the parameters for each particular case and use it to realize numerical simulations and more important to understand the qualitative behavior of the growth.

3.1.2 Moment expansion of the kernel

In order to reach the simplest description we approximate the nonlocal interactions in $\omega_d(n_t)$ as follows. First of all, the exponential term can be expanded at first order such that $(1-e^{-a_e n_t}) \sim a_e n_t$ then extracting a_e out of the integral, the nonlocal term reads:

$$I(n_t(\vec{r},t)) = \int\limits_{-\infty}^{\infty} \int\limits_{-\infty}^{\infty} \mathcal{K}(\vec{r}-\vec{r}')n_t(\vec{r}',t)d\vec{r}'. \tag{3.20}$$

The integral term can be expanded using a moment expansion as in [118, 105, 106] which is equivalent to a Taylor expansion of the kernel in the Fourier space. The moment expansion allows to write the integral in terms of the derivatives in space where only even derivatives contribute given the symmetry of the kernel $\mathcal{K}(\vec{r}) = \mathcal{K}(-\vec{r})$:

$$I(n_t(\vec{r},t)) = \sum_{j=0}^{\infty} \frac{M_{2j}}{(2j)!}\nabla^{2j}n_t(\vec{r},t), \tag{3.21}$$

where the coefficients correspond to the moments of the kernel.

$$M_{2j} = (-1)^j \frac{d^{(2j)}\tilde{\mathcal{K}}(q)}{dq^{2j}}\bigg|_{q=0} = 2\pi(-1)^j J_0^{(2j)}(0)\int_0^{\infty} r^{2j+1}\mathcal{K}(r)dr. \tag{3.22}$$

Considering terms until fourth order provides the simplest description of the integral leading to patterns. Although the critical wave number is not well captured the qualitative behavior is well reproduced. Hence, replacing the integral term by the expansion until fourth order in Eq. (3.17) one can write the following equation describing the evolution of the total density.

$$\begin{aligned}
\partial_t n_t &= (\omega_b - \omega_{d0})n_t - a_e(\kappa-\mu)n_t^2 - bn_t^3 \\
&+ (d_1 - \frac{a_e(\kappa\sigma_\kappa^2 - \mu\sigma_\mu^2)}{2})n_t\nabla^2 n_t - \frac{a_e(\kappa\sigma_\kappa^4 - \mu\sigma_\mu^4)}{8}n_t\nabla^4 n_t \\
&+ d_0\nabla^2 n_t + d_1\|\nabla n_t\|^2.
\end{aligned} \tag{3.23}$$

At this level the approximation is too rough to provide a quantitative correspondence. Essentially the approximation of the exponential removes the saturation of the interaction with n_t and leads to values of the stationary density which are very different from the original model. In addition, the moment expansion does not have enough terms to reproduce the shape of the kernel for large wavenumbers. In Fig. 3.5 we show the moment expansion in Fourier space with different orders of the expansion to clearly show that fourth order is not sufficient.
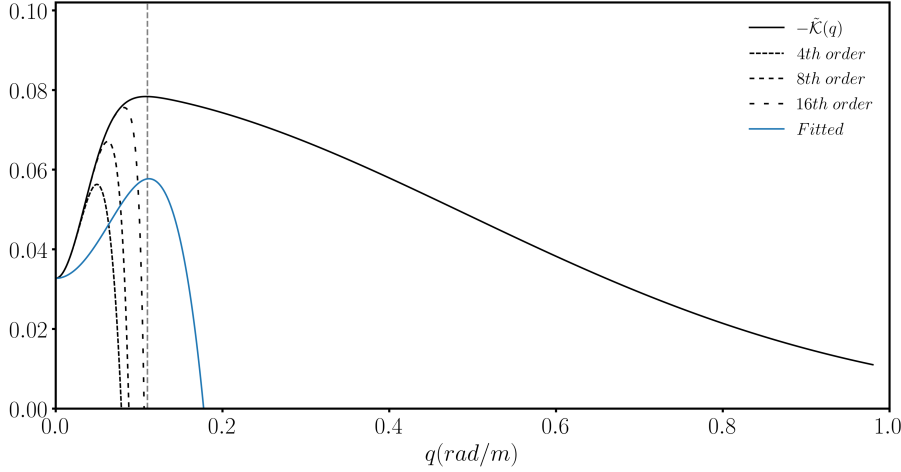
Figure 3.5: Representation of the kernel in Fourier space together with different moment expansions truncated at different orders as well as a fourth order polynomial in blue chosen to have the maximum at the same wave number than the kernel. Parameters are $\omega_{d0} = 0.08$ $year^{-1}$, $\kappa = 0.048$ $year^{-1}$, $\sigma_\kappa = 2851.4$ cm, $\sigma_\mu = 203.7$ cm.

3.2 Analysis of the simplified equation

Hence, the alternative approach is to recalibrate the model to resemble quantitatively the complete model. In the following for simplicity in the notation, $n \equiv n_t$

$$\partial_t n = (\omega_b - \omega_{d0})n + a(\kappa - \omega_b)n^2 - bn^3 - \alpha n\nabla^2 n - \beta n\nabla^4 n + d_0\nabla^2 n + d_1\|\nabla n\|^2, \quad (3.24)$$

where now a, b, α and β are chosen to satisfy some constraints. The first one has been already introduced. In order to have the saddle node bifurcation and the transicritical bifurcation intersecting at $\kappa = \omega_b$, as in the ABD model, we need to impose $\mu = \omega_b$. This can be done without loss of generality and it facilitates the comparison between the ABD model and its most simplified version. We choose $a = 100.41$ $cm^2 year^{-1}$ and $b = 12.5$ $cm^4 year^{-1}$ imposing that for $\kappa = 0.048$ $year^{-1}$ the mortality of the saddle node is close to $\omega_{d0}/\omega_b = 1.5$, which corresponds to the value in the original model. The values of the shoot density are similar too. In other words we choose both parameters to have a similar bifurcation diagram, as can be seen in Fig. 3.8. The parameters $\alpha = 8.642 \cdot 10^7$ $cm^6 year^{-1}$ and $\beta = 3.585 \cdot 10^{13}$ $cm^8 year^{-1}$ are chosen for $\kappa = 0.048$ $year^{-1}$ in order to have a the modulation instability at the same value of mortality and with the same critical wavenumber than the ABD model. This can be easily done because in this model the dispersion relation has an analytical expression which can be obtained considering perturbations of the type $n = n^* + e^{\lambda t + iqx}$, and it is given by:

$$\lambda(q) = \omega_b - \omega_{d0} + 2a(\kappa - \omega_b)n^* - 3bn^{*2} + \alpha n^* q^2 - \beta n^* q^4 - d_0 q^2, \qquad (3.25)$$

where $q = \|\vec{q}\|$ is the wavenumber of the perturbation and n^* the stationary solution which can be zero for the stability of the unpopulated solution and

$$n_{\pm}^* = \frac{a(\kappa - \omega_b)}{2b} \pm \sqrt{\left(\frac{a(\kappa - \omega_b)}{2b}\right)^2 - \frac{\omega_b - \omega_{d0}}{b}}, \qquad (3.26)$$

for the populated solution. Thus, the critical wavenumber is given by $q_c = \sqrt{\frac{\alpha n_+^* - d_0}{2\beta n_+^*}}$, while there is not an analytical expression for the threshold.
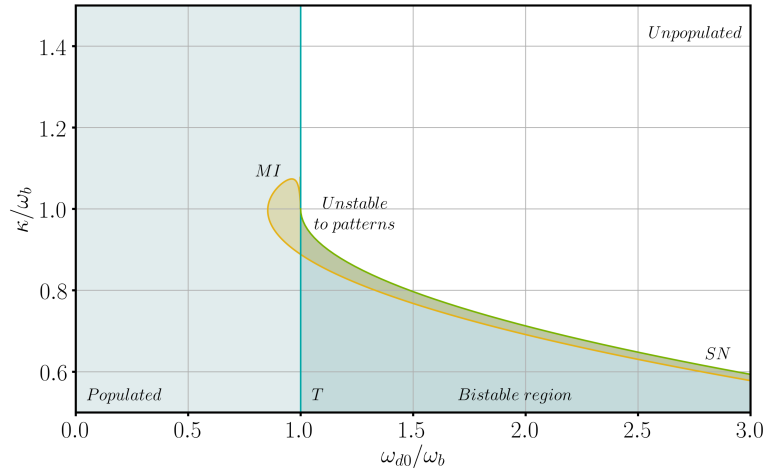
Figure 3.6: Phase diagram of the simplified model in (3.24). The parameters are $\omega_b = 0.06$ $year^{-1}$, $a = 100.41$ $cm^2 year^{-1}$, $b = 12.5$ $cm^4 year^{-1}$, $\alpha = 8.642 \cdot 10^7$ $cm^6 year^{-1}$, $\beta = 3.585 \cdot 10^{13}$ $cm^8 year^{-1}$, $d_0 = 508.1$ $cm^2 year^{-1}$ and $d_1 = 6560.6$ $cm^4 year^{-1}$. We show the region where the populated solution is stable in bright blue, where the unpopulated solution is stable in white, the region of coexiestence between the populated and unpopulated in blue, and finally the region where the populated solutions is unstable to patterns in yellow. T refers to the transcritical bifurcation at $\omega_{d0}/\omega_b = 1$, and SN for the saddle-node bifurcation where the subcritical populated solutions ends.

In Fig. 3.6 we show the phase diagram computed with 3.25. Structurally the phase diagram is equivalent to the one of the full model (Fig. 3.4), in the sense that the same phases can be found. Similarly, the modulation instability reproaches to the saddle node bifurcation when decreasing the strength of competition in the subcritical case. On the contrary, in the supercritical case, when $\kappa > \omega_b$ there is again a window between two modulation instabilities where the solution is unstable
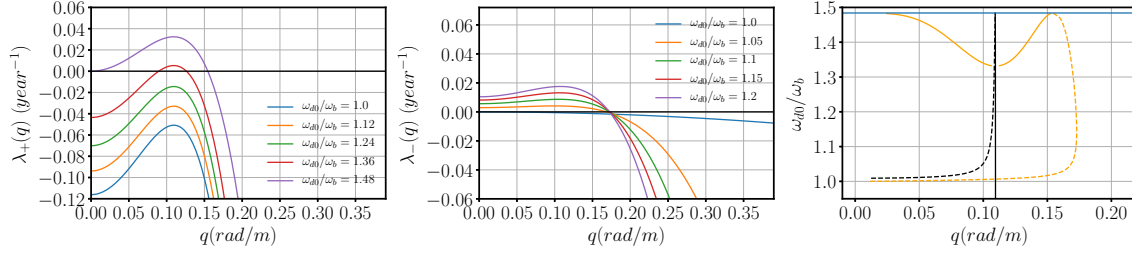
Figure 3.7: Dispersion relation for the populated solution n_+ (left) and n_- (center) for different values of the mortality. Right: Marginal stability curve for n_+ in yellow and n_- in dashed yellow. In black the maximum of the dispersion relation is representes respectively. The parameter set are $\omega_b = 0.06\ year^{-1}$, $\kappa = 0.048\ year^{-1}$, $a = 100.41\ cm^2 year^{-1}$, $b = 12.5\ cm^4 year^{-1}$, $\alpha = 8.642 \cdot 10^7\ cm^6 year^{-1}$, $\beta = 3.585 \cdot 10^{13}\ cm^8 year^{-1}$, $d_0 = 508.1\ cm^2 year^{-1}$ and $d_1 = 6560.6\ cm^4 year^{-1}$.

to patterns. Essentially the qualitative features of the model have not been modified, however, the results are quantitatively different. Fig. 3.7 shows the finite wavelength instability of the populated solution for different values of the mortality in the supercritical regime. Additionally, we show the dispersion relation for the unstable branch which is unstable for $q = 0$ for all values of the parameters. However, for a certain value of the density n_-^* close to the transcritical bifurcation the maximum of the dispersion relation changes to a finite wavelength. Finally, we show the marginal stability curve for the two branches together with the maximum of the dispersion relation.

As a result of the modulation instability a pattern forms, here we study the bifurcation diagram of patterns and localized states using numerical continuation techniques (see Appendix D, thus we can find stationary solutions, including the unstable parts which are not available using numerical simulations. In Fig. 3.8 we show the results in one dimension. The stripes solution with the critical wavenumber emerges from the Modulation Instability (MI) subcritically and folds for lower values of mortality. The branch stabilizes at the fold. Thus, increasing mortality the branch continues after the saddle node of the homogeneous solutions folding again at another saddle node, where the stability changes and continues decreasing mortality until it connects with the solution n_- very close to zero density where the critical mode bifurcates. Thus, the stable pattern extends for larger values of the mortality coexisting with the unpopulated solution. This solution persist beyond mortality values where the homogeneous solution does not exist. When the stripes solution is subcritical and coexists with the homogeneous solution the so called homoclinic snaking region appears [111, 112, 114]. In this region there are localized solutions, which from the perspective of spatial dynamics are connections of the periodic orbit formed by the pattern with the homogeneous solution. These are homoclinic
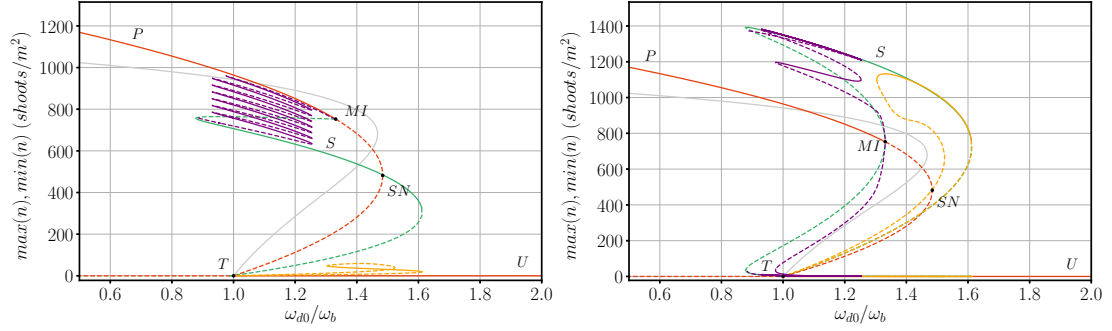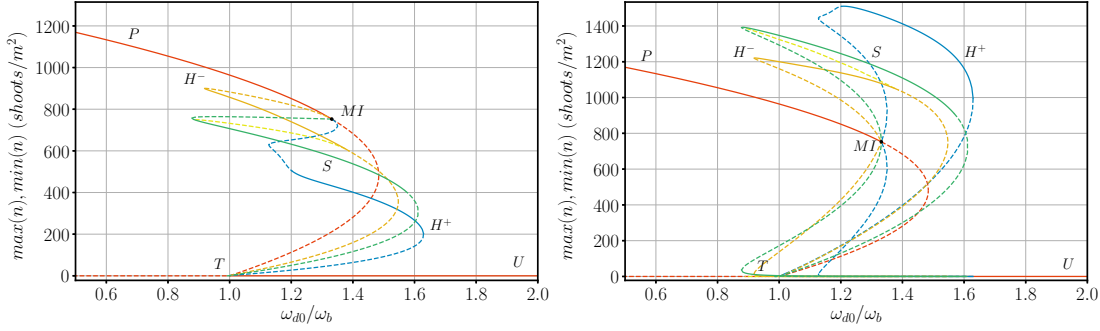
Figure 3.8: Bifurcation diagram of the simplified equation in one dimension. Left panel shows the average density for different solutions while right panel shows the maximum and minimum of the density. In red the homogeneous populated solution $n_\pm$ (P) and the unpopulated (U). In purple isolated holes, stripes (S) in green and localized spots in orange. Continuous (dashed) line indicates the sable (unstable) solutions. MI refers to the modulation instability, T to the transcritical, and SN to the saddle node. In gray the homogeneous solution of the ABD model for comparison. The parameter set are $\omega_b = 0.06$ $year^{-1}$, $\kappa = 0.048$ $year^{-1}$, $a = 100.41$ cm^2year^{-1}, $b = 12.5$ cm^4year^{-1}, $\alpha = 8.642 \cdot 10^7$ cm^6year^{-1}, $\beta = 3.585 \cdot 10^{13}$ cm^8year^{-1}, $d_0 = 508.1$ cm^2year^{-1} and $d_1 = 6560.6$ cm^4year^{-1}.

connections where interpreting space as the analog of time the solution starts from the homogeneous solution does a cycle around the periodic orbit and returns to the homogeneous solution. This solution in particular corresponds to a hole without vegetation embedded in a dense meadow or a fairy circle. Equivalently two oscillations are also a solution which corresponds to two holes. In fact an arbitrary number of them is possible in this region. The bifurcation diagram shows all these solutions. The branch bifurcates from the modulation instability subcritically, after the first fold the localized structure with one hole stabilizes. The curve snakes and after every two folds an additional hole is created at each side until all the domain is filled and the branch connects with the periodic orbit or a stripes pattern. For larger values of mortality, and as the last state before desertification, a different set of localized structures exist. Localized patches, emerge from the solution n_- at a distance from the transcritical determined by the system size. A single peak grows from a modulation with a wavelength equal to the system size when increasing mortality. After a fold, where stabilizes, continues decreasing mortality until a second fold where the solution splits in two peaks and becomes unstable, which later decrease in size following the curve and reaching again to the solution n_-. In chapter 4 we devote more efforts to analyze localized structures and their bifurcation diagram in the model with the kernel in 3.17 which are very similar to the ones presented here.

In Fig. 3.9 we present the bifurcation diagram including positive hexagons (spots), stripes and negative hexagons (gaps) in order to show, in fact, that the sim-

Figure 3.9: Bifurcation diagram of the simplified equation in two dimensions. Left panel shows the average density for different solutions while right panel shows the maximum and minimum of the density. In red the homogeneous populated solution $n_\pm$ (P) and the unpopulated (U). In yellow negative hexagons (H^-), in bright yellow mixed mode connecting stripes and negative hexagons, in green stripes (S) computed in one dimension and finally in blue positive hexagons (H^+). Continuous (dashed) line indicates the sable (unstable) solutions. MI refers to the modulation instability, T to the transcritical, and SN to the saddle node. The parameter set are $\omega_b = 0.06 \ year^{-1}$, $\kappa = 0.048 \ year^{-1}$, $a = 100.41 \ cm^2 year^{-1}$, $b = 12.5 \ cm^4 year^{-1}$, $\alpha = 8.642 \cdot 10^7 \ cm^6 year^{-1}$, $\beta = 3.585 \cdot 10^{13}$ $cm^8 year^{-1}$, $d_0 = 508.1 \ cm^2 year^{-1}$ and $d_1 = 6560.6 \ cm^4 year^{-1}$.

plified model presents the same patterns than the ABD model. Negative hexagons bifurcate subcritically and fold at a saddle node where they acquire stability. In the middle of the branch a mixed mode bifurcates connecting with the solution of stripes and precisely at this value the solution loses stability. The branch finishes close to the transcritical bifurcation after the fold as previously. Positive hexagons perform a similar path reaching higher values of the mortality. This branch bifurcates supercritically in agreement with the general theory of pattern formation. However, the unstable branch folds twice before stabilizing and remains stable until the last fold. Interestingly, the bifurcation diagram shows that positive hexagons are the most persistent solution for high values of mortalities. Note that stripes are unstable to hexagons close to their fold. In general the three solution change similarly when increasing mortality, the parts without vegetation increase in such a way the average density decreases for larger mortality, which is consistent with the ABD model and the fact of approaching desertification. Notice the standard sequence of patterns, negative hexagons, stripes, positive hexagons when increasing mortality appears. Moreover, different ranges of stability of the stationary solutions are present, which in certain cases coexist. In fact, it is possible to find values of the mortality in which all the solutions are stable simultaneously, including the homogeneous, hence, it is expected to find a very rich spatiotemporal dynamics due to these ranges of coexistence.

3.3   Conclusions

We have derived a simplified 2-dimensional equation describing the total density in space from the complete ABD model consisting of one 2-dimensional and one 3-dimensional equations describing shoots and apices. This derivation makes a connection between the terms appearing in the simplified equation with the mechanisms of clonal growth involved in the ABD. Consequently we have given a relation between parameters of both models allowing to realize numerical simulations with the simplified equation corresponding to real conditions. It is important to notice that the new equation has a new term no present before in previous models. The term $d_1 \|\nabla n\|^2$ is new, and it is a specific feature of clonal growth. This term adds an extra contribution to the spatial spreading, increasing the velocity of the front. Thus, the exploration of the additional effects this term can introduce in the growth will have an important impact on the understanding of clonal growth from the spatial colonization perspective.

The approximations made are well justified and in accordance with numerical simulations. Moreover, we have shown that the simplified equation reproduces the velocity and profile of the front in the subcritical region providing a good quantitative description of the colonization of space due to clonal-growth rules. The phase diagram and the position of the MI is maintained as well, when considering constant d_0 and d_1 the curve can change with respect to the ABD model, however, it not changes is qualitative shape. Even so, the approximation remains valid specially in the subcritical domain. Furthermore, we show that when approximating the kernel term by a Taylor expansion the qualitative behavior is reproduced but the quantitative agreement is lost. For instance, we have shown the equivalence of the phase diagram and MI, the presence of the same patterns and its sequence of appearance with mortality. Localized structures are also present as the analog of fairy circles. Isolated patches have been found too.

Clonal-growth plants are present in many different ecosystems where the conditions of growth can also change. From this perspective not all the approximations will hold for different species. However, the fact that one has a procedure to simplify the complete model of clonal growth allows to choose different levels of approximation according to the conditions we want to reproduce. A good example of this is the moment expansion of kernel.

The approximation using the moments of the kernel is equivalent to a Taylor expansion of the kernel in Fourier space. This way it is very easy to test the accuracy of the approximation. For the particular case of *P.oceanica* the competition length is large and as a result when one considers the moment expansion until fourth order the maximum of the kernel in Fourier space is not well captured, which will give a

wrong critical wave number or patterns with different characteristic wavelength than the original model. The immediate solution of considering more terms of the expansion, or expanding around the maximum of the dispersion relation, do not provide a more simple description. The disadvantages of this approximation can be avoided in two ways. The first option is to consider the complete kernel which we are going to develop in chapter 4, and it gives very good results compared to the complete model in terms of numerical efficiency. The other possibility, if one wants to use the most simplified equation, is changing the parameters to fit the bifurcation diagram the mortality of the modulation instability and the wavenumber of the ABD model.

Other species instead will have interaction across space which will be well reproduced with the kernel moment expansion, however, it may be possible to have a different branching angle which will make some of the previous approximation less appropriate. Given the generality of the model, it would be useful to learn from the derivation which approximations are good for each particular species which is something to be investigated in the future.

Simplified model with long-range interactions

The previous chapter focuses on the derivation of a simplified equation from the ABD model. As a result of different approximations the quantitative agreement is lost and parameters need to be fitted in order to obtain reasonable results from the quantitative point of view. There is an intermediate point in the derivation in which the quantitative agreement holds. In particular Eq. (3.17). Changing for simplicity the notation to $n \equiv n_t$ it reads

$$\partial_t n = (\omega_b - \omega_d(n))n + d_0 \nabla^2 n + d_1 n \nabla^2 n + d_1 \|\nabla n\|^2, \tag{4.1}$$

where the mortality term accounts for the nonlocal interactions described by the integral term

$$\omega_d(n) = \omega_{d0} + \int\int \mathcal{K}(\vec{r} - \vec{r'})(1 - e^{-an(\vec{r'})})d\vec{r'} + bn^2. \tag{4.2}$$

Keeping the full nonlocal term Eq. (4.2) preserves all the features of the full model. Thus, there are two important reasons to study this intermediate equation. First, it is a better approximation to the ABD model. Second, the influence of the nonlocal interaction in the dynamics and the spatial profiles have been less studied. Most studies use equations representing spatial coupling with derivatives up to fourth order. Thus, the interaction represented with the integral term gives an additional interest to the problem. The aim is to provide a deeper characterization of the model, in particular the stationary states, their stability and their coexistence.

This chapter is organized as follows: The first section focuses on the linear stability analysis of the model. The second section on the bifurcation diagram in one and two dimensions. Finally, the last section focuses on the dynamics of fronts between two stationary states in the one dimensional case.

4.1 Linear stability analysis

The homogeneous stationary solution n^* of Eq. (4.1) is given by (2.9). It is the same stationary solution of the ABD model for the total density. Both the populated and zero states are solutions of this equation. The stability of these stationary states is determined with a linear stability analysis. One considers the evolution of small perturbations around the stationary states of the form $n = n^* + e^{\lambda t + i\vec{q}\cdot\vec{r}}$ to obtain the dispersion relation $\lambda(\vec{q})$. For the unpopulated case it reads

$$\lambda(q) = \omega_b - \omega_{d0} - d_0 q^2, \tag{4.3}$$

where $q = \|\vec{q}\|$. Essentially there is a change of stability at $q = 0$ for $\omega_b = \omega_{d0}$ where the homogeneous solution bifurcates. Above this transcritical bifurcation the unpopulated state is stable and perturbations decay, below the threshold perturbations grow until the saturation term limits the growth and the systems reach the stationary populated state.
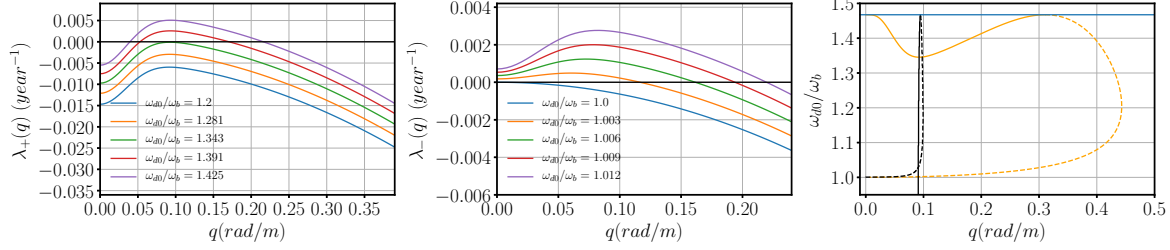Around the populated solution the dispersion relation has the following form

$$\lambda(q) = -(2bn^* + ae^{-an^*}\tilde{\mathcal{K}}(q))n^* - (d_0 + d_1 n^*)q^2, \tag{4.4}$$

where $\tilde{\mathcal{K}}(q)$ is the Fourier transform of the kernel. In analogy to the previous chapter we call n_+ the part of the populated solution which is stable for $q = 0$ and n_- the part that is unstable, these two branches emerge from a saddle node bifurcation. Thus, one can study the stability of the two branches independently as it can be seen in Fig. 4.1. For n_+ the maximum of the dispersion relation becomes positive at $\omega_{d0,c}/\omega_b = 1.345$ with the critical wavenumber $q_c = 0.094\ rad/m$. Although nonlinearities can play an important role, the maximum of the dispersion relation generally determines the wavenumber of the emerging pattern. The solution n_-, close to the transcritical has a parabolic dispersion relation with maximum at $q = 0$. However, when moving along n_- increasing ω_{d0}, the maximum displaces to finite wavenumbers. The marginal stability curve summarizes the dependence of the two solutions with ω_{d0}. After the onset of the modulation instability at $\omega_{d0,c}$ a bandwidth of finite wavenumbers becomes unstable, which reaches to zero at the saddle node. Following the branch decreasing n_-, now the homogeneous mode is unstable and the band widens. Finally close to zero density the bandwidth diminishes and the maximum of $\lambda(q)$ moves to $q = 0$, or to very large wavelengths.

It is not possible to obtain an exact expression of the critical wave number q_c, however, in the limit $\sigma_\mu \to 0$ one can obtain the following expression for the wavenumber with maximum growth rate as a function of the stationary density n^*

$$q_m^2 = \frac{2}{\sigma_\kappa^2} \ln\left(\frac{\kappa\sigma_\kappa^2 ae^{-an^*}n^*}{2(d_0 + d_1 n^*)}\right) \tag{4.5}$$

Figure 4.1: Dispersion relation for the populated solution n_+ (left) and n_- (center) for different values of the mortality. Right: Marginal stability curve for n_+ in yellow and n_- in dashed yellow. In black the maximum of the dispersion relation is represented. Finally the value of ω_{d0}/ω_b of the saddle node bifurcation is indicated with a blue line. The parameters are $\omega_b = 0.06\ year^{-1}$, $\kappa = 0.048\ year^{-1}$, $a = 27.38\ cm^2$, $b = 1.25\ cm^4 year^{-1}$, $\sigma_\kappa = 2851.4\ cm$, $\sigma_\mu = 203.7\ cm$, $d_0 = 631.2\ cm^2 year^{-1}$, $d_1 = 4842.1\ cm^4 year^{-1}$.

which is a good approximation since σ_μ is small compared with σ_κ.

The phase diagram in Fig. 4.2 using adimensional mortality ω_{d0}/ω_b and adimensional strength of the interaction κ/ω_b, shows essentially the same as in Fig. 3.4.
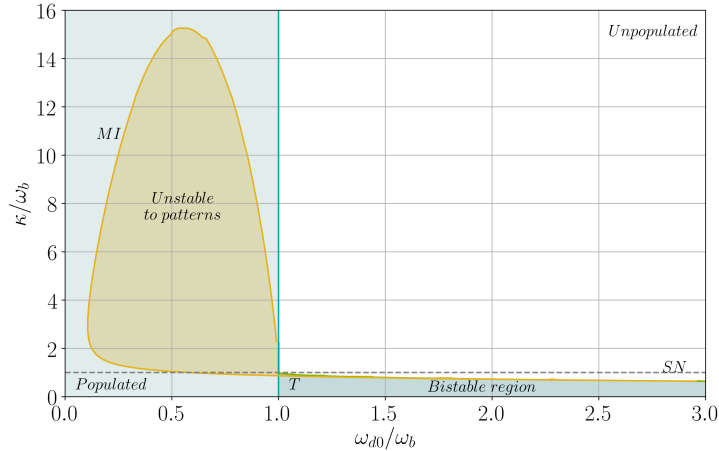
Figure 4.2: Phase diagram of Eq. (4.1). Here $\omega_b = 0.06\ year^{-1}$, $b = 1.25\ cm^4 year^{-1}$, $\sigma_\kappa = 2851.4\ cm$, $a = 27.38\ cm^2$, $\sigma_\mu = 203.7\ cm$, $d_0 = 631.2\ cm^2 year^{-1}$, $d_1 = 4842.1\ cm^4 year^{-1}$. We represent the region where the populated solution is stable in bright blue, where the unpopulated solution is stable in white, the region where populated and unpopulated coexist in blue, and finally the region where the populated solution is unstable to patterns in yellow. Note that the patterns arising from the MI extend beyond this region and may coexist with the populated or unpopulated solutions. T stands for the transcritical bifurcation at $\omega_{d0}/\omega_b = 1$, and SN for the saddle-node bifurcation where the subcritical populated solutions ends.

For small values of κ/ω_b, in the bistable regime, the region stable to patterns extend until the saddle node. On the contrary, for larger values of κ/ω_b there is a limited window between two modulation instabilities. The modulation instability extends for larger values of κ/ω_b due to the constant values of d_0 and d_1, being this the only difference with previous cases.

4.2   Continuation of nonlinear states

The pattern that forms after the onset of the instability emerges as a result of long-range competition and nonlinearity. As shown previously, different patterns emerge from the modulation instability according to the theory of pattern formation, and nonlinearity plays an important role in the relative stability of different stationary solutions. Using continuation techniques it is possible to track these nonlinear states in parameter space.

We focus first on the one dimensional case. The pattern with critical wavenumber bifurcates at the modulation instability subcritically. The solution which emerges as an harmonic function is unstable. Decreasing mortality the nonlinearities become important and modifies the pattern profile to a non-harmonic function. After the saddle node the pattern stabilizes, the spatial profile here is characterized by maximum density at the borders of the meadow (Fig. 4.4). At difference with the simplified Eq. (3.24) where the profiles are quasi-harmonic, here the integral term couples a broader region of space, in such a way plants at the border can benefit from the lack of density in the vicinity. The stripe pattern persists until large values of the mortality. Increasing mortality the pattern changes in a continuous way decreasing the value of the average density, as can be seen in Fig. 4.3 and 4.4. The regions with non-zero density shrink and the maximum density grows, leading to a more compact distributions of vegetation in harmful growth conditions.

In the region of bistability between the pattern and the homogeneous solution localized structures form. In this interval there is a subdomain in which an arbitrary number of localized holes embedded in the homogeneous solution is stable. In Fig. 4.5 we show the bifurcation structure of these stationary states. At the modulation instability two branches bifurcate subcritically, which fold for a lower value of the mortality forming respectively a localized structure with one and two holes. Both solutions have oscillatory tails, the first oscillation moderately increases its amplitude as one follows the curve. At the fold this oscillation starts to increase considerably and at the next fold two extra holes have been created at both sides of the first localized structure. This process is successively repeated for next folds until the full domain is filled and the branches connect with a branch of stripes with the wavelength selected the front between the pattern and the homogeneous solution. The parts
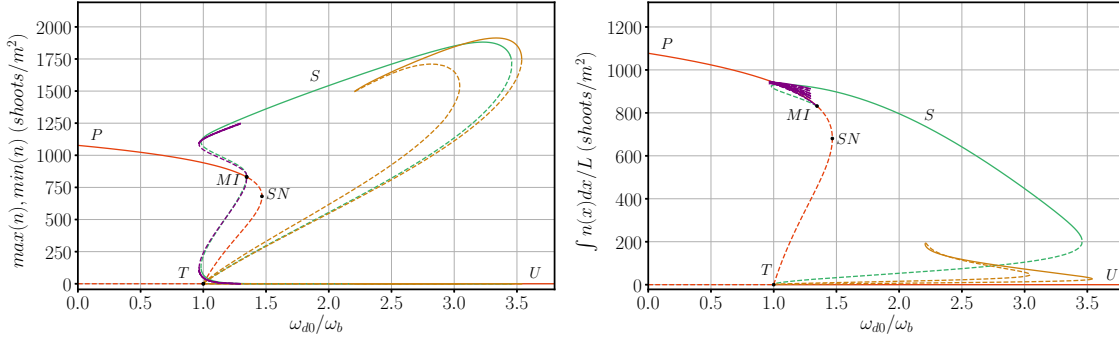
Figure 4.3: Bifurcation diagram as a function of the ratio ω_{d0}/ω_b. The maximum and minimum value of the density for different stationary solutions is plotted in the left panel and the integral of the solution divided by the system size in the right panel. Continuous (dashed) lines represent the stable (unstable) solutions. In red the homogeneous solutions are represented, the populated (P) and the unpopulated (U). In purple localized structures of holes embedded in the homogeneous solution. In green the stripes pattern (S) and orange represents the localized structures of patches. MI refers to the modulation instability, T to the transcritical, and SN to the saddle node. The parameters are: $\omega_b = 0.06$ $year^{-1}$, $b = 1.25$ $cm^4 year^{-1}$, $\kappa = 0.048$ $year^{-1}$, $\sigma_\kappa = 2851.3$ cm, $a = 27.38$ cm^2, $\sigma_\mu = 203.7$ cm, $d_0 = 631.2$ $cm^2 year^{-1}$, $d_1 = 4842.1$ $cm^4 year^{-1}$.
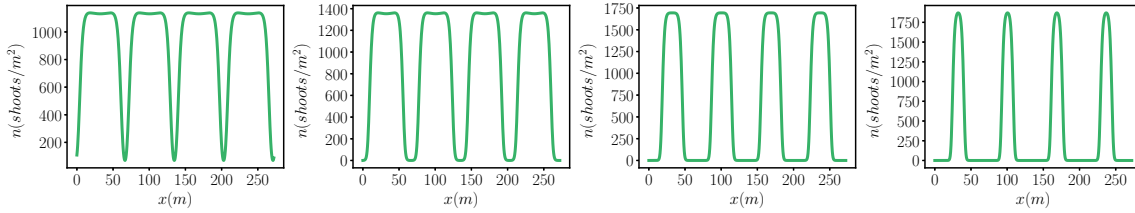
Figure 4.4: Different stable stationary solutions of stripes pattern for $\omega_{d0}/\omega_b = 1, 1.5, 2.45, 3.1$ from left to right. The other parameters are: $\omega_b = 0.06$ $year^{-1}$, $b = 1.25$ $cm^4 year^{-1}$, $\kappa = 0.048$ $year^{-1}$, $\sigma_\kappa = 2851.3$ cm, $a = 27.38$ cm^2, $\sigma_\mu = 203.7$ cm, $d_0 = 631.2$ $cm^2 year^{-1}$, $d_1 = 4842.1$ $cm^4 year^{-1}$.

of the branches where new holes are created is unstable while the other parts are stable. These localized structures are the result of the existence of an heteroclinic orbit in the spatial dynamics framework. This heteroclinic orbit is precisely the front connecting the pattern (periodic orbit) with the homogeneous solution (a saddle in the spatial dynamics). This scenario is associated to spatial chaos giving rise to all possible spatial profiles as combination of arbitrary sequences of localized structures separated by the homogeneous solution.

The formation of stable localized structures has dramatic effects on the dynamics. From a different perspective, a localized structure can be interpreted as two fronts

locked, both connecting the pattern and the homogeneous solution. Hence, the snaking region correspond to the region where the front connecting the two stationary solutions is also stationary. Thus, it is said the front is locked or pinned in this region also called the pinning region. Outside this region the front moves as we will see in the next section.

A different set of localized structures appears for higher values of mortality. Interestingly these are the last solution that persists before the only solution is bare soil. An isolated peak or patch is stable for high values of the mortality. As can be appreciated in Fig. 4.6, the branch bifurcates from the transcritical bifurcation in the limit of infinite system size. For a finite domain of size L, the solution bifurcates from the solution n_- when $\lambda(q = \frac{2\pi}{L}) = 0$ as an harmonic function with the wavelength L. Very quickly the width around the maximum shrinks along the branch to form the solution of one peak, which grows in amplitude until the saddle node around $\omega_{d0}/\omega_b \sim 3.55$. After the saddle node the solution stabilizes and grows in size while the maximum value diminishes as decreasing mortality. At a certain moment the central value becomes a relative minimum, which after the second fold splits the localized structure in two peaks. Later after the third fold all the structure diminishes in size and continues until very close to the transcritical bifurcation, more precisely to n_- when $\lambda(q = 2\frac{2\pi}{L}) = 0$, where the solution with a wavelength of half the system size bifurcates. In particular it is not clear if this branch bifurcates from the homogeneous branch or from the branch of two peaks, which clearly bifurcate from the homogeneous as it can be seen in Fig. 4.6. The numerical precision is insufficient to determine this connection with the chosen discretization. From the bifurcation of the two peaks solution an equivalent curve emerges where the solutions along the curved are the same than the previous case but formed by two peaks separated the system size. Each one of the peaks follows the same change in shape along the curve than the solution of one peak, both solutions have equivalent stability as shown in the panels in Fig. 4.6. Localized structures of isolated patches have been shown to be present in other vegetation models applied to arid ecosystems [119, 120] and in similar models applied to completely different topics [121]. In all cases the bifurcation diagram is similar and the work presented in [42] is particularly interesting as they show the connection of the two types of localized structures at the Maxwell point for a different parameter regime.

In the same way we did in the one dimensional case, the stationary solutions in two dimensions can be followed changing the mortality. We continuate negative hexagons and positive hexagons (Fig. 4.7). The pattern of stripes is equivalent to the one dimensional case. The solution of negative hexagons bifurcates from the modulation instability subcritically and the consecutive fold extends beyond the fold of the stripes. At this fold the solution stabilizes and generally remains stable until high values of mortality close to the next fold. Here, the solution jumps to an other
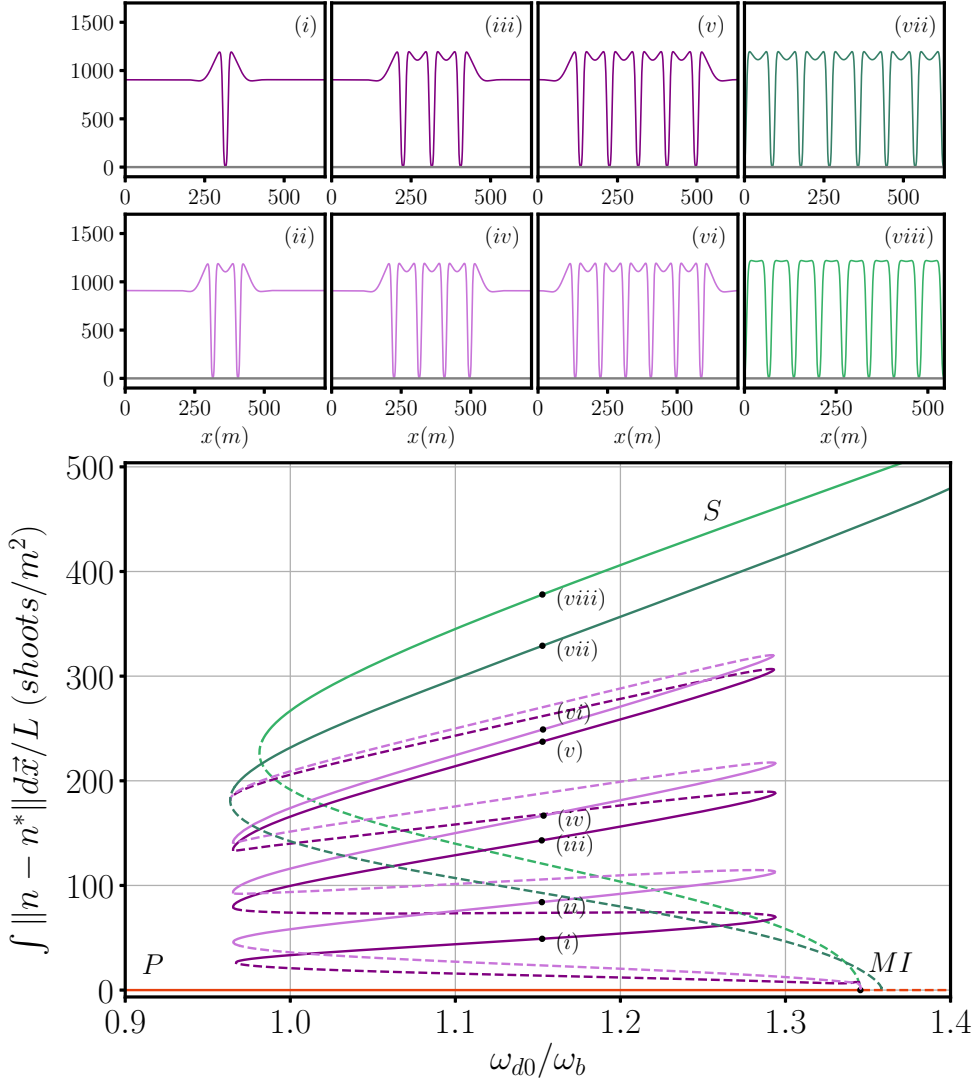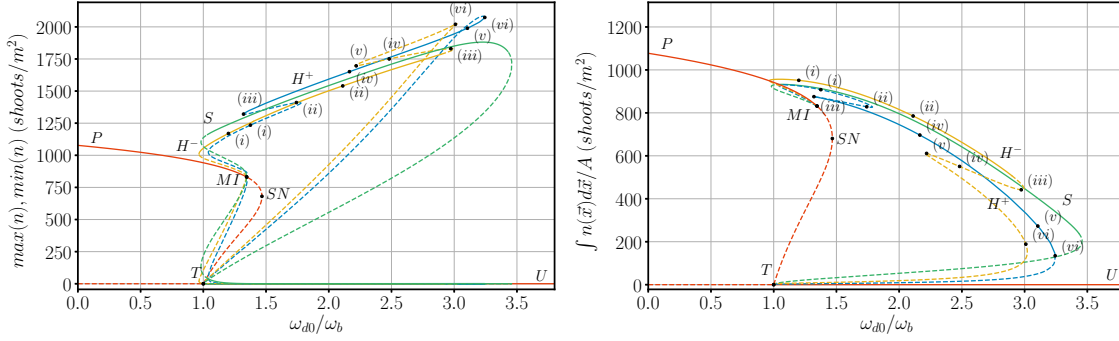
Figure 4.5: Bifurcation diagram as a function of the ratio ω_{d0}/ω_b using the norm of the difference to the homogeneous populated solution n^* (P) to better show the homoclinic snaking of the localized structures. Dark purple represents solutions with odd number of localized structures. Bright purple represents solutions with even number of localized structures. In green stripe patterns (S) with different wavenumber. One corresponds to the critical wavenumber while the other corresponds to the wavelength selected by the front between the pattern and the homogeneous solution. The solutions in the top panels correspond to the points indicated in the branches. Continuous (dashed) lines represent the stable (unstable) solutions. MI refers to the modulation instability. The parameters are: $\omega_b = 0.06\ year^{-1}$, $b = 1.25\ cm^4 year^{-1}$, $\kappa = 0.048\ year^{-1}$, $\sigma_\kappa = 2851.3\ cm$, $a = 27.38$ cm^2, $\sigma_\mu = 203.7\ cm$, $d_0 = 631.2\ cm^2 year^{-1}$, $d_1 = 4842.1\ cm^4 year^{-1}$.
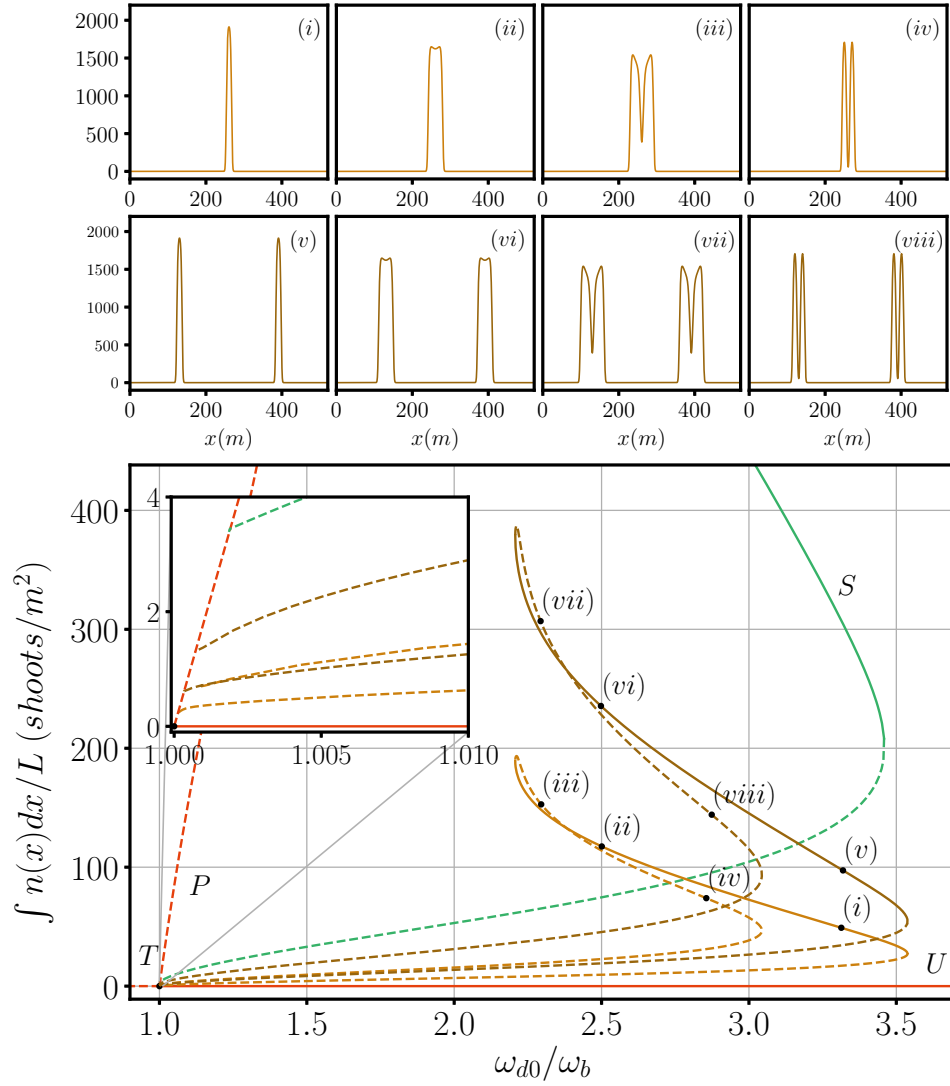
Figure 4.6: Bifurcation diagram as a function of the ratio ω_{d0}/ω_b using the average density. Yellow represents the solution of one peak while brown represents the solution of two peaks. In green the stripes pattern (S) and in red the homogeneous populated (P) and unpopulated (U) stationary solutions. The solutions in top panels correspond to the points indicated in the branches. Continuous (dashed) lines represent the stable (unstable) solutions. T refers to the transcritical bifurcation. The parameters are: $\omega_b = 0.06\ year^{-1}$, $b = 1.25\ cm^4 year^{-1}$, $\kappa = 0.048\ year^{-1}$, $\sigma_\kappa = 2851.3\ cm$, $a = 27.38\ cm^2$, $\sigma_\mu = 203.7\ cm$, $d_0 = 631.2\ cm^2 year^{-1}$, $d_1 = 4842.1\ cm^4 year^{-1}$.

Figure 4.7: Bifurcation diagram as a function of the ratio ω_{d0}/ω_b for two dimensional patterns. The maximum and minimum of the solution is used in the left panel while the average density is used in the right panel. In red the homogeneous populated solution (P) and the unpopulated (U). Yellow represents the branch of negative hexagons (H^-). Green represents the branch of stripes pattern (S) computed in one dimension. And blue represents the branch of positive hexagons (H^+). The dots indicated with roman numerals are represented in Figs. 4.8 and 4.9. Continuous (dashed) lines represent the stable (unstable) solutions. MI refers to the modulation instability, T to the transcritical, and SN to the saddle node. The parameters are: $\omega_b = 0.06 \ year^{-1}$, $b = 1.25 \ cm^4 year^{-1}$, $\kappa = 0.048 \ year^{-1}$, $\sigma_\kappa = 2851.3 \ cm$, $a = 27.38 \ cm^2$, $\sigma_\mu = 203.7 \ cm$, $d_0 = 631.2 \ cm^2 year^{-1}$, $d_1 = 4842.1 \ cm^4 year^{-1}$.

pattern depending on the relative stability of the different solutions. Along the branch the pattern changes similarly to the one dimensional case. The populated part of the solution shrinks and the maximum value grows. Thus the average density decreases while increasing mortality. After, the instability the unstable part of the branch folds. At the fold the holes have become big enough to touch between them leaving triangles in the middle (see Fig 4.8). After the fold the triangles become round and in a second fold the solution transforms in a pattern of patches located at the vertices of an hexagon. Later, after the last fold, the density decrease maintaining the spatial arrangement and finally connects with the homogeneous branch n_- close to transcritical. The different spatial distribution can be seen in the Fig. 4.8.

The solutions of positive hexagons has a similar behavior when changing mortality (Fig. 4.9). It is stable for high values of the mortality and loses stability after the fold at $\omega_{d0}/\omega_b \sim 3.25$. After the fold the unstable branch follow until its bifurcation close to the transcritical bifurcation of the zero solution. Equivalently to previous cases, higher values of the mortality lead to more compact distributions and higher values of the maximum density. When decreasing mortality the solution loses stability and it jumps to a different pattern. Similarly to the previous case the branch continues, and the spots in the hexagonal lattice become big enough to touch between them. They form triangles that after the fold become round and after the next fold form spots

69
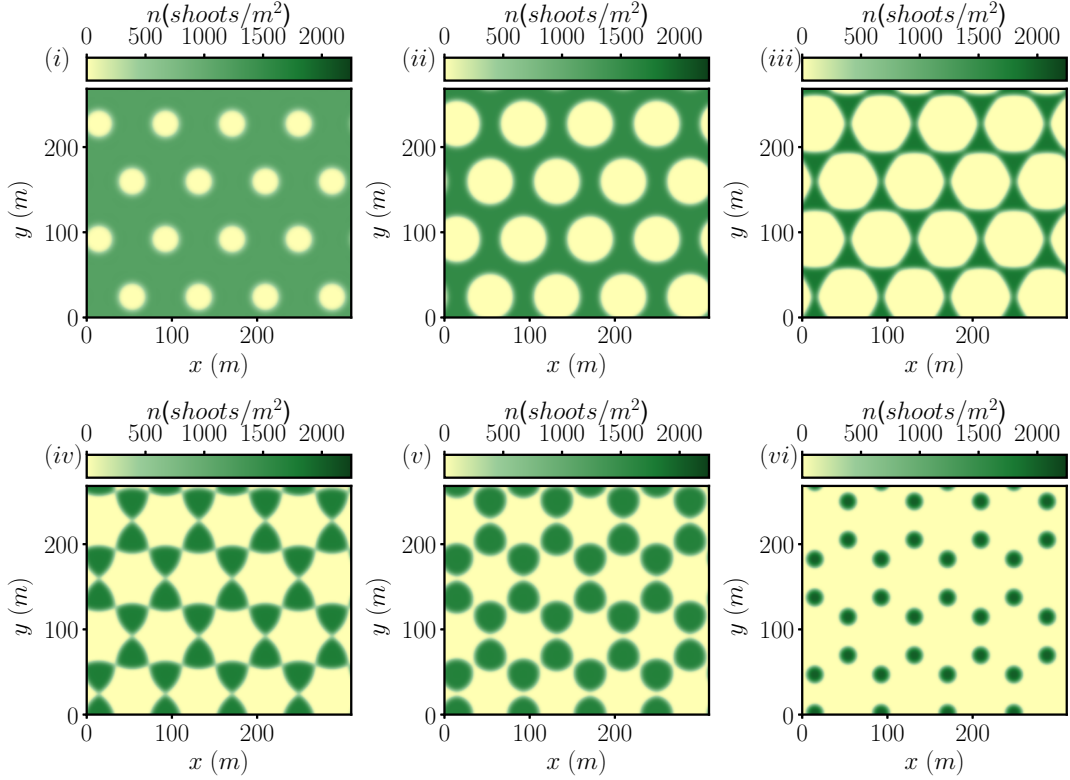
Figure 4.8: Different stationary solutions of the branch of negative hexagons. The panels correspond to the dots indicated in Fig. 4.7. The mortalities are $\omega_{d0}/\omega_b = 1.2$, 2.11, 2.97, 2.48, 2.22, 3.01 n the order specified by the numerals and the other parameters are $\omega_b = 0.06\ year^{-1}$, $b = 1.25\ cm^4 year^{-1}$, $\kappa = 0.048\ year^{-1}$, $\sigma_\kappa = 2851.3\ cm$, $a = 27.38\ cm^2$, $\sigma_\mu = 203.7\ cm$, $d_0 = 631.2\ cm^2 year^{-1}$, $d_1 = 4842.1\ cm^4 year^{-1}$.

arranged in the vertices of an hexagon. Two extra folds follow, the first is for higher values of mortality than those for the stripes pattern and the negative hexagons. The second fold is very close to the modulation instability where the branch bifurcates supercritically as expected from the theory of pattern formation. In Fig. 4.7 the branch of negative hexagons with indicated solutions represented is shown in Fig. 4.9. These atypical configurations are for the two branches are in all cases unstable solutions, which means they will not be observed. From the theoretical point of view it is interesting the bifurcation structure of the mode. It is possible that the high number of folds can be attributed to the highly nonlinear regime, different number of folds have been found in a Swift-Hohenberg equation with high order nonlinearities [122].

Beyond the three patterns analyzed more spatial structures are expected to be stable. Localized structures are an example. Holes and spots with radial symmetry
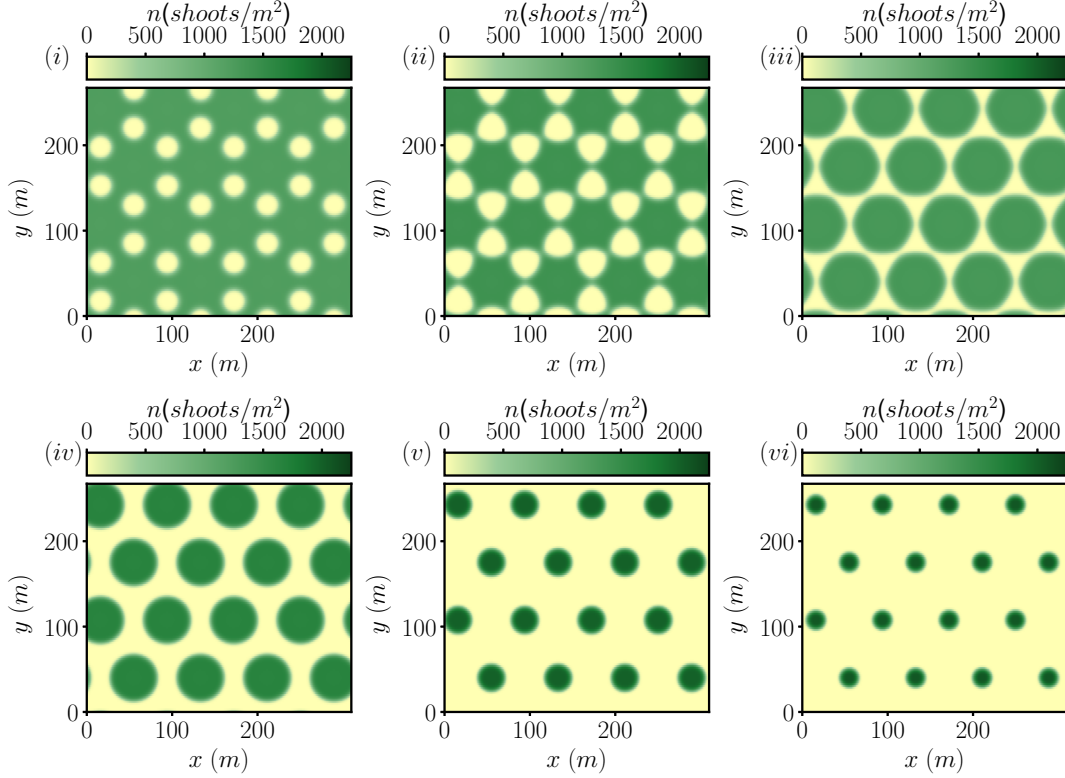
Figure 4.9: Different stationary solutions of the branch of positive hexagons. The panels correspond to the dots indicated in Fig. 4.7. The mortalities are $\omega_{d0}/omega_b = 1.38, 1.74, 1.32, 2.17, 3.11, 3.24$ in the order specified by the numerals and the other parameters are $\omega_b = 0.06\ year^{-1}$, $b = 1.25\ cm^4 year^{-1}$, $\kappa = 0.048\ year^{-1}$, $\sigma_\kappa = 2851.3\ cm$, $a = 27.38\ cm^2$, $\sigma_\mu = 203.7\ cm$, $d_0 = 631.2\ cm^2 year^{-1}$, $d_1 = 4842.1\ cm^4 year^{-1}$.

are expected to be found in similar regions than its one dimensional analogs. Rings of vegetation have been found in similar models [123, 121] and other more complex structures lacking radial symmetry. The difficulty associated to computing these structures is the large arrays that must be considered, essentially the tails can not be neglected and large domains are necessary. At difference with the case of patterns, where only the Brillouin zone is considered, localized structures are more computationally demanding. Radial structures have the advantage that with the proper change of variables the solution can be computed in one dimension, describing only the radial profile. From this perspective more work is needed to fully characterize the bifurcation diagram for two dimensional solutions and its stability.

The bifurcation diagram is not only a compact summary of the stationary solutions of the model but it also provides information about the dynamics. The stability of the solutions gives important information about the evolution of the system for

all values of ω_{d0}/ω_b. The extensions of different branches determine the thresholds under which the meadow may experience sudden transitions. Moreover, the recovery of vegetation is determined by the unstable branches which act as barriers between growth or decay, giving valuable information for reforestation projects. Finally the relative stability between stationary solution may determine the evolution of different patterns one close to the other. In other words, a front connecting to stationary solutions may move according to the relative stability of the two confronted solutions [124]. This dynamics is studied in the next section.

4.3 Vegetation fronts

The two dimensional case has multiple connections between different stationary solutions. Fronts between stripes and positive hexagons, stripes and negatives hexagons, positive and negative hexagons are the simplest combinations one can imagine. However, more complicated scenarios accounting for the orientation of the patterns with respect to the front or connections involving three stationary solutions, in the cases in which there is tristability, are also valid possibilities. The difficulty of the analysis in the two dimensional case is considerable and it will not be tackled here. Instead, we focus in the one dimensional case in order to gain understanding on the relevant factors determining the evolution of these spatial profiles.

Multiple solutions simultaneously present for the same parameter values allow the formation of fronts. The homogeneous populated solution (P), the unpopulated solution (U) and the stripes pattern (S) coexist in different regions making possible the existence of different fronts in different ranges. We study the front connecting the populated solution with the unpopulated solution (P-U), the front connecting the populated solution with the stripes pattern (S-P) and the front connecting the stripes pattern with the unpopulated solution (S-U). The fronts, according to the stability of the solutions involved, can be classified in two types. Those involving two stable states are called pushed fronts while those involving a stable state and an unstable state are called pulled fronts. The motion of the first is driven by the relative stability between the two solutions which is determined by nonlinear mechanism. On the contrary pulled fronts are driven by linear mechanisms. Basically, perturbations that grow on the edge of the fronts drive the evolution, being the motion determined by the eigenvalues of the unstable solution. Thus, being the evolution of the front determined by linear mechanisms it is possible to compute the velocity of propagation using a linear calculation, as we will do in the next pages. On the following we perform numerical simulation with the pseudospectral method explained in Appendix C using periodic boundary conditions with $n = 16384$ number of points, which allows to simulate big domains that allow the propagation of the front for long distances.

Studying in first place the front P-U, we can distinguish two cases, when $\omega_{d0}/\omega_b >$ 1 the front is a pushed front and there should be a Maxwell point where the velocity goes to zero. The presence of modulation instability hides the Maxwell point since the homogeneous populated solution becomes unstable after the MI. Besides, when $\omega_{d0}/\omega_b > 1$ the pushed front and the pulled fronts exist simultaneously being the one with bigger velocity the one that prevails. This crossover of the velocity is usually noticeable when representing the velocity of the front as a function of the control parameter. In our case there is a change of tendency of the velocity as a function of mortality, however it is barely unnoticeable (see Fig. 4.10). Interestingly, the velocity of the P-U front is not well predicted by the linear calculation. To clarify the reason, we have performed a numerical simulation without the term $d_1 \|\nabla n\|^2$, which is nonlinear and is not considered the linear calculation (blue dot in Fig. 4.10). However, the effect is very small and we can not attribute the discrepancy to this term. A second simulation has been done also removing long-range competition, more precisely with $\sigma_\kappa = 0$ (black dot in Fig. 4.10). The velocity removing this term coincides accurately with the analytical prediction. Hence, the long-range competition can inhibit the growth of the unpopulated solution, basically because the homogeneous solution compete at a distance ahead of the front, which limits the growth of new plants. Closer to the Turing instability the homogeneous front loses stability against modulations in the populated part. There is a small coexistence range between the fronts P-U and S-U, where the two fronts are possible. Thus, we see the front S-U appears for $\omega_{d0}/\omega_b > 1.263 - 1.291$ and the homogeneous front exist until $\omega_{d0}/\omega_b < 1.333$, both before the Maxwell point of the front P-U. In Fig. 4.10 we can see a space time representation of the evolution of the front with the only particularity of having a maximum at the interface of the front produced by long-range interactions. Moreover, Fig. 4.10 (right) shows the dependence of the front velocity with ω_{d0}/ω_b.

In second place, the front S-U which prevails for $\omega_{d0}/\omega_b > 1.263 - 1.291$ is a pushed front and it is present until $\omega_{d0}/\omega_b = 2.207$ where the pinning region begins. The pinning region corresponds to the range of mortalities where the velocity of the front is zero, and the front is locked, which coincides with region of existence of localized structures as expected and as it can be seen in Figs. 4.5 and 4.11. The connection of the unpopulated solution with the pattern in the central part of the front is quite similar to the connection between the unpopulated and populated solutions. May be that is the reason why the dependence of the velocity with mortality is so similar in the two fronts. This particular shape, which can be seen in Fig. 4.11, resembles the P-U front propagating leaving stripes behind. Moreover, we note this interface produces phase slips as it moves, where the first patch expands and changes its wavelength until two patches are created from the division of the first.

The last front we study is the pattern of stripes connecting with the homogeneous
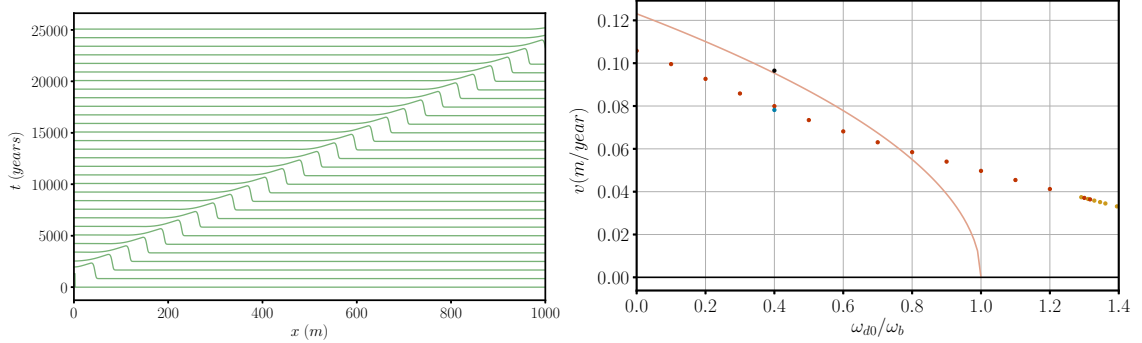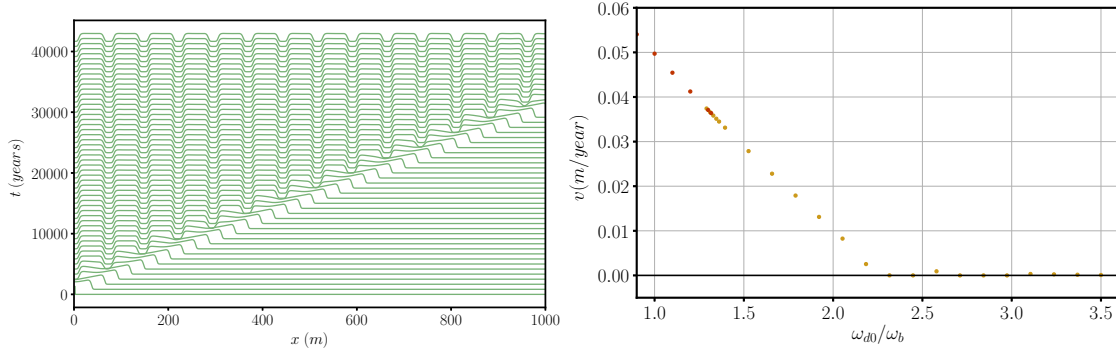
Figure 4.10: Left: Space time representation of the front connecting the two homogeneous solutions populated and unpopulated P-U for $\omega_{d0} = 0.0679 \; year^{-1}$. Right: Velocity of the front P-U for different values of mortality. In both panels the parameters are: $\omega_b = 0.06 \; year^{-1}$, $b = 1.25 \; cm^4 year^{-1}$, $\kappa = 0.048 \; year^{-1}$, $\sigma_\kappa = 2851.3 \; cm$, $a = 27.38 \; cm^2$, $\sigma_\mu = 203.7 \; cm$, $d_0 = 631.2 \; cm^2 year^{-1}$, $d_1 = 4842.1 \; cm^4 year^{-1}$.

populated solution (S-P). In this case the distinction pulled and pushed fronts can be made again in terms of the relative position to the Turing instability. Before the onset of the Turing instability $\omega_{d0c}/\omega_b = 1.345$ the only possible front is the pushed front, which persist until the beginning of the pinning region $\omega_{d0}/\omega_b = 1.294$ where the velocity goes to zero and the front is locked. Beyond the Turing instability, again, the front with bigger velocity prevails, as it can be seen in Fig. 4.12 the pushed front goes beyond the Turing until the velocity of the pulled front overcomes the velocity of the pushed front. The pulled front S-P exist until the saddle node bifurcation.

The prediction of the velocity v of the pulled front can be obtained according to [125–127, 127] considering perturbations with the form $e^{ikx+\lambda(k)t}$ which in the co-moving reference frame $x' = x - vt$ are $e^{ikx'+\Lambda(k)t}$ where $\Lambda(k) = ikv + \lambda(k)$. Thus, applying the marginal stability criteria, $Re\left[\Lambda(k)\right]=0$ and $\frac{d\Lambda(k)}{dk} = 0$ one can obtain three coupled equations from which the velocity v and the real and imaginary part of the wave number, k_r, k_i, representing the wavenumber of the front and the spatial decay of its envelope can be computed. Thus, the equations are $v = \frac{Re[\lambda(k)]}{k_i}$, $Re\left[\frac{d\lambda(k)}{dk}\right] = 0$ and $v = -Im\left[\frac{d\lambda(k)}{dk}\right]$, which written in in terms of k_r, k_i, and v read

$$
\begin{aligned}
vk_i \;=\; & -2bn^{*2} - (d_0 + d_1 n^*)(k_r^2 - k_i^2) \\
& -an^* e^{-an^*}\left(\kappa e^{-(k_r^2 - k_i^2)\frac{\sigma_\kappa^2}{2}} \cos\left(k_r k_i \sigma_\kappa^2\right) - \omega_{d0} e^{-(k_r^2 - k_i^2)\frac{\sigma_\mu^2}{2}} \cos\left(k_r k_i \sigma_\mu^2\right)\right).
\end{aligned}
$$
(4.6)

Figure 4.11: Left: Space time representation of the front connecting the stripes pattern with the unpopulated solution S-U for $\omega_{d0} = 0.0837 \; year^{-1}$. Right: Velocity of the homogeneous front S-U for different values of mortality. In both panels the parameters are: $\omega_b = 0.06 \; year^{-1}$, $b = 1.25 \; cm^4 year^{-1}$, $\kappa = 0.048 \; year^{-1}$, $\sigma_\kappa = 2851.3 \; cm$, $a = 27.38 \; cm^2$, $\sigma_\mu = 203.7 \; cm$, $d_0 = 631.2 \; cm^2 year^{-1}$, $d_1 = 4842.1 \; cm^4 year^{-1}$.

The second condition is

$$
\begin{aligned}
0 = & \left(-(d_0 + d_1 n^*) \right. \\
& + an^* e^{-an^*} \left(\kappa e^{-(k_r^2 - k_i^2)\frac{\sigma_\kappa^2}{2}} \cos\left(k_r k_i \sigma_\kappa^2\right)\frac{\sigma_\kappa^2}{2} - \omega_{d0} e^{-(k_r^2 - k_i^2)\frac{\sigma_\mu^2}{2}} \cos\left(k_r k_i \sigma_\mu^2\right)\frac{\sigma_\mu^2}{2} \right) \right) 2k_r \\
& + an^* e^{-an^*} \left(\kappa e^{-(k_r^2 - k_i^2)\frac{\sigma_\kappa^2}{2}} \sin\left(k_r k_i \sigma_\kappa^2\right)\frac{\sigma_\kappa^2}{2} - \omega_{d0} e^{-(k_r^2 - k_i^2)\frac{\sigma_\mu^2}{2}} \sin\left(k_r k_i \sigma_\mu^2\right)\frac{\sigma_\mu^2}{2} \right) 2k_i.
\end{aligned}
$$
(4.7)

And finally the third

$$
\begin{aligned}
v = & \left(+(d_0 + d_1 n^*) \right. \\
& - an^* e^{-an^*} \left(\kappa e^{-(k_r^2 - k_i^2)\frac{\sigma_\kappa^2}{2}} \cos\left(k_r k_i \sigma_\kappa^2\right)\frac{\sigma_\kappa^2}{2} - \omega_{d0} e^{-(k_r^2 - k_i^2)\frac{\sigma_\mu^2}{2}} \cos\left(k_r k_i \sigma_\mu^2\right)\frac{\sigma_\mu^2}{2} \right) \right) 2k_i \\
& + an^* e^{-an^*} \left(\kappa e^{-(k_r^2 - k_i^2)\frac{\sigma_\kappa^2}{2}} \sin\left(k_r k_i \sigma_\kappa^2\right)\frac{\sigma_\kappa^2}{2} - \omega_{d0} e^{-(k_r^2 - k_i^2)\frac{\sigma_\mu^2}{2}} \sin\left(k_r k_i \sigma_\mu^2\right)\frac{\sigma_\mu^2}{2} \right) 2k_r.
\end{aligned}
$$
(4.8)

The three equations can be solved numerically to find k_r, k_i, and v for each parameter set. Notice the solutions of the problem can be multiple, since the trigonometric functions are multivalued. However one can analyze the three conditions to reach the conclusion that the solution with maximum velocity dominates. In Fig. 4.12 one can

75
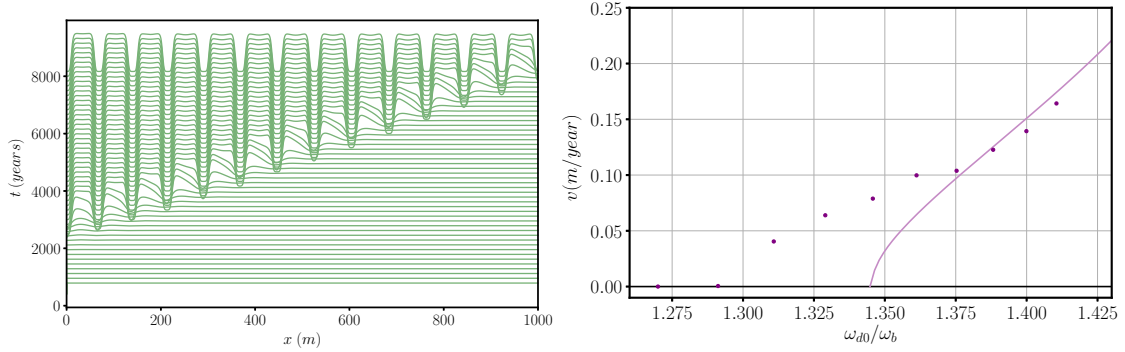
Figure 4.12: Left: Space time representation of the front connecting the stripes pattern with the populated solution S-P for $\omega_{d0} = 0.0846 \ year^{-1}$. Right: Front velocity as a function of ω_{d0}/ω_b. Dots correspond to numerical simulations while the continuous line represents the linear prediction. The parameters are: $\omega_b = 0.06 \ year^{-1}$, $b = 1.25 \ cm^4 year^{-1}$, $\kappa = 0.048 \ year^{-1}$, $\sigma_\kappa = 2851.3 \ cm$, $a = 27.38 \ cm^2$, $\sigma_\mu = 203.7 \ cm$, $d_0 = 631.2 \ cm^2 year^{-1}$, $d_1 = 4842.1 \ cm^4 year^{-1}$.

see the linear velocity and the agreement with numerical simulations. One can follow the same procedure to compute the velocity of the pulled front P-U using 4.3 which gives $k_r = 0$, $k_i = \sqrt{(\omega_b - \omega_{d0})/d_0}$ and $v = 2\sqrt{d_0(\omega_b - \omega_{d0})}$ and it is represented in Fig. 4.10.

4.4 Conclusions

In this chapter we have focused on the analysis of the simplified equation introduced in Chapter 3 preserving the full nonlocal interactions. Through a linear stability analysis, continuation techniques of stationary solutions, and numerical simulations of fronts, we have characterized the dynamics in the one dimensional case and obtained some results in the two dimensional case. The linear stability reveals the presence of a Modulation Instability in agreement with previous chapters. As a result, the standard sequence of patterns increasing mortality emerges. However, more complex patterns appear along the branches with different spatial distributions. This fact leads to the question of where the branches of hexagons end up, having in mind the results in [35], where the branches of patterns emerge from a Turing instability and end in a second Turing instability one could expect to have a similar behavior. In the one dimensional case we have analyzed in more detail the bifurcation diagram, focusing mainly in the structure of the branches of localized structures. More precisely, we have shown the structures associated to fairy rings are the result of bistability between the homogeneous populated solution and the pattern, which

give rise to the formation of the snaking region. On the other side of the bifurcation diagram, localized structures in the form of spots have different bifurcation diagram where successive number of peaks emerge from n_- very close to the transcritical bifurcation. In the last part, we have shown how the formation of localized structures determines the dynamics of fronts between the different stationary states. Outside the pinning regions the fronts move with velocity different from zero which changes with mortality. In the cases where fronts are pulled we predict the velocity using linear theory. For pushed fronts more involved calculations are necessary which are not possible in our case due to the particular form of the equation. Instead we have used numerical simulations in large domains to simulate the evolution. In the light of these results we aim to devote more effort to the stability and the evolution of fronts of the two dimensional case. The results obtained here allow to understand more deeply the dynamics of vegetation. In particular, the formation of patterns in the ABD model can be studied quite accurately using the simplified version of the model preserving full nonlocal interactions. Thus, the bifurcation diagram and the numerical simulations presented address important questions from the biological point of view. For instance, the unstable branches of patterns are important information from the reforestation point of view, since they provide the value of the density that has to be planted in order for the plant to succeed, but more importantly, they also give information about the spatial distribution that has to be used in reforestation projects. Obviously, reforestation will be more complicated than arranging plants in a certain distribution, but the model can provide important insights. Bistability between different solution also can have important consequences for seagrasses, essentially the evolution of fronts is of certain importance when the ecosystem is under the influence of changing environmental factors. Thus, under external changes, the meadow will experience a change in spatial distribution, which will occur through a front. Thus, the time scale evolution of the ecosystem will be determined by the relative stability between different patterns, which is a result very difficult to predict without a model. In essence, the theoretical prediction from bifurcation theory can be of important relevance for the evolution of the ecosystem.

Sulfide concentration as a mechanism for pattern formation and complex dynamics

Spatial heterogeneity of vegetation affecting different habitats globally has important implications for the functionality of the ecosystem. Primarily, the distribution of resources changes completely according to the prevalence of homogeneous vegetation or heterogeneous coverage [128]. Beyond that, the effects are profound because different factors of the trophic chain are susceptible to the changes vegetation may experience. From this perspective vegetation, which is really the basis of the ecosystem is better understood as a dynamic part rather than a fixed scenario where other organisms are developing. Nevertheless, the dynamics of the spatial distribution of vegetation is poorly understood mainly because the mechanisms which drive the evolution operate at a certain distance, making the measurement of these interactions difficult. Self-organization is an important manifestation of the presence of long-range interactions. When there is a balance between growth and death, interactions can become important enough to drive the evolution of the system. Thus, spatial interactions give rise to the formation of regular patterns of vegetation, creating a striking view that shapes all the landscape. Namibian fairy circles are an important example of this phenomenon [31, 28, 26] but many other ecosystems exhibit the same process. Fairy circles in Australia, patchy vegetation in Sudan, bands in Niger, labyrinths in northern Negev [34, 24, 23, 32, 13, 129] are different examples. Pattern formation is usually associated with the presence of stressing conditions to the plants, however, from the academic point of view, it is really convenient since it allows to extract more knowledge of the interactions mechanisms, mainly because the typical length of the pattern is directly related with the length of operation of the leading mechanism. In arid ecosystems the diffusion of rainfall water is the main explanation for the formation of these vegetation patterns, however, other hypotheses have been considered being an important topic of scientific discussion.

Chapter 5. Sulfide concentration as a mechanism for pattern formation and complex dynamics

In marine ecosystems, vegetation patterns have been less studied, at least from the theoretical point of view [55, 130, 131]. Mainly experimental studies of spatial heterogeneity have been reported, not always clarifying the responsible mechanisms. Banded vegetation associated to sand dunes due to wave exposure [132, 55], leopard skin [53], stripped patterns [54], rings of vegetation in *Zostera marina* in the Danish Kattegat [56] and *Posidonia oceanica* in the Corsican coast [58]. Above all, the largest patterns found in marine habitats are those formed by *Posidonia oceanica* around the Balearic Islands. Patterns of mainly bare circular holes extending over regions of kilometers in both Pollença and Alcudia bays [59].

No matter terrestrial or marine vegetation patterns have a common feature, long-range competition mechanisms are necessary for the formation of these regular structures, as shown in chapter 1. For the case of *Posidonia oceanica*, there is not a known mechanism explaining the nature of the interactions. Different explanations are possible, however, the interaction length around $\sigma \sim 30 \ m$ points to mechanisms related to water movement, which makes from our perspective two hypotheses the most plausible explanations. The first hypothesis is based on hydrodynamics, basically, vegetation would adapt its distribution modifying the dissipation of wave energy in such a way that the probability of survival is enhanced. The second hypothesis compatible with the typical distance of interaction corresponds to the diffusion of organic matter produced by the plant, whose decomposition produces sulfides in the sediment. Sulfides in the sediment have been reported to be toxic to the plant. In fact, it is possible that both mechanisms play an important role simultaneously. Nevertheless, as a first step, the last hypothesis is the one we are going to explore in this chapter, while the first will be addressed in future works.

The production of hydrogen sulfide is part of the sulfur cycle, a predominant biogeochemical process in marine environments with important implications on the conditions of growth of different species of seagrasses. Although its ubiquity and the large efforts in the study of the process, not all mechanisms involved are clear yet. One thing is clear, sulfides in the sediment have been reported to be extremely toxic to seagrasses [133], where intrusion through the roots inhibits the growth of the plant. As a matter of fact, in the Danish Kattegat the reported rings of vegetation were the result of increased shoot mortality in the center due to sulfide invasion. Thereby, the formation of this vegetation structure points to sulfide dynamics as an important factor driving spatial organization. From this perspective, there seems to be a strong coupling between the evolution of the seagrass and the evolution of this phytotoxin. This is in fact the case, the presence of seagrass increases sedimentation of organic matter in the surroundings, thus this organic carbon is oxidized by sulfate-reducing bacteria, which reduce sulfates $(S0_4^{2-})$ into hydrogen sulfide (H_2S). Then, the latter can be absorbed by the plant and reach different parts, starting from the invasion of roots, through the meristem to the leaves, and finally the invasion of

the plant tissue inhibits the growth leading to prone mortality. In this fashion, all the necessary ingredients are present to have a long-range competitive interaction. However, it becomes necessary to consider the process from a quantitative point of view. Therefore, one needs to account for four different things: the rate of production of sulfides, the rate of removal, the diffusion in space of organic matter and the effect of a given concentration in shoots mortality.

First of all, Sulfate Reduction Rates (SRR) measure the production of sulfides, however, this flux can not be associated directly to the net production mainly because these sulfides are oxidized back again to sulfates if oxygen is present in the upper layer of the sediment. Furthermore, seagrasses introduce oxygen into the soil as a protection mechanism against sulfide intrusion, which increases reoxidation. Thus in a cyclic way sulfates are available to be reduced again. Hence if one wants to consider the net production of sulfide it is necessary to consider the balance of these two quantities. SRR and sulfide and sulfate concentrations are common measures in the literature [134–138, 56] ranging between $100 - 500 \ \mu M/d$, $1 - 300 \ \mu M$, and ~ 30 mM respectively. However, there are fewer estimations of the reoxidation process [134]. Luckily, the time evolution of sulfides has been measured for *Zostera marina* giving a better estimation of the time scale, which is of the order of months to one year, rather than the rate provided by SRR.

Second, regarding the removal of sulfides, two processes are possible. On the one hand hydrogen sulfide combines with iron to form pyrite (FeS_2). On the other hand, hydrogen sulfide is directly absorbed resulting in intoxication of the plant [139]. The contribution of each process to the total removal it is not clear, moreover, it can depend on the properties of the substrate. For instance it is known carbonate sediments characterized by low iron availability make seagrasses like *P.Oceanica* more sensitive to sulfide intrusion [136, 135, 140–143].

Third, various studies about fish farming effects on the surroundings have quantified in terms of organic matter spreading the distribution of different chemical components with distance, including sulfides and its effects on *P. oceanica* [144–147]. These results show how the production of organic matter in a given position can affect the growth at important distances, as far as hundreds of meters away.

Finally, direct measurements of demographic activity of *P.oceanica* in presence of different sulfide concentrations indicate a clear relation of the effects of sulfides on mortality, reducing the growth up to $15\% yr^{-1}$ for moderate sulfide concentrations around $30 \mu M$ [135].

The previous evidence indicates sulfur cycle as a plausible explanation of pattern formation in seagrass ecosystems. However, the scales of the involved process are crucial in order to clarify if this mechanism can explain a long-range competition.

In this chapter, we aim to develop a quantitative model based on the work on clonal growth developed in the previous chapters in combination with a simple equa-

tion describing the dynamics of sulfide concentration. We are going to explore the consequences of the coevolution between seagrass and sulfides and try to answer the questions related to the mechanism behind the formation of patterns in *P.oceanica* and other species.

The chapter is organized as follows: In Section 5.1 we propose the model and perform the mathematical analysis. Section 5.2 is devoted to parametrize the model for *P.oceanica*. Section 5.3 the model is parametrized for *Z.marina*. Finally some conclusions and remarks are given in Section 5.4.

5.1 Model for coupled vegetation and sulfide concentration

For the sake of simplicity, we use here the simplified version of the ABD model rather than the full description. The model has some limitations but this simplifies the understanding of the phenomena in a first approach to the problem. Since we want to explain the origin of long-range interactions we exclude the kernel term from the equation. Thus the evolution of the density of vegetation $n \equiv n(\vec{x}, t)$ is described by

$$\partial_t n = (\omega_b - \omega_d(n, S))n + d_0 \nabla^2 n + d_1 n \nabla^2 n + d_1 \|\nabla n\|^2, \qquad (5.1)$$

where $\nabla = (\partial_x, \partial_y)$, and now the mortality rate does not depend only on the local density but also on the concentration of porewater hydrogen sulfide S in μM. We consider a linear dependence of the mortality on S [135]:

$$\omega_d(n, S) = \omega_{d0} - an + bn^2 + \gamma S, \qquad (5.2)$$

where the parameter γ measures the increment of the mortality rate for each unit of concentration. The evolution of the sulfide concentration is dominated by three processes, the diffusion of organic matter produced by the plant, production of sulfides due to decomposition and sulfide removal. In fact, it is possible to describe the evolution of both organic matter and sulfides with two equations similarly to [131], where organic matter diffuses to the surroundings and generates sulfides. However, we prefer to use a simpler description accounting only for sulfide concentration, thus, effectively, sulfides are produced proportionally to death plants $c_s \omega_d(n, S)n$ and its diffusion encompasses not only diffusion of sulfides in the sediment but diffusion of organic matter on the water column due to the flow. Thus, the evolution of the concentration of sulfide $S \equiv S(\vec{x}, t)$ is described by

$$\partial_t S = c_s \omega_d(n, S)n - \delta_s S + D_s \nabla^2 S, \qquad (5.3)$$

where c_s accounts for the increment of concentration for each dead shoot, δ_s is rate of removal of sulfides and D_s is the effective diffusion of sulfides. We consider all parameters to take only positive values. Thus with the previous equations, we are able to reproduce the coupled dynamics between vegetation and sulfide concentration and determine the effect of this toxic compound on the growth of the meadow. These two equations describe the main processes explained above and schematized in Fig. 5.1

Vegetation density n

Sulfide concentration S
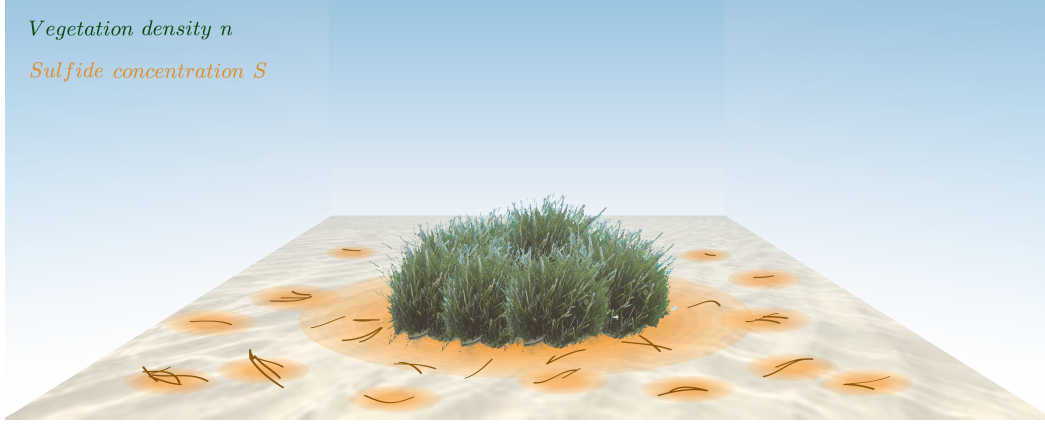
Figure 5.1: Sketch of the diffusion of organic matter produced by the plant which is accumulated in the soil increasing sulfide concentration on the sediment and inhibiting the growth. This generates an effective long-range competition mechanism which can be the explanation of the formation of vegetation patterns under the sea.

The stationary homogeneous solution given by n^* and S^* corresponds to the case in which there is a balance between branching and mortality, $\omega_b - \omega_d(n^*, S^*) = 0$. In this regime the concentration of sulfide is proportional to the stationary density $S^* = \frac{c_s \omega_b}{\delta_s} n^*$ and so n^* is the solution of a second order polynomial.

$$
n_\pm^* = \frac{a - \frac{\gamma c_s \omega_b}{\delta_s}}{2b} \pm \sqrt{\left(\frac{a - \frac{\gamma c_s \omega_b}{\delta_s}}{2b} \right)^2 + \frac{\omega_b - \omega_{d0}}{b}}.
\tag{5.4}
$$

We do not consider negative values of the vegetation density since they do not have any physical meaning. Thus two regimes can be distinguished: On the one hand, when $a < \frac{\gamma c_s \omega_b}{\delta_s}$ the populated solution only exist for $\omega_{d0} < \omega_b$, otherwise the only possible solution is bare soil $n^* = S^* = 0$. This is the transcritical bifurcation (T) of the unpopulated solution. On the other hand, when $a > \frac{\gamma c_s \omega_b}{\delta_s}$ the populated solution exists beyond the critical value $\omega_{d0} = \omega_b$ until the value of the mortality

$$
\omega_{d0_{SN}} = \omega_b + \frac{\left(a - \frac{\gamma c_s \omega_b}{\delta_s} \right)^2}{4b},
\tag{5.5}
$$

where a saddle-node bifurcation (SN) occurs. In this regime the transition from the populated to the unpopulated solution is subcritical, and this range corresponds to the bistability domain where there is a coexistence of the populated and the unpopulated solution. The presence of sulfides is proportional to the density of vegetation, hence there is a negative effect for the plant when the vegetation is denser, as a result, there is a competition between local facilitation given by a and the presence of sulfides, when facilitation overcomes this negative effect the homogeneous solution is bistable and vegetation persist for values of mortalities above the limit $\omega_{d0} = \omega_b$.

5.1.1 Pattern formation

The stability of the homogeneous solutions can be analyzed with a linear stability analysis. We consider small perturbations around the homogeneous solution with the form $n = n^* + \delta n e^{i\vec{q}\cdot\vec{x}}$ and $S = S^* + \delta S e^{i\vec{q}\cdot\vec{x}}$, which yields to the following characteristic polynomial

$$
\begin{aligned}
\lambda^2 - \lambda((a - 2bn^*)n^* + c_s\gamma n^* - \delta_s - ((d_0 + d_1 n^*) + D_s)q^2) \\
-(a - 2bn^*)n^*\delta_s + c_s\omega_b\gamma n^* \\
+(-(a - 2bn^*)n^*D_s - (d_0 + d_1 n^*)c_s\gamma n^* + \delta_s(d_0 + d_1 n^*))q^2 \\
+D_s(d_0 + d_1 n^*)q^4 = 0,
\end{aligned} \tag{5.6}
$$

where $q \equiv \|\vec{q}\|$ and λ corresponds to the temporal eigenvalues. Analyzing first the stability of the unpopulated solution $n^* = 0$ the eigenvalues are $\lambda = \omega_b - \omega_{d0} - d_0 q^2$ and $\lambda = -\delta_s - D_s q^2$. There is a change of stability of the first eigenvalue at $q = 0$ which correspond to the transcritical bifurcation. Second, the stability of the populated solutions is not so simple, the analytical expressions have a complicated dependence on parameters as can be seen in Appendix B, so we represent the changes of stability in the phase diagram in Fig. 5.2. Different analytical relations can be obtained but they are not insightful given the complicated dependence with parameters.

The populated solution is stable when mortality is low, meaning vegetation under low stress can resist the presence of sulfides. When increasing mortality, at a certain point vegetation can not resist anymore and becomes unstable. The populated solution is susceptible to become unstable in two different ways. On the one hand, it can experience an homogeneous oscillatory instability, also known as Hopf bifurcation where vegetation experience periodic cycles. This can be understood easily if one considers the vegetation growing and producing sulfides as time goes. At a certain point the concentration of the toxin is so high that the vegetation can not handle it and starts to decrease. If vegetation decreases the production of sulfides decreases
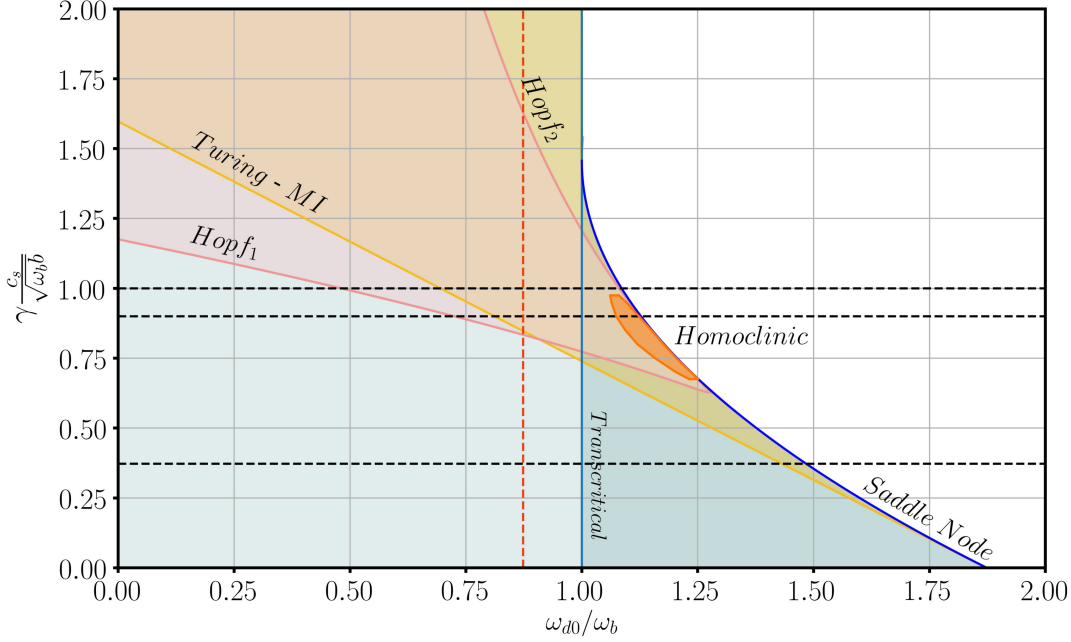
Figure 5.2: Phase diagram using the adimensional sensitivity of the plant $\gamma' = \gamma \frac{c_s}{\sqrt{\omega_b b}}$ and mortality $\omega'_{d0} = \omega_{d0}/\omega_b$ as control parameters. The white region corresponds to the unpopulated solution being the only stable solution. Blue regions correspond to the populated solution being stable, where dark blue correspond to the region of bistability between the populated and the unpopulated states. Yellow corresponds to pattern forming instability while pink region to oscillatory instability. These two regions are represented with semitransparent colors in order to see the superposition of both, light orange corresponds of pink and yellow. Finally in dark orange corresponds to the excitable region. Dashed black lines correspond to the values of γ' used in different bifurcation diagrams or simulations shown later. The red vertical dashed line corresponds to the condition in 5.8. The other fixed parameters are $\omega_b = 0.06 \ year^{-1}$, $a = 1.62 \ cm^2year^{-1}$, $b = 12.5 \ cm^4year^{-1}$, $d_0 = 508.1 \ cm^2year^{-1}$, $d_1 = 6560.6 \ cm^4year^{-1}$, $c_s = 75 \ \mu Mcm^2$, $\delta_s = 0.047 \ year^{-1}$, $D_s = 4.21 \cdot 10^6 \ cm^2year^{-1}$.

as well until the concentration of sulfides is low enough to allow the growth of the plant again, generating a periodic oscillation of the density.

On the other hand, the homogeneous solution can experience a Turing instability where spatial modulations appear leading to the formation of a pattern. In this case the explanation is different. Regions with higher density produce higher concentrations of sulfides than those produced by their neighbors. Due to diffusion, an effective long-range competition takes place, where those regions with higher density compete stronger than its neighborhood reducing vegetation in the surroundings. Thus, there is a feedback mechanism where regions with more vegetation can grow against those
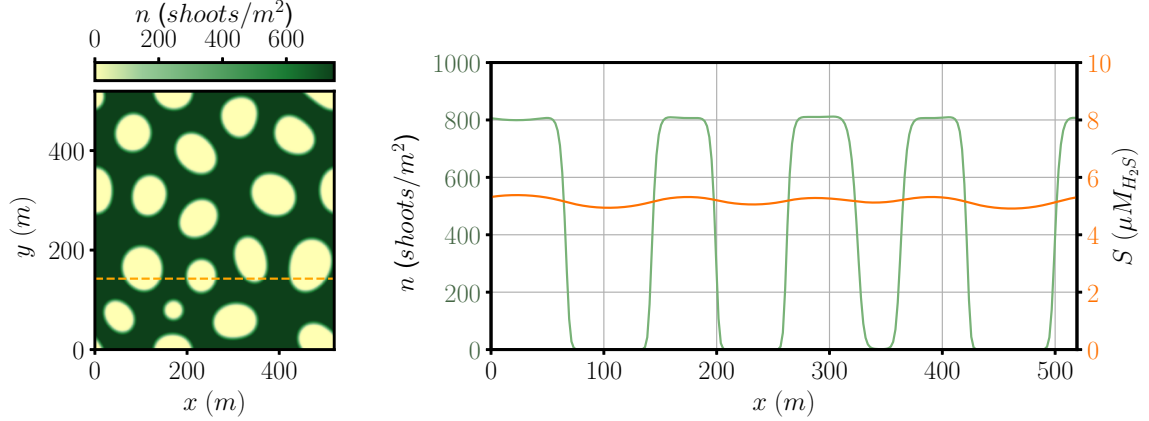
Figure 5.3: Left: Vegetation pattern from a numerical simulation starting with the homogeneous stationary solution plus noise as initial condition. The density of shoots n is represented according to the green scale on top. Right: Transversal cut of the vegetation pattern indicated in the figure on the left. Shoot density in green and associate sulfur concentration S in orange. Parameters are $\omega_b = 0.06$ $year^{-1}$, $\omega_{d0} = 0.0864$ $year^{-1}$, $a = 1.62$ $cm^2 year^{-1}$, $b = 12.5$ $cm^4 year^{-1}$, $d_0 = 508.1$ $cm^2 year^{-1}$, $d_1 = 6560.6$ $cm^4 year^{-1}$, $c_s = 75$ $\mu M cm^2$, $\gamma = 4.3 \cdot 10^{-3}$ $\mu M^{-1} year^{-1}$, $\delta_s = 0.047$ $year^{-1}$, $D_s = 4.21 \cdot 10^6$ $cm^2 year^{-1}$.

with less density, giving rise to spatial modulations, which after some time will form a regular pattern. The order of the appearance of these two instabilities can change according to the parameters, being possible to find regions of the parameter space with only oscillatory instability, with only Turing instability, or instability to oscillations and patterns at the same time. Generally, the window of instability broadens when increasing γ, being able to destabilize the homogeneous solution for all values of mortality. This broadening is not rare, since this parameter is interpreted as the sensibility of the plant to the concentration of sulfides. Given the close relationship between the strength of the competition κ from previous chapters and the parameter γ, we show the phase diagram using γ and ω_{d0} as control parameters which allows comparing with previous models including the interaction kernel (compare Fig. 5.2 with 2.4). The parameters are chosen to obtain a phase diagram where it is possible to find different instabilities together and separately as it can be seen in Fig. 5.2. Observing the line of Turing instability, we can see how the line approaches the saddle-node bifurcation when reducing γ, as in previous versions of the model. Contrary to previous versions, however, including the interaction kernel, the range of mortalities where the system is unstable broadens for high values of γ instead of closing as in 2.4. Inside the region indicated by Turing bifurcation, a homogeneous initial condition is unstable to patterns and one expects different patterns emerging from a Turing bifurcation to coexist, similarly to the ones shown in previous chap-

ters. We have performed numerical simulations to examine the patterns of negative hexagons (Fig. 5.3) and an isolated hole or localized structure (Fig. 5.4) in relation with the associated distribution of sulfide concentration in the sediment. These two cases clearly exemplify how the mechanism described by this model is able to explain the formation of regular patterns as well as circular holes of bare soil embedded in the homogeneous meadow. One interesting thing about the numerical simulations is the spatial profile of the concentration of sulfides on the sediment in relation to the shoot density. Generally, sulfides increase with the presence of vegetation, which at the end is quite reasonable since it corresponds to the place where they are produced. These profiles offer an opportunity to measure experimentally the relation between these two quantities, however, the variability of sulfide concentration is low, being at the limit of error measurement in some cases.
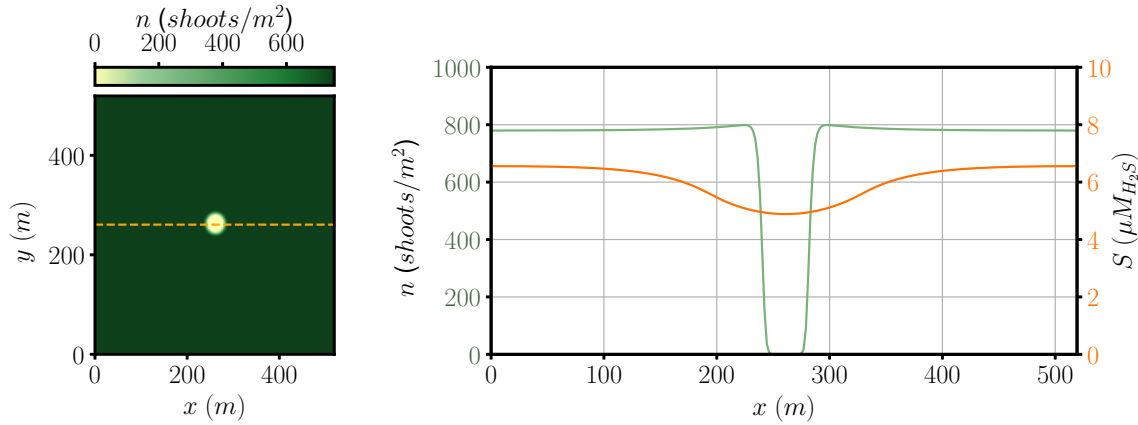
Figure 5.4: Left: Localized structure or circular hole embedded in a homogeneous meadow. Starting from a circular hole in the homogeneous meadow with a discontinuous jump in density, the evolution reaches the shown stationary profile. The density of shoots n is represented according to the greenscale on top. Right: Transverse cut of the vegetation pattern indicated in the figure on the left. Shoot density in green and associate sulfur concentration S in orange. Parameters are $\omega_b = 0.06\ year^{-1}$, $\omega_{d0} = 0.078\ year^{-1}$, $a = 1.62\ cm^2 year^{-1}$, $b = 12.5\ cm^4 year^{-1}$, $d_0 = 508.1\ cm^2 year^{-1}$, $d_1 = 6560.6\ cm^4 year^{-1}$, $c_s = 75\ \mu M cm^2$, $\gamma = 4.3{\cdot}10^{-3}\ \mu M^{-1} year^{-1}$, $\delta_s = 0.047\ year^{-1}$, $D_s = 4.21{\cdot}10^6\ cm^2 year^{-1}$.

When the region of instability to patterns overlaps with the region of oscillatory instability the dynamics become more complex [3]. An example of this regime is shown in Fig. 5.5. Starting with the homogeneous solution as initial condition, the system develops oscillations of the homogeneous solution but the limit cycle is unstable to patterns. Thus, spatial heterogeneities are amplified along the oscillations forming a pattern which stops the oscillatory dynamics. Other more complicated evolution can emerge, in particular spatiotemporal chaos or turbulence as shown in

Fig. 5.6. These regimes require more theoretical study in order to characterize their appearance.
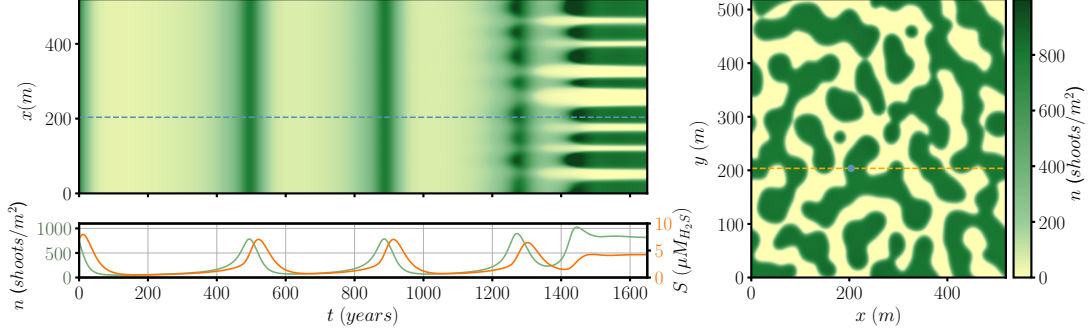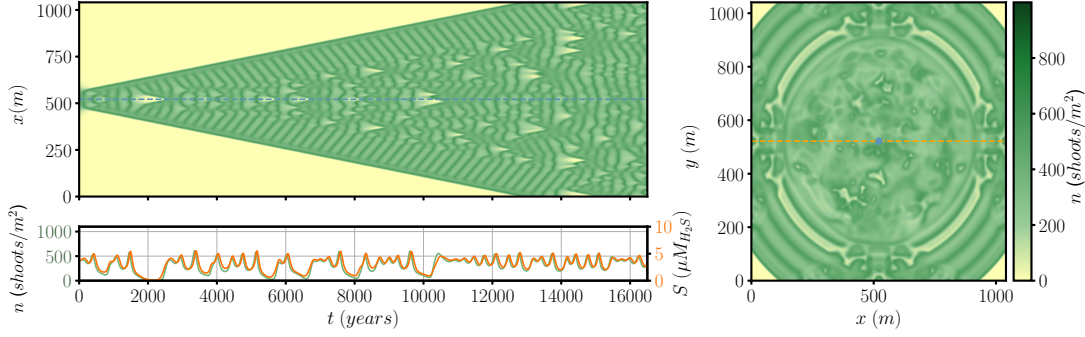

Figure 5.5: Temporal evolution in the regime simultaneously unstable to patterns and oscillations. Left-top: Temporal evolution of the shoot density of the orange cut indicated in the right panel according to its greenscale. Left-bottom: Temporal evolution of the density of shoots n in green and sulfide concentration S in orange at the position indicated by the blue dashed line on the left-top panel and the blue dot in the right panel. Right: Final shoot density in space according to the greenscale on the right. The numerical simulation starts with an homogeneous initial condition with small added noise. Parameters are $\omega_b = 0.06\ year^{-1}$, $\omega_{d0} = 0.06\ year^{-1}$, $a = 1.62\ cm^2 year^{-1}$, $b = 12.5\ cm^4 year^{-1}$, $d_0 = 508.1\ cm^2 year^{-1}$, $d_1 = 6560.6\ cm^4 year^{-1}$, $c_s = 75\ \mu M cm^2$, $\gamma = 0.0115\ \mu M^{-1} year^{-1}$, $\delta_s = 0.047\ year^{-1}$, $D_s = 4.21 \cdot 10^6\ cm^2 year^{-1}$.

5.1.2 Oscillatory dynamics

In order to characterize how the oscillatory dynamics affects the spatial dynamics it is useful to study the cycle independently from spatial coupling, so we perform numerical simulations of equations (5.1), (5.2) and (5.3) removing the spatial derivatives. Thus it is possible to see the appearance of a limit cycle just above the Hopf bifurcation when mortality is increased. For large values of γ ($\gamma' > 1$), increasing mortality the cycle grows in amplitude deforming its shape due to nonlinearity. At a certain point the amplitude of the cycle diminishes with mortality until its disappearance in a second Hopf bifurcation, which is usually very close to the saddle node, as seen in Fig. 5.7. Different time evolutions for different mortalities are shown in Fig. 5.8. The change of the amplitude and its deformation when changing mortality can be observed. The increase of the period of the oscillation is also clear.

For lower values of γ (Fig. 5.9) the behavior of the cycle changing mortality can be different. Initially the amplitude grows as previously, however, in this case the amplitude of the cycle can be large enough to collide with the unstable branch

Figure 5.6: Temporal evolution in the excitable region for small sulfide diffusion. Left-top: Temporal evolution of the shoot density of the orange cut indicated in the right panel according to its greenscale. Left-bottom: Temporal evolution of the density of shoots n in green and sulfide concentration S in orange at the position indicated by the blue dashed line on the left-top panel and the blue dot in the right panel. Right: Stationary shoot density in space according to the greenscale on the right. The numerical simulation starts with a Gaussian initial condition. Parameters are $\omega_b = 0.06 \ year^{-1}$, $\omega_{d0} = 0.069 \ year^{-1}$, $a = 1.62 \ cm^2 year^{-1}$, $b = 12.5 \ cm^4 year^{-1}$, $d_0 = 508.1 \ cm^2 year^{-1}$, $d_1 = 6560.6 \ cm^4 year^{-1}$, $c_s = 75 \ \mu M cm^2$, $\gamma = 0.0092 \ \mu M^{-1} year^{-1}$, $\delta_s = 0.047 \ year^{-1}$, $D_s = 2.86 \cdot 10^3 \ cm^2 year^{-1}$.
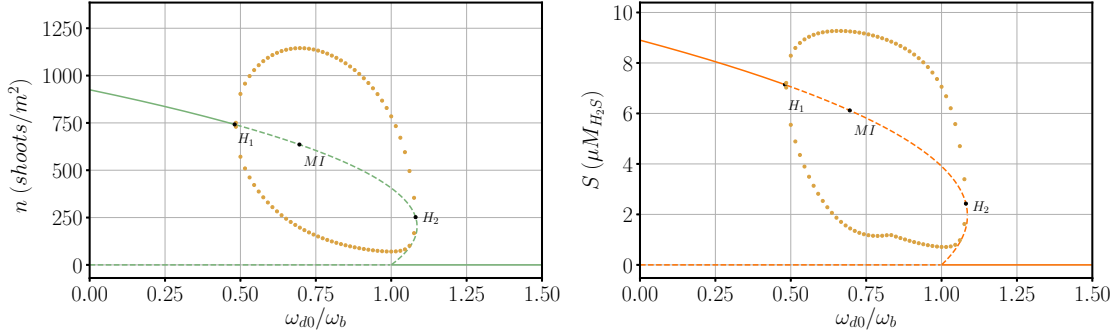
Figure 5.7: Bifurcation diagram of the homogeneous solution as a function of adimensional mortality. Left: Stationary homogeneous vegetation density in green and maximum and minimum of n on the limit cycle in yellow. Right: Stationary homogeneous sulfide concentration in orange and maximum and minimum of S on the limit cycle in yellow. Parameters are $\omega_b = 0.06 \ year^{-1}$, $a = 1.62 \ cm^2 year^{-1}$, $b = 12.5 \ cm^4 year^{-1}$, $d_0 = 508.1$ $cm^2 year^{-1}$, $d_1 = 6560.6 \ cm^4 year^{-1}$, $c_s = 75 \ \mu M cm^2$, $\gamma = 0.0115 \ \mu M^{-1} year^{-1}$, $\delta_s = 0.047$ $year^{-1}$, $D_s = 4.21 \cdot 10^6 \ cm^2 year^{-1}$. Numerical simulations of the limit cycles are performed in the system without space.

n_-^*. At this point the cycle is destroyed and for larger mortalities the cycle does not exist. This transition is called homoclinic bifurcation, a global bifurcation that changes the dynamics of the system. One of the important features is the divergence
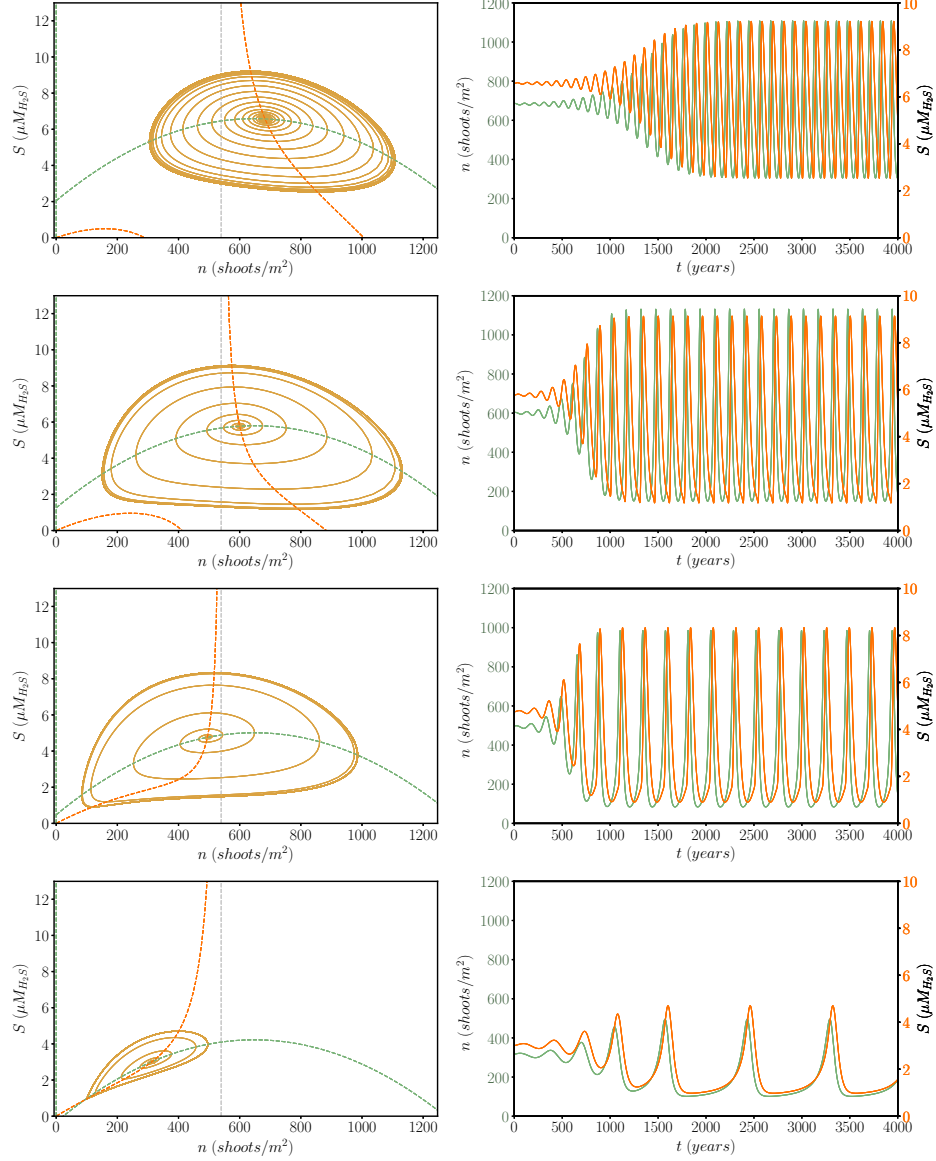
Figure 5.8: Different time evolutions of the homogeneous solutions showing the approximation to the limit cycle in the model without space. Left column represents the evolution in phase space in yellow, nullclines are represented in dashed lines in green and orange for shoots and sulfides respectively. Right column represents time evolution of shoots in green and sulfide concentration in orange. Different rows correspond to different values of mortality from top to bottom $\omega_{d0} = 0.036, 0.045, 0.055, 0.064 \ year^{-1}$. Parameters are $\omega_b = 0.06 \ year^{-1}$, $a = 1.62 \ cm^2 year^{-1}$, $b = 12.5 \ cm^4 year^{-1}$, $d_0 = 0 \ cm^2 year^{-1}$, $d_1 = 0 \ cm^4 year^{-1}$, $c_s = 75 \ \mu M cm^2$, $\gamma = 0.0115 \ \mu M^{-1} year^{-1}$, $\delta_s = 0.047 \ year^{-1}$, $D_s = 0 \ cm^2 year^{-1}$.

of the period as one approaches the homoclinic transition. Moreover, as can be seen in Fig. 5.10 the dynamics is slow for low densities close to n_-^* and accelerates with a sharp pick for high densities. When the homoclinic transition is crossed and there is no limit cycle the dynamics becomes excitable. n_-^* acts as a threshold of vegetation density. Below the threshold vegetation will decrease exponentially to zero, instead above the threshold vegetation will grow producing a lot of sulfides until a certain point in which it can not resist and vegetation will decrease to zero. In this excitable regime the final state is bare soil independently of the initial density, but if the vegetation is dense enough to overcome the threshold then the system does a large excursion before ending up in the unpopulated solution. This excitable behavior has important implications for the spatial dynamics, mainly because adding spatial coupling it makes possible that a region experiencing this excursion of growth and decay can excite its neighbors producing pulses that travel in space. Hence, determining the region bounded by the homoclinic bifurcation is very useful for the understanding of the dynamics. Nevertheless, the homoclinic bifurcation can not be characterized by linear calculation, since it is dominated by nonlinear mechanisms. It is only accessible with numerical simulations or continuation techniques. We use the first for simplicity. In Fig. 5.2 we represent the homoclinic bifurcation with an orange line. The part inside corresponds to the excitable regime. One can see that increasing mortality a homoclinic transition appears but close to the saddle node there is another homoclinic bifurcation where the cycle reappears again as it can be seen also in the bifurcation diagram in Fig. 5.9.
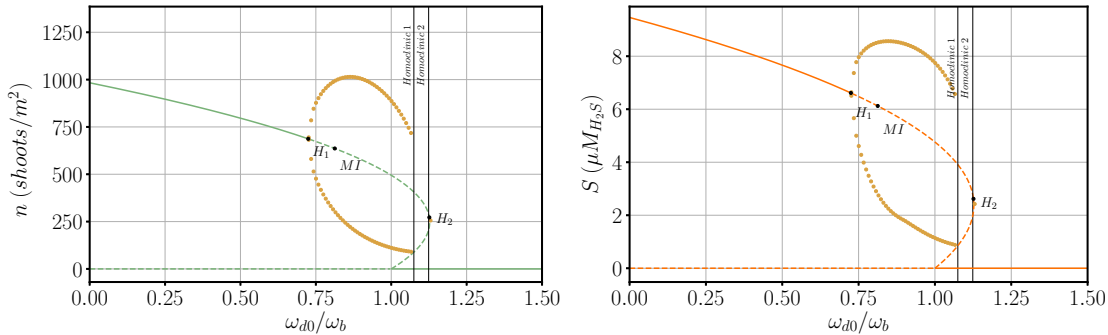
Figure 5.9: Bifurcation diagram of the model as a function of adimensional mortality showing two homoclinic bifurcations. Left: Stationary homogeneous vegetation density in green and maximum and minimum of n on the limit cycle in yellow. Right: Stationary homogeneous sulfide concentration in orange and maximum and minimum of S on the limit cycle in yellow. Parameters are $\omega_b = 0.06 \ year^{-1}$, $a = 1.62 \ cm^2year^{-1}$, $b = 12.5 \ cm^4year^{-1}$, $d_0 = 508.1 \ cm^2year^{-1}$, $d_1 = 6560.6 \ cm^4year^{-1}$, $c_s = 75 \ \mu Mcm^2$, $\gamma = 0.0103 \ \mu M^{-1}year^{-1}$, $\delta_s = 0.047 \ year^{-1}$.
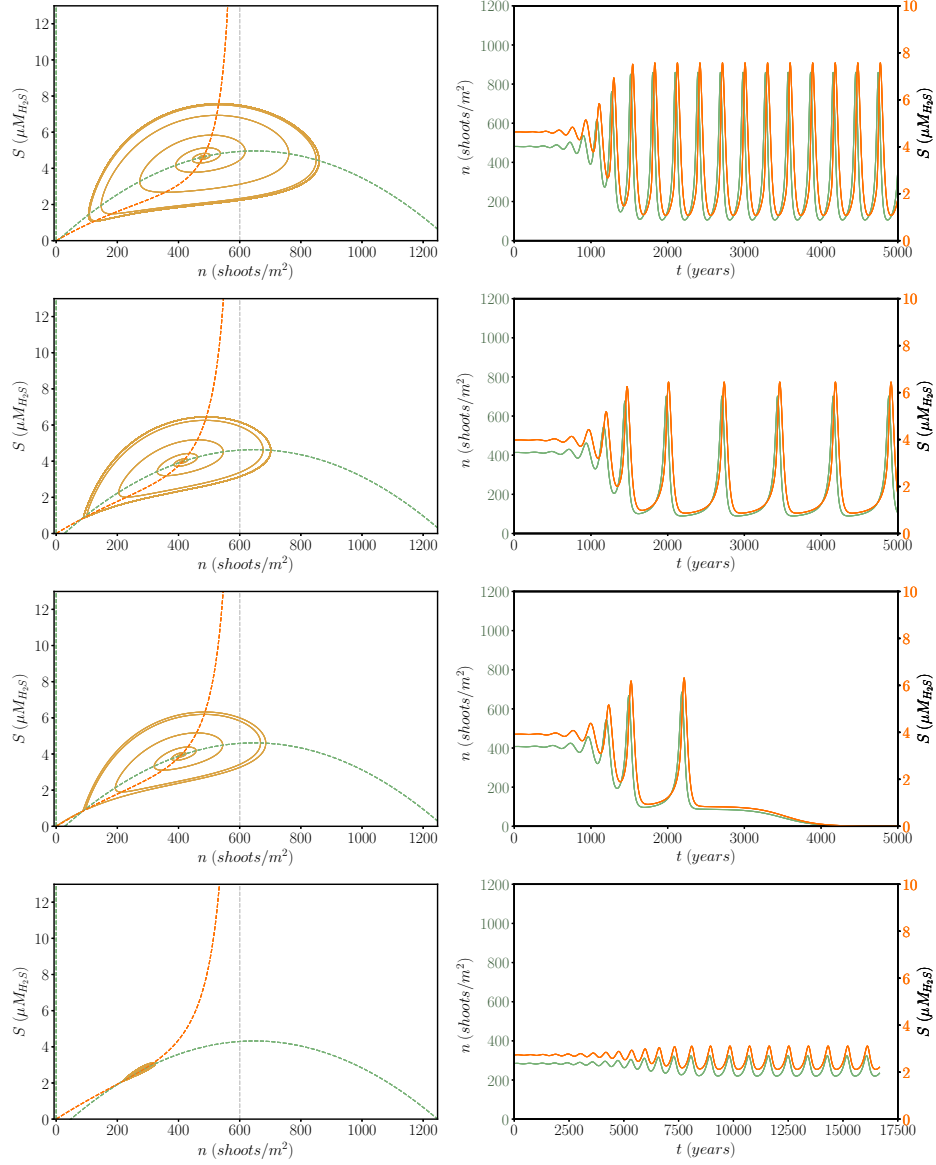
Figure 5.10: Different time evolutions of the homogeneous solutions approaching the limit cycle of the model without space and the crossing of two homoclinic bifurcations. Left column represents the evolution in phase space in yellow. Nullclines are represented in dashed lines in green and orange for shoots and sulfides respectively. Right column represents time evolution of shoots in green and sulfide concentration in orange. Different rows correspond to different values of mortality from top to bottom $\omega_{d0} = 0.0608, 0.0642, 0.0645, 0.0675$ $year^{-1}$. Parameters are $\omega_b = 0.06\ year^{-1}$, $a = 1.62\ cm^2 year^{-1}$, $b = 12.5\ cm^4 year^{-1}$, $d_0 = 0\ cm^2 year^{-1}$, $d_1 = 0\ cm^4 year^{-1}$, $c_s = 75\ \mu M cm^2$, $\gamma = 0.0103\ \mu M^{-1} year^{-1}$, $\delta_s = 0.047\ year^{-1}$, $D_s = 0\ cm^2 year^{-1}$.

The dependence on parameters of this excitable region can be difficult to characterize but one can obtain some insight using the knowledge of bifurcation theory. An homoclinic transition unfolds from a higher codimension point called Takens-Bogdanov (TB), which is a point in parameter space where the Saddle-node bifurcation and the Hopf bifurcation meet. So one can look at the linear stability analysis around the saddle-node bifurcation, Eq. (5.5). At this point one of the two eigenvalues is zero while the other changes value according to parameters. Precisely at the Takens-Bogdanov the second eigenvalue must change sign. Imposing this condition it is possible to obtain the values of γ of the Takens-Bogdanov:

$$\gamma_{TB} = \frac{\delta_s a}{2c_s\omega_b} \pm \frac{\sqrt{(\delta_s a(\delta_s + \omega_b))^2 - 8\omega_b(\delta_s + \omega_b)\delta_s^3 b}}{2c_s\omega_b(\delta_s + \omega_b)}. \tag{5.7}$$

Two Takens-Bogdanov points are created when the radicant becomes zero, or $\delta_s = \frac{-a^2\omega_b}{a^2 - 8\omega_b b}$, which emerge from $\gamma = \frac{\delta_s a}{2c_s\omega_b}$ and separate along the Saddle-node curve when the parameters are changed properly. The curve of the homoclinic transition starts in one of these two high codimension points and ends up in the other, forming a closed region in parameter space associated to the excitable region. Of course, these conditions do not fully determine the presence of an homoclinic transition since they only give us information about the point where this bifurcation emerges. However, what it is possible to determine with these conditions is, given an homoclinic bifurcation if there will exist a second homoclinic bifurcation or, on the contrary, the excitability region will reach up to the saddle node bifurcation.

One of the important advantages of this model is its simplicity, it allows to perform numerical simulations with a reasonable computational cost and obtain certain analytical results, however, it has an important disadvantage. For certain parameters the oscillatory dynamics can lead to negative sulfide concentration, which is unreasonable from the physical point of view. One can understand the source of this problem by analyzing Eq. (5.3) with $D_s = 0$, focusing in the oscillatory regime. The concentration will become negative if the right hand side of Eq. (5.3) is negative when $S = 0$, in other words, $S = 0$ represents a boundary that won't be crossed only if $\partial_t S > 0$ when $S = 0$. Thus, the sign of $\omega_d(n, 0)$ determines this behavior, which only is negative when starting with initial conditions between the two values of $n = \frac{a \pm \sqrt{a^2 - 4b\omega_{d0}}}{2}$. So in order to avoid the possibility of having trajectories in phase space that become negative the system needs to be in the range of parameters in which these values of n are not real, in other words, the range between the two values closes, which leads to

$$\omega_{d0} > \frac{a^2}{4b}. \tag{5.8}$$

Above this limit S is guaranteed to always remain positive and below this limit the system is susceptible to having trajectories crossing $S = 0$, however, even in this

case, not all trajectories become necessary negative as one can see in Fig. 5.11.
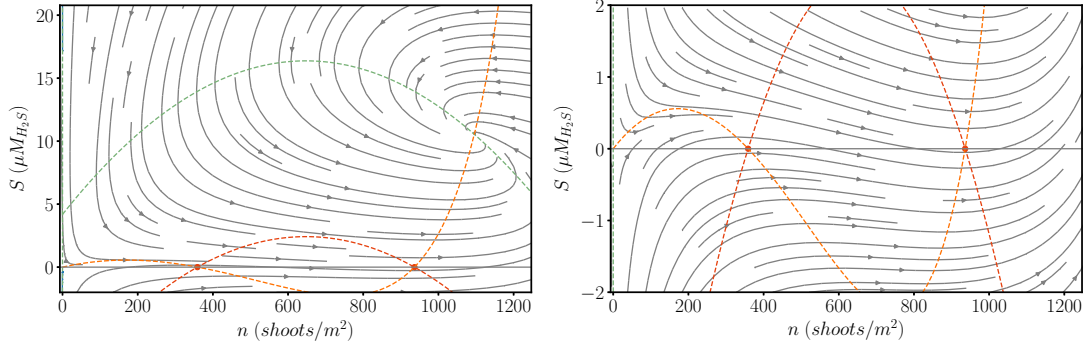
Figure 5.11: Streamplot showing the appearence of trajectories crossing $S = 0$. The nullclines are represented in green and orange for the equations of shoots and sulfides respectively and the red curve represents $\omega_d(n, 0) = 0$. The red dots represent the limits where there are trajectories crossing to the negative side. The right panel shows a detail of the left one close to $S = 0$. Parameters are $\omega_b = 0.06$ $year^{-1}$, $\omega_{d0} = 0.042$ $year^{-1}$, $a = 1.62$ $cm^2 year^{-1}$, $b = 12.5$ $cm^4 year^{-1}$, $d_0 = 0$ $cm^2 year^{-1}$, $d_1 = 0$ $cm^4 year^{-1}$, $c_s = 75$ $\mu M cm^2$, $\gamma = 4.3 \cdot 10^{-3}$ $\mu M^{-1} year^{-1}$, $\delta_s = 0.047$ $year^{-1}$, $D_s = 0$ $cm^2 year^{-1}$.

This problem of the model appears because the model is an oversimplification. Basically the mortality without sulfides $\omega_d(n, 0)$ can become negative due to the facilitative term an creating plants and removing sulfides. When one describes the evolution of only n, like in chapter 3, there is no need to distinguish between mortality and birth and $\omega_b - \omega_d(n, 0)$ accounts for the balance, however, here we include dead plants into the production of sulfides and the distinction between mortality and birth terms must be explicit, ensuring $\omega_d(n, S) > 0$. This can be easily implemented using a mortality dependence with density like in Chapter 2, however, this complicates the problem, so for now we have not included this improvement.

5.2   Parametrization for *Posidonia oceanica*

Now that we have a better understanding of the dynamics of vegetation when sulfides are included in the picture, we are going to calibrate the model using different measures for *P.oceanica*. We are going to explore the dependence of the thresholds of instability with the variability of the measures $c_s \omega_b n^*$, $\frac{c_s \omega_b}{\delta_s}$, γ and $\frac{D_s}{\delta_s}$ in order to clarify the presence or absence of the different instabilities. The values of the parameters regarding clonal growth $\omega_b = 0.06$ $year^{-1}$, $d_0 = 508.1$ $cm^2 year^{-1}$, $d_1 = 2.0$ $cm^4 year^{-1}$ are those used in previous chapters. The difference is in a and b, which are now different since we have removed the interaction kernel. Thus, we chose their

value in order to have a quantitatively similar bifurcation diagram of the homogeneous solution shown in Chapter 3. The parameter b controls the values of the stationary shoots density, while $a - \frac{\gamma c_s \omega_b}{\delta_s}$ controls the degree of bistability, therefore, $b = 12.5 cm^4 year^{-1}$ and a is determined such that $a - \frac{\gamma c_s \omega_b}{\delta_s} = 1.205\ cm^2 year^{-1}$, where γ, c_s, and δ_s are to be determined together with D_s. There are direct measures which provide $\gamma = 4.3 \cdot 10^{-3} \mu M^{-1} year^{-1}$ [135] but not of the other three. However one can use the relation between shoots and hydrogen sulfide in the sediment $S^* = \frac{c_s \omega_b}{\delta_s} n^*$ for the homogeneous stationary solution in order to determine the ratio $\frac{c_s \omega_b}{\delta_s} = 385$ $\mu M shoots^{-1} cm^2$ from the slope in Fig. 5.12. The available data does not allow to have a precise value of this quantity but at least gives an order of magnitude.
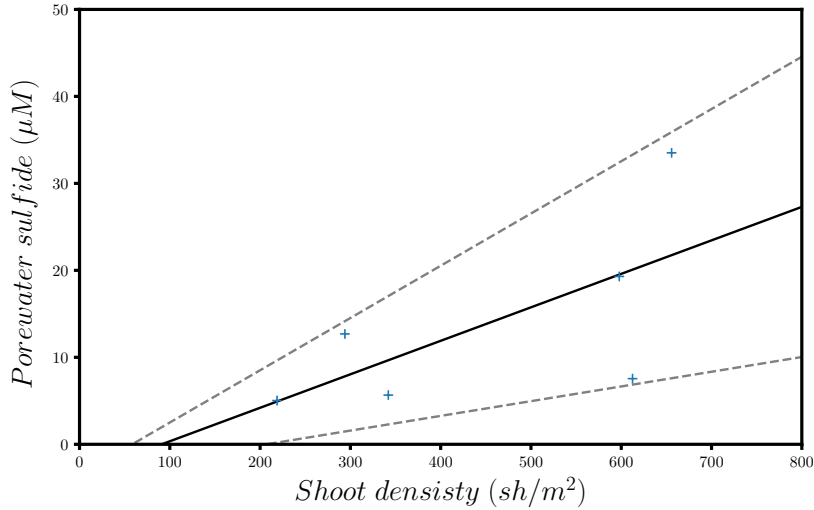
Figure 5.12: Representation of sulfide concentration as a function of vegetation density for different locations in the Balearic Island courtesy of the athours in [135]. Slope of the least square linear fit: $385.0 \pm 216.0\ \mu M shoots^{-1} cm^2$, $r = 0.666$

The value of the net production of sulfides $c_s \omega_b n$ must be a fraction of Sulfide Reduction Rate (SRR) due to reoxidation. In [134] net production is around $10^{-1} SRR$. For *Posidonia oceanica* the values of production given in [136] are quite big in comparison with stationary concentrations indicating that an important fraction being reoxidated. For example, there is a factor 10^{-3} between the concentrations of sulfates and sulfides, suggesting the net production of sulfides is much smaller than SRR. Hence, on the following we are going to consider the net production $c_s \omega_b n$ in the range $10^{-3} - 10^{-1} SRR$, from which we can obtain c_s using an average shoot density of 800 $shoots/m^2$ [94, 148] and $SRR \sim 10\ mmol/m^2/d = 3.65 \cdot 10^4\ \mu M/year$, considering the concentration below 10 cm depth is negligible [135] . We will use later different values of this range to see the effects of this variability on the results.

As a result, having an estimation of c_s and using the ratio $\frac{c_s \omega_b}{\delta_s}$ one can obtain δ_s. Finally, there are no direct measurements of D_s, however, it is possible to obtain an estimation of its value. First, from chapter 2 we know the interaction distance is $\sigma_\kappa \sim 30\ m$. The diffusion equation for sulfides gives an effective interaction with distance that we can compare with. Following this idea we can consider Eq. (5.3) being linearly dependent on the density of shoots n as an oversimplification:

$$\partial_t S = \alpha n - \delta_s S + D_s \nabla^2 S, \tag{5.9}$$

where α is an arbitrary constant determining the value of sulfides production. The solution $\tilde{S}(q,t)$ can be obtained exactly in Fourier space as

$$\tilde{S}(q,t) = e^{-(\delta_s + D_s q^2)t} \left(S_0 + \alpha \tilde{n}(q,t) \frac{e^{(\delta_s + D_s q^2)t} - 1}{\delta_s + D_s q^2} \right). \tag{5.10}$$

Considering the initial concentration $S_0 = 0$ and the limit in which δ_s and D_s are large, which corresponds to the sulfide concentration reaching its stationary state faster than the evolution of vegetation, the exponential term can be neglected and the sulfide concentration can be written in terms of the convolution of an interaction kernel $\mathcal{K}(x)$ and the density of vegetation n.

$$S(\vec{x}, t) = \iint_{-\infty}^{\infty} \mathcal{K}(\vec{x} - \vec{x}')n(\vec{x}', t)d\vec{x}', \tag{5.11}$$

where the kernel is the inverse Fourier transform of the Lorentzian $\frac{\alpha}{\delta_s + D_s q^2}$. In the one dimensional case the kernel correspond to an exponential kernel $\frac{\alpha}{2\sqrt{D_s \delta_s}} e^{-\sqrt{\frac{\delta_s}{D_s}}\|x\|}$, while in two dimensions the kernel is given in terms of the modified Bessel function of second kind $\frac{\alpha}{2\pi D_s} K_0(\sqrt{\frac{\delta_s}{D_s}}\|x\|)$. In both cases the kernel corresponds to decaying functions where the scale of the interaction is given by $\sqrt{\frac{D_s}{\delta_s}}$. Thus, imposing this interaction length must be $\sim 30\ m$ the parameter D_s can be obtained.

Alternatively it is possible to obtain this characteristic length using measurements of organic matter spreading due to fish farm activity. Considering the production $\alpha \delta(\vec{x})$ instead of $\alpha n(\vec{x}, t)$ we can use Eq. (5.11) and obtain the stationary distribution of sulfides with distance for constant production in a given position, which is basically the expression given by the kernel. The variability of these measurements in [144–147] is large, $\sqrt{\frac{D_s}{\delta_s}} = 5 - 200\ m$, which is compatible with the interaction length considered above.

The precision of these values is clearly low, giving just an order of magnitude. Hence different results can be obtained within the range of possible values. From this perspective we aim to quantify how the results depend on the values we choose

for the quantities γ, c_s, $\frac{c_s \omega_b}{\delta_s}$, $\sqrt{\frac{D_s}{\delta_s}}$. Initially we consider $\gamma = 4.3 \cdot 10^{-3} \mu M^{-1} year^{-1}$, $c_s = 7.6 \cdot 10^3 \ \mu M cm^2$, $\delta_s = 1.18 \ year^{-1}$ and $D_s = 1.07 \cdot 10^7 \ cm^2 year^{-1}$ as the reference set of parameters, which corresponds to taking $c_s \omega_b n = 10^{-3} SRR$, $\frac{c_s \omega_b}{\delta_s} = 385$ $\mu M shoots^{-1} cm^2$, $\sqrt{\frac{D_s}{\delta_s}} = 30 \ m$. We consider the production of sulfides a small fraction of sulfate reduction rate $c_s \omega_b n = 10^{-3} SRR$ for two reasons. First it does not seem plausible that a concentration of sulfides $\sim 10 \mu M$ is produced by a $SRR = 3.65 \cdot 10^4 \ \mu M / year$. The net production considering reduction and oxidation process should be smaller than SRR. The second reason is based on the fact that, taking the correction fraction $10^{-3} SRR$, the resultant removal rate of sulfides is comparable to the one we obtain from temporal evolution of the concentration of sulfides in meadows of *Zostera marina*, which gives a temporal scale of removal of the order of months to one year. Next, we will change the factor 10^{-3} to see the consequences. Thus, we are going to use the phase diagram (Fig. 5.13) to characterize this dependence with the variability of the parameters changing one keeping the others fixed.

For the reference set of parameters we can see the changes in the phase diagram in Fig. 5.13 with respect to Fig. 5.2. There are no significant changes in the qualitative shape of the phase diagram with this set of parameters, however the values of the parameters have changed significantly, being γ the most affected. There is not a qualitative change of the Turing instability as compared to the previous results, where the critical wavelength was $\sim 30m$. The big difference is in the Hopf bifurcation, which extends much further in mortality and for lower values of γ. As a result, the Hopf bifurcation touches the Saddle node bifurcation at two Takens-Bogdanov codimension-2 points. Hence, the presence of the two TB's indicates the existence of an excitable region. However, almost all this region is susceptible to develop negative densities.

All the following cases present the same problem. The oscillatory regions are susceptible to become negative. Only regions with patterns are guaranteed to remain positive.

The first parameter used for the calibration that we are going to change is γ. We are going to consider changes according to error measurement in [135] $\gamma = 4.3 \pm 1.4 \cdot 10^{-3} \mu M^{-1} year^{-1}$. We show the phase diagrams for the two cases in Fig 5.14. The most important effect is the presence of the two TB points. For bigger values of the calibration parameter the Hopf bifurcation moves slightly to higher mortality expanding the distance between the TB points, on the contrary decreasing its value the Hopf bifurcation moves to lower mortalities, not intersecting with the saddle node. The Turing bifurcation moves down increasing the parameter without experiencing important qualitative changes. The critical wavelength is barely affected when increasing γ, while for $\gamma = 5.7 \cdot 10^{-3} \ \mu M^{-1} year^{-1}$ the critical wavelength moves
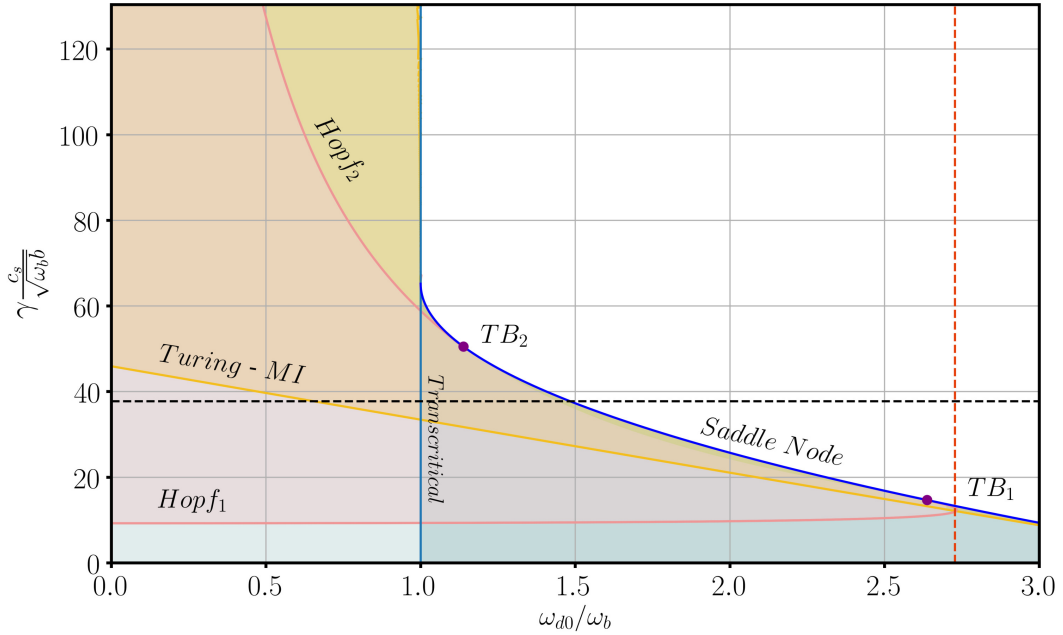
Figure 5.13: Same as in Fig. 5.2 for $a = 2.86\ cm^2 year^{-1}$, $c_s = 7.6 \cdot 10^3\ \mu M cm^2$, $\delta_s = 1.18\ year^{-1}$, $D_s = 1.07 \cdot 10^7\ cm^2 year^{-1}$.

to $\sim 20\ m$.

Second, we change the factor of sulfate reduction rate, considered as net sulfide production as explained previously, using $10^{-2}SRR$ and $10^{-1}SRR$ respectively. Comparing with the reference set of parameters in Fig. 5.13, where we take $10^{-1}SRR$, the phase diagrams of the three cases are qualitatively equivalent (Figs. 5.13 and 5.15). Essentially, there is a scaling factor between axis of the phase diagrams of the three cases being the regions of coexistence not affected. Neither the wavelength varies significantly, changing to $\sim 20\ m$ for both cases ($10^{-2}SRR$ and $10^{-1}SRR$). The important changes occur on the parameters c_s, δ_s and D_s, which basically increase proportionally to the considered factor. The interpretation is simple, increasing the production of sulfides, in order to maintain the same stationary concentration controlled by $S^* = \frac{c_s \omega_b}{\delta_s} n^*$, the rate of removal must increase proportionally. As a result, the diffusion must increase in the same way to maintain the interaction distance given by $\sqrt{\frac{D_s}{\delta_s}}$, in other words since the removal rate increases the sulfides must diffuse faster to preserve the wavelength of the pattern. The problem is the removal rate and diffusion reach values which are unreasonable. There is a substantial change in the temporal scale of sulfides given by the inverse of δ_s, from ten months, to one month, to 3 days, and the distance of spreading due to diffusion changes from 30 $m/year$, to 100 $m/year$, to 300 $m/year$.
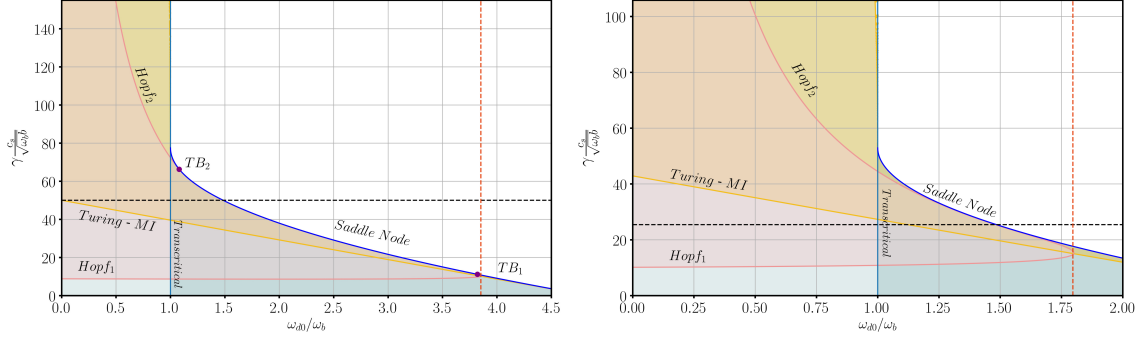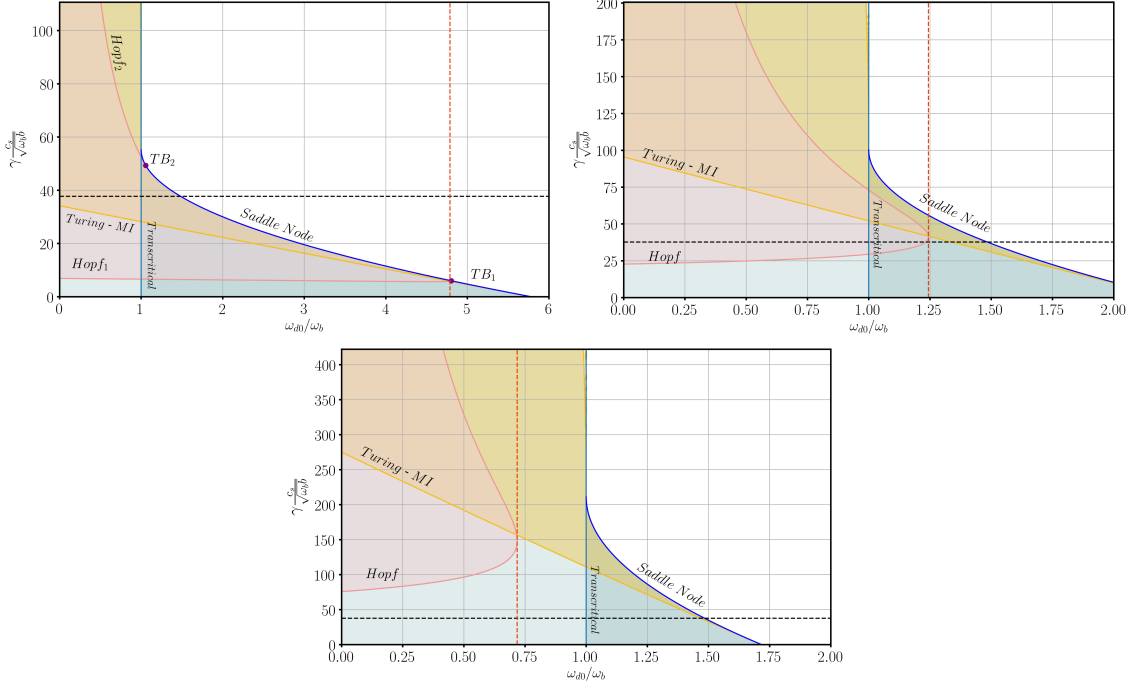
Figure 5.14: Same as in Fig. 5.2. Parameters of left panel changing the calibration value to $\gamma = 5.7 \cdot 10^{-3}\ \mu M^{-1}year^{-1}$ are $a = 3.4\ cm^2year^{-1}$, $c_s = 7.6 \cdot 10^3\ \mu Mcm^2$, $\delta_s = 1.18\ year^{-1}$, $D_s = 1.07 \cdot 10^7\ cm^2year^{-1}$. Parameters of right panel changing the calibration value to $\gamma = 2.9 \cdot 10^{-3}\ \mu M^{-1}year^{-1}$ are $a = 2.32\ cm^2year^{-1}$, $c_s = 7.6 \cdot 10^3\ \mu Mcm^2$, $\delta_s = 1.18\ year^{-1}$, $D_s = 1.07 \cdot 10^7\ cm^2year^{-1}$.
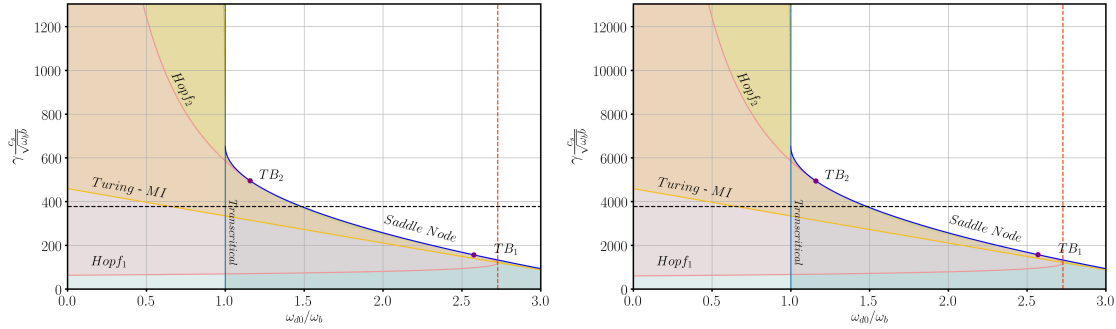
Figure 5.15: Same as in Fig. 5.2. Parameters of the left panel changing to $c_s\omega_b n = 10^{-2}SRR$ are $a = 2.86\ cm^2year^{-1}$, $c_s = 7.6 \cdot 10^4\ \mu Mcm^2$, $\delta_s = 11.84\ year^{-1}$, $D_s = 1.07 \cdot 10^8\ cm^2year^{-1}$. Parameters of the right panel changing to $c_s\omega_b n = 10^{-1}SRR$ are $a = 2.86\ cm^2year^{-1}$, $c_s = 7.6 \cdot 10^5\ \mu Mcm^2$, $\delta_s = 118.44\ year^{-1}$, $D_s = 1.07 \cdot 10^9\ cm^2year^{-1}$.

Third, we change the ratio $\frac{c_s\omega_b}{\delta_s} = 385 \pm 216\ \mu M shoots^{-1}cm^2$ within its error (Fig. 5.12). We also take $\frac{c_s\omega_b}{\delta_s} = 61\ \mu M shoots^{-1}cm^2$ where the effects of changing the previous ratio are more pronounced to better see the changes of the phase diagram. This ratio corresponds to the relation between the stationary concentration of sulfides and the shoot density. This case has important implications from the dynamical point of view, mainly because this ratio controls the level of superposition between the unstable regions to patterns and to oscillations. As one can see in Fig. 5.16 increasing this ratio the oscillatory domain touches the saddle node creating the two TB points as previously. On the contrary, decreasing the ratio, the oscillatory domain moves to lower mortalities, generating regions with only oscillatory instability, regions with

only Turing instability, and regions with the two instabilities simultaneously. The wavelength of the pattern increases when decreasing the ratio reaching $\sim 50\ m$ for the lowest value considered. Interestingly the ratio $\frac{c_s \omega_b}{\delta_s} = \frac{S^*}{n^*}$ has an important impact on the dynamical behaviors present in the phase diagram, which is an important fact from the diagnostic point of view.

Figure 5.16: Same as in Fig. 5.2. Parameters of left panel changing to $\frac{c_s \omega_b}{\delta_s} = 601$ $\mu M shoots^{-1} cm^2$ are $a = 3.79\ cm^2 year^{-1}$, $c_s = 7.6 \cdot 10^3\ \mu M cm^2$, $\delta_s = 0.76\ year^{-1}$, $D_s = 6.83 \cdot 10^6\ cm^2 year^{-1}$. Parameters of the right panel changing to $\frac{c_s \omega_b}{\delta_s} = 169\ \mu M shoots^{-1} cm^2$ are $a = 1.93\ cm^2 year^{-1}$, $c_s = 7.6 \cdot 10^3\ \mu M cm^2$, $\delta_s = 2.70\ year^{-1}$, $D_s = 2.43 \cdot 10^7$ $cm^2 year^{-1}$. Parameters of the bottom panel changing to $\frac{c_s \omega_b}{\delta_s} = 61\ \mu M shoots^{-1} cm^2$ are $a = 1.47\ cm^2 year^{-1}$, $c_s = 7.6 \cdot 10^3\ \mu M cm^2$, $\delta_s = 7.48\ year^{-1}$, $D_s = 6.73 \cdot 10^7\ cm^2 year^{-1}$.

Finally, we change the quantity $\sqrt{\frac{D_s}{\delta_s}}$ to 5 and 100 m. As expected for the lower value the domain of instability to patterns diminishes starting to resemble the shape found in previous chapters for the model with kernel 2.4, besides the oscillatory domain is not affected. Is not surprising that the wavelength of the pattern changes accordingly to $\sqrt{\frac{D_s}{\delta_s}}$ being $\sim 10\ m$ and $\sim 50\ m$ respectively.

As said previously all previous parameterizations are susceptible to develop negative values of S, which is a problem because impose limitations to the model for studying *P.oceanica*. We do not expect the results to change significantly changing
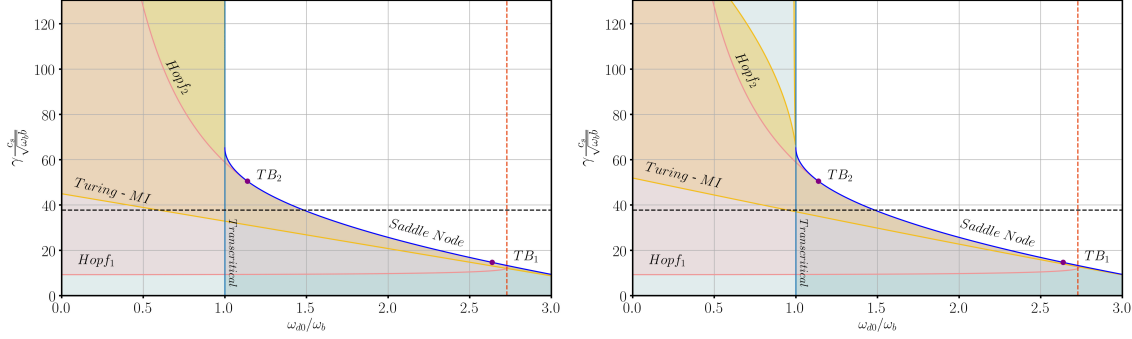
Figure 5.17: Same as in Fig. 5.2. Parameters are $a = 2.86\ cm^2 year^{-1}$, $c_s = 7.6 \cdot 10^3$ $\mu M cm^2$, $\delta_s = 1.18\ year^{-1}$, $D_s = 1.18 \cdot 10^8\ cm^2 year^{-1}$ for the left panel and $D_s = 2.96 \cdot 10^5$ $cm^2 year^{-1}$ for the right panel taking $\sqrt{\frac{D_s}{\delta_s}} = 100$ and $5\ m$ respectively.

the mortality term $\omega_d(n, S)$ to prevent negative values as done in chapter 1. As we have seen, the relation of the unstable regions with parameters is complex, however, the region unstable to patterns exist for a broad range of values of γ. This fact is important because variable conditions found in nature like the increase in mortality approaching the coast will explore the phase diagram making reasonably probable observing pattern formation. The same can be applied to the excitable region, although being more limited, there is an important range of values of γ in which the natural exploration of mortality will make the plants exhibit excitable behavior in some locations. In fact, it seems to be the case, vegetation patterns are more easily found in nature while excitable dynamics is rare. However, in the Corsican coast the evolution of a ring of vegetation compatible with excitable behavior was reported in [58]. We expect to be able to reproduce such behavior with numerical simulations in the excitable region when including the saturation of the facilitative term, which avoids the appearance of negative values of sulfide concentration.

5.3 Parametrization for *Zostera marina*

Similar to the formation of rings in the Corsican coast for *P. oceanica*, rings of vegetation were found in the Danish Kattegat. In this work measurements of porewater sulfides were taken along the radial direction of the ring, showing a correlation between the presence of sulfides in the sediment and the lack of vegetation. We aim to calibrate the model for these seagrass species in order to show the possibility of the formation of rings due to the presence of the excitable region in the phase diagram. Equivalently to the case of *P. oceanica* it is possible to calibrate the model using the same procedure as before. From [94] we take the branching rate ω_b, the branching

angle ϕ_b and the elongation velocity of the rhizome ν. Using the previous values and according to chapter 3, we compute $d_0 = 232.67\ cm^2year^{-1}$ and $d_1 = 1164.57$ cm^4year^{-1}. The parameter a is calculated to have the same degree of bistability while b is calculated to have around 1000 $shoots/m^2$ for the homogeneous density at mortality $\omega_{d0}/\omega_b = 1.273$. Regarding the parameters of sulfide evolution γ, c_s, δ_s and D_s, there are no systematic measurements of γ, however, we can obtain an estimation using measurements of sulfide concentration and mortality. From [149] $\gamma = 2.92 \cdot 10^{-2}\ \mu M^{-1}year^{-1}$ while in [150] $\gamma = 2.58 \cdot 10^{-3}\ \mu M^{-1}year^{-1}$. We also obtain the value of $\frac{c_s\omega_b}{\delta_s} = 2847.46\ \mu M shoots^{-1}cm^2$ from density measurements and sulfide concentrations in [137], and $\frac{c_s\omega_b}{\delta_s} = 1347.55\ \mu M shoots^{-1}cm^2$ from [56]. The removal rate can be estimated from the time evolution of sulfide concentration in Fig. 2 of [137]. The maximum production of sulfides is in summer and after that there is a decay of the concentration with time, being the time of removal between half year and a year, hence we take $\delta_s = 1 - 2\ years^{-1}$. The removal rate can be computed using the same procedure used for $P.Oceainca$, however one needs to consider the production of sulfides a fraction of SRR. In this case we can compare the resultant δ_s using both ways, and there is agreement when the fraction is between $10^{-4} - 10^{-3}SRR$. Finally the diffusion parameter is considered the same as in the previous case due to the lack of measurements in the Danish Kattegat.

We use the following parameters in the calibration, $\gamma = 8.315 \cdot 10^{-3}\ \mu M^{-1}year^{-1}$, $\frac{c_s\omega_b}{\delta_s} = 2 \cdot 10^3\ \mu M shoots^{-1}cm^2$, $\delta_s = 1.2\ years^{-1}$ as a reference, which are in the ranges determined by the values presented before and allow the formation of rings as we will show below. Next, we are going to change the parameters in order to study how the phase diagram changes for different values used in the calibration as in the previous section. But first, we analyze the phase diagram for this set of values. Basically, instabilities to patterns and oscillations are present. The two regions of instability are superimposed and are present for the chosen value of γ (Fig. 5.18). The two Hopf bifurcations touch the saddle node at two Takens-Bogdanov creating a region of excitability. As one can see the region where the sulfide concentration is guaranteed to be positive is limited but not inexistent like previously. The critical wavelength of the pattern is around $15m$.

The first parameter used in the calibration we change is δ_s to 1 and 2 $year^{-1}$ showing its phase diagrams in Fig. 5.19. The oscillatory region moves creating a broader excitable region in the first case and a smaller one in the second. Other changes are minor, even in the critical wavelength.

Second, we change the ratio $\frac{c_s\omega_b}{\delta_s}$ to 2847.46 $\mu M shoots^{-1}cm^2$ and 1347.55 $\mu M shoots^{-1}cm^2$. In Fig. 5.20 we can see in the first case that the saddle node bifurcation moves to higher mortalities and the two TB separate creating a bigger excitable region, however a big part of this region is susceptible to develop negative concentrations. In the second case, the excitable region is smaller but this limit is on top on the transcritical
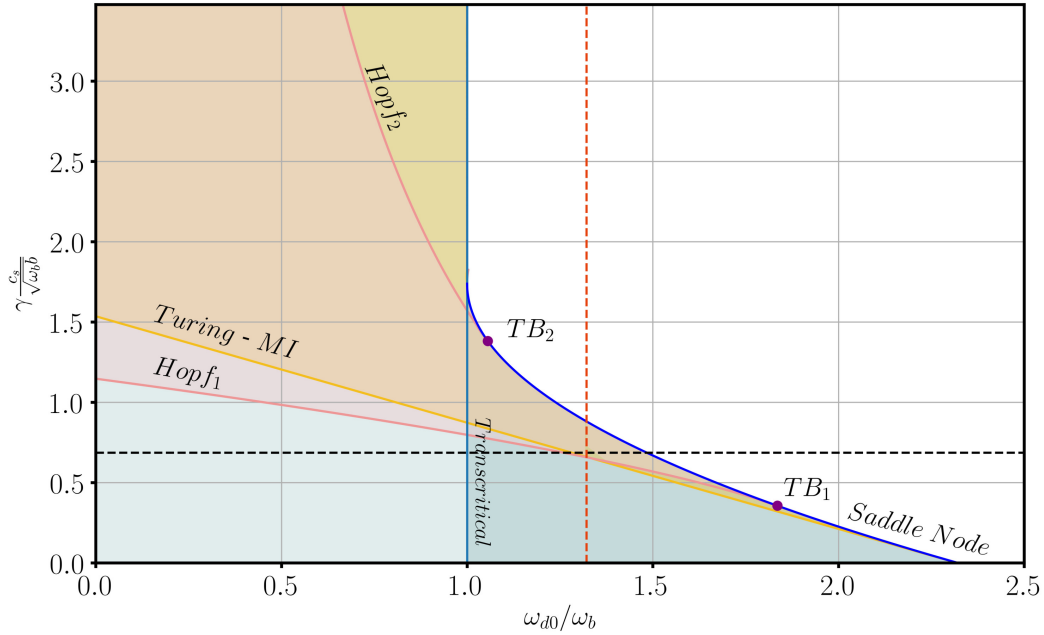
Figure 5.18: Same as in Fig. 5.2. Parameters are $\omega_b = 1.587\ year^{-1}$, $a = 42.13\ cm^2year^{-1}$, $b = 211.6\ cm^4year^{-1}$, $d_0 = 232.67\ cm^2year^{-1}$, $d_1 = 1164.57\ cm^4year^{-1}$, $c_s = 1512.29\ \mu Mcm^2$, $\delta_s = 1.2\ year^{-1}$, $D_s = 1.08 \cdot 10^7\ cm^2year^{-1}$.
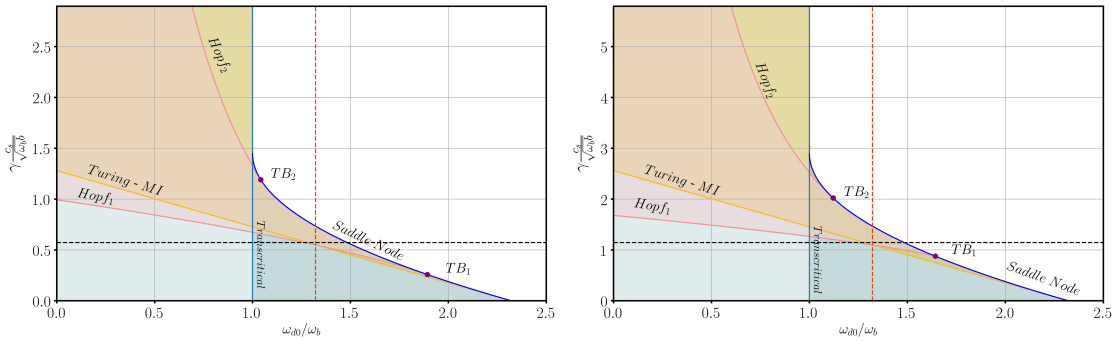
Figure 5.19: Parameters are $\omega_b = 1.587\ year^{-1}$, $a = 42.13\ cm^2year^{-1}$, $b = 211.6\ cm^4year^{-1}$, $d_0 = 232.67\ cm^2year^{-1}$, $d_1 = 1164.57\ cm^4year^{-1}$, $c_s = 1260.24\ \mu Mcm^2$, $\delta_s = 1\ year^{-1}$, $D_s = 9.0 \cdot 10^6\ cm^2year^{-1}$. Parameters are $\omega_b = 1.587\ year^{-1}$, $a = 42.13\ cm^2year^{-1}$, $b = 211.6\ cm^4year^{-1}$, $d_0 = 232.67\ cm^2year^{-1}$, $d_1 = 1164.57\ cm^4year^{-1}$, $c_s = 2520.48\ \mu Mcm^2$, $\delta_s = 2\ year^{-1}$, $D_s = 1.8 \cdot 10^7\ cm^2year^{-1}$.

bifurcation, leaving a broader safe region. In the first case the wavelength changes to around 10 m while in the second remains around 15 m

In the third case, represented in Fig. 5.21, we show a similar dependence changing
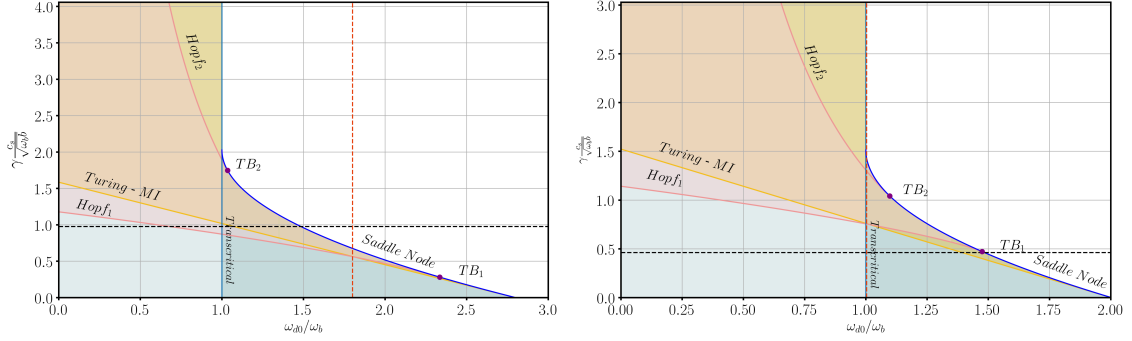
Figure 5.20: Parameters with calibration parameter $\frac{c_s \omega_b}{\delta_s} = 2847.46 \ \mu M shoots^{-1} cm^2$ are $\omega_b = 1.587 \ year^{-1}$, $a = 49.18 \ cm^2 year^{-1}$, $b = 211.6 \ cm^4 year^{-1}$, $d_0 = 232.67 \ cm^2 year^{-1}$, $d_1 = 1164.57 \ cm^4 year^{-1}$, $c_s = 2153.1 \ \mu M cm^2$, $\delta_s = 1.2 \ year^{-1}$, $D_s = 1.08 \cdot 10^7 \ cm^2 year^{-1}$. Parameters with calibration parameter $\frac{c_s \omega_b}{\delta_s} = 1347.55 \ \mu M shoots^{-1} cm^2$ are $\omega_b = 1.587 \ year^{-1}$, $a = 36.7 \ cm^2 year^{-1}$, $b = 211.6 \ cm^4 year^{-1}$, $d_0 = 232.67 \ cm^2 year^{-1}$, $d_1 = 1164.57 \ cm^4 year^{-1}$, $c_s = 1018.94 \ \mu M cm^2$, $\delta_s = 1.2 \ year^{-1}$, $D_s = 1.08 \cdot 10^7 \ cm^2 year^{-1}$.

the value of γ used in the calibration to $\gamma = 2.92 \cdot 10^{-2} \ \mu M^{-1} year^{-1}$ and $\gamma = 2.58 \cdot 10^{-3} \ \mu M^{-1} year^{-1}$. For the first value, the distance between the two TB points increases dramatically but all the region becomes susceptible to develop negative concentrations. On the second case this limit moves in mortality as well as the Hopf bifurcation, which in this case does not meet the saddle node. This similar change of the phase diagram when increasing the values of $\frac{c_s \omega_b}{\delta_s}$ and γ used for the calibration (compare Fig. 5.20 and 5.21) is basically due to the movement of the saddle node bifurcation.

One can see from the previous cases, that for these parameter ranges the excitable region appears easily, however, the problem is that in many cases the excitable region coincides with the region susceptible of developing negative sulfide concentrations. If one performs numerical simulations with these parameter sets one can see the formation of rings with negative sulfide concentration in the front, which is physically unreasonable. However, the initially chosen parameter values have regions in the phase diagram where one can ensure positive concentration and being inside the excitable region. Additionally, there is one more requirement for a ring to be formed. The diffusion of sulfides must not exceed the diffusion of plants in order to maintain the front of vegetation and sulfide concentration one in front of the other. Thus we show that for much smaller diffusions than those giving patterns, $D_s = 214.95 \ cm^2 year^{-1}$, one can find expanding rings of vegetation. In Fig. 5.22 we show the phase diagram with this value of diffusion. As we can see the Turing instability is not present. For higher values of D_s on can recover gradually this instability, but the ring is influenced by this fact developing much more complex structures in space.
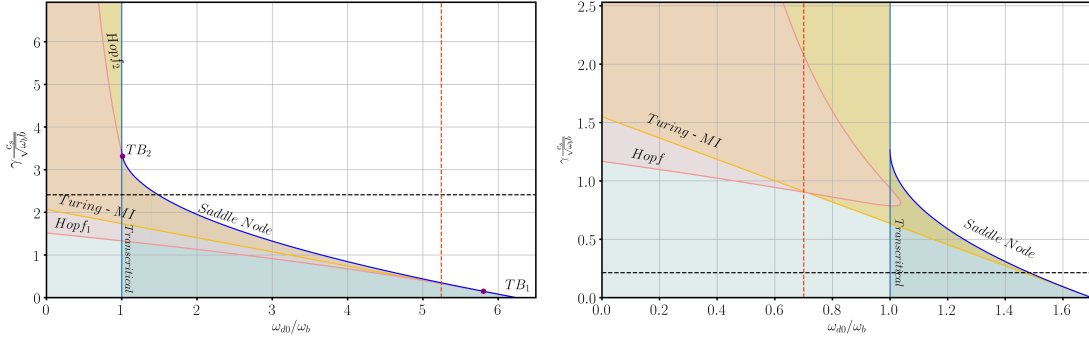
Figure 5.21: Parameters with calibration parameter $\gamma = 2.92 \cdot 10^{-2}$ $\mu M^{-1} year^{-1}$ are $\omega_b = 1.587$ $year^{-1}$, $a = 83.94$ $cm^2 year^{-1}$, $b = 211.6$ $cm^4 year^{-1}$, $d_0 = 232.67$ $cm^2 year^{-1}$, $d_1 = 1164.57$ $cm^4 year^{-1}$, $c_s = 1512.29$ $\mu M cm^2$, $\delta_s = 1.2$ $year^{-1}$, $D_s = 1.08 \cdot 10^7$ $cm^2 year^{-1}$. Parameters with calibration parameter $\gamma = 2.58 \cdot 10^{-3}$ $\mu M^{-1} year^{-1}$ are $\omega_b = 1.587$ $year^{-1}$, $a = 30.68$ $cm^2 year^{-1}$, $b = 211.6$ $cm^4 year^{-1}$, $d_0 = 232.67$ $cm^2 year^{-1}$, $d_1 = 1164.57$ $cm^4 year^{-1}$, $c_s = 1512.29$ $\mu M cm^2$, $\delta_s = 1.2$ $year^{-1}$, $D_s = 1.08 \cdot 10^7$ $cm^2 year^{-1}$.
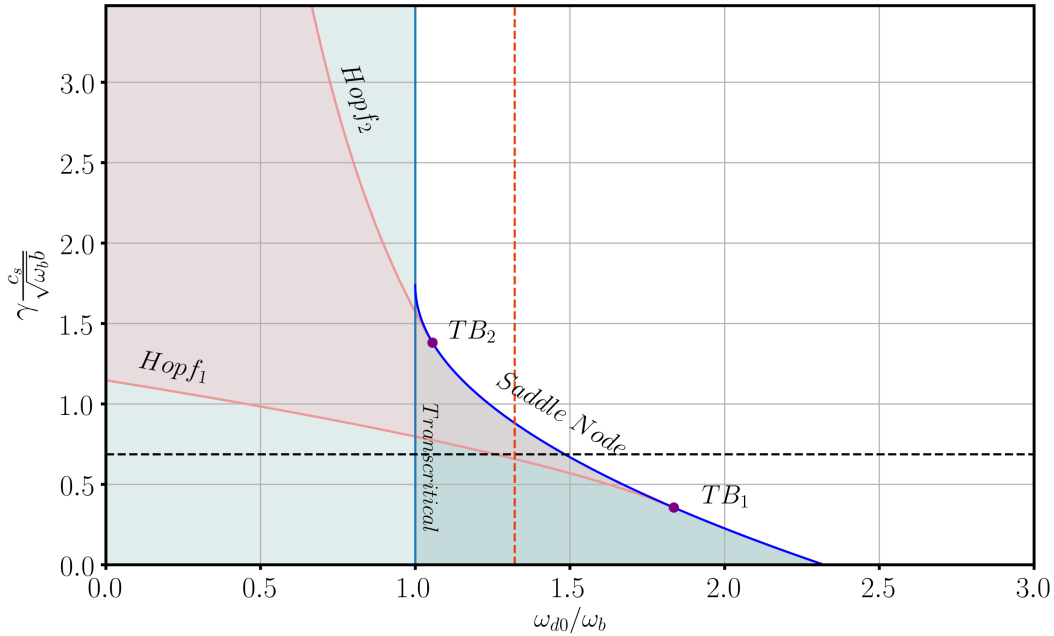
Figure 5.22: Parameters are $\omega_b = 1.587$ $year^{-1}$, $a = 42.13$ $cm^2 year^{-1}$, $b = 211.6$ $cm^4 year^{-1}$, $d_0 = 232.67$ $cm^2 year^{-1}$, $d_1 = 1164.57$ $cm^4 year^{-1}$, $c_s = 1512.29$ $\mu M cm^2$, $\delta_s = 1.2$ $year^{-1}$, $D_s = 214.95$ $cm^2 year^{-1}$.

Fig. 5.23 shows the time evolution of a ring of vegetation that expands. Starting with an initial condition of a Gaussian spot of vegetation, the accumulation of sulfides
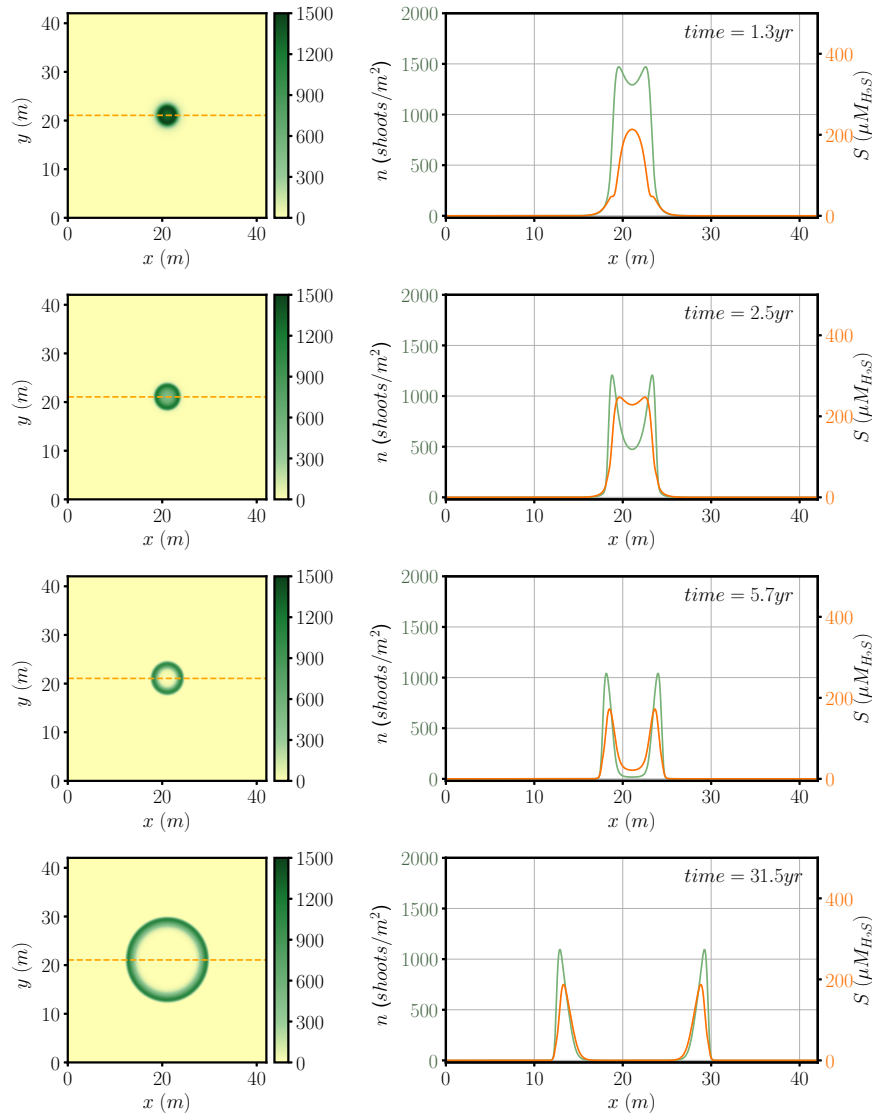
Figure 5.23: Spatiotemporal evolution of an expanding ring of vegetation. Left: Vegetation distribution of a numerical simulation starting with a Gaussian spot of vegetation as initial condition. The density of shoots n is represented according to the right greenscale. Right: Transversal cut of the vegetation pattern indicated in the figure on the left. Shoot density in green and associate sulfur concentration S in orange. Parameters are $\omega_b = 1.587$ $year^{-1}$, $\omega_{d0} = 2.301$ $year^{-1}$, $a = 42.13$ cm^2year^{-1}, $b = 211.6$ cm^4year^{-1}, $d_0 = 232.67$ cm^2year^{-1}, $d_1 = 1164.57$ cm^4year^{-1}, $c_s = 1512.29$ μMcm^2, $\delta_s = 1.2$ $year^{-1}$, $D_s = 214.95$ cm^2year^{-1}.

opens a hole in the center poisoning the vegetation, thus once the ring is formed it

increases its size with time remaining the circular band of vegetation with the same width. Vegetation is fast enough to grow escaping the diffusion of sulfides which remain just behind killing all left plants, thus forming an excitable pulse, which grows indefinitely until colliding with another pulse. The formation of this expanding ring and the sulfide concentration behind resembles those fairy rings reported in the Danish Kattegat for *Zostera marina* [56], (Fig. 5.24).
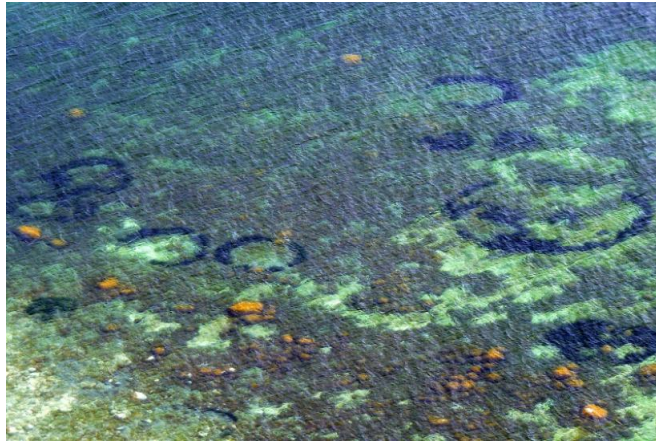
Figure 5.24: Fairy rings of *Zostera marina* in the Danish Kattegat. Image from [56]

5.4 Conclusions

The model presented in this chapter helps in the understanding of the mechanism involved in the formation of patterns of vegetation in marine ecosystems. It explains from a mechanistic point of view the processes leading to spatial organization. Moreover, the sulfur cycle is an important geochemical process present in very different ecosystems around the globe, hence, this mechanism is expected to have important implications not only for *P.oceanica* but for other seagrasses. Thus, the long-range competition introduced previously with a kernel is well explained in terms of the spreading of this phytotoxin. As a matter of fact, the interaction kernel can be recovered for certain limits of parameters. In this limit, however, the oscillatory dynamics is not present, showing the limitations of using an effective kernel to describe the interaction. Additionally, the model shows that bistability is necessary to make possible the formation of rings, which will not be created without an excitable region.

The presence of oscillatory behavior is a significant change in the study of the problem from different perspectives. On the one hand, it adds a new level of complexity to the study of the dynamics. The number of possible dynamic regimes is increased as we have shown, giving rise not only to patterns and oscillations but to

mixed behaviors like the formation of rings, oscillatory patterns or turbulence. On the other hand, from the measurements, diagnostic and predictive points of view not considering this possible behavior can lead to wrong interpretations of the state of a meadow and obviously wrong predictions of its future development.

This simple approach, which allows to obtain analytical expressions and simplify the calculations, has important advantages in the understanding of the dynamics. However, as we have seen, the model also has some limitations. In particular, sometimes it develops negative sulfide concentrations when describing oscillatory regimes. This can be easily solved by introducing a saturation of the facilitative term. Even so, the variability of the data used for parametrization introduces stronger uncertainties in the results obtained with the model. In other words, although the obtained results point to the presence of pattern forming and oscillatory instabilities, some values of the parameters used in the parametrization require unreasonably large values of the diffusion. Moreover, changes in these parameters produce big shifts in the threshold of the oscillatory instability. Thus, the experimental measurements are not accurate enough to determine which are the dynamical regimes present. Notice also that not all measurements are taken in the same location neither measure the appropriate quantity, thus introducing more variability in results.

A number of open questions arise from the results in the chapter. For instance, which is the importance of this mechanism structuring spatial organization in seagrass ecosystems? Are oscillations of biomass or spatio-temporal chaos present in seagrass ecosystems? Is it a common phenomenon independent of species? Or some of them can be expected to be more susceptible?

As future perspectives, there are three important aspects which require more efforts. First, precise measurements in a single location of the parameters of the model. Second, an improvement of the model to guarantee positive sulfide concentration, and third, a deeper exploration of the dynamical regimes that emerge in the region of coexistence of the oscillatory instability and the Turing instability.

CHAPTER 6

Conclusions

Along this thesis different chapters address different questions in the context of theoretical ecology using tools which traditionally belong to physics. In particular, a big part of the thesis is focused on *Posidonia oceanica* due to its key importance for the Mediterranean, although other clonal plants have been considered. The ABD model, derived to describe the growth of clonal plants is a continuous model based on intrinsic mechanisms of growth which are measured experimentally and well quantified in the literature. Thus, the model describes properly clonal growth and it is applicable to many clonal species.

As it has been shown, long-range competitive interactions are the necessary ingredient for a meadow to develop vegetation patterns. An interaction distance around $20-30\ m$ is inferred from the analysis of spatial patterns in the cartography data from LIFE Posidonia project, which points to mechanisms related with matter movement as the most plausible explanation of the competitive interaction. With this ingredients the landscape features of the meadow are well reproduced by the model. More precisely an hexagonal pattern of holes without vegetation appears close to the coast. The pattern shows more elongated shapes at the shoreline while for deeper waters, closer where the homogeneous meadow prevails, isolated holes appear consistently with the existence of localized states predicted by pattern formation theory. Moreover, the formation of patterns explains high variability of density measurements close to the coast. Besides, the model has potential applications to identify critical thresholds after which the spatial configuration changes, which for extreme cases lead to complete desertification. As a result, the different landscapes appearing at different mortalities are useful as a diagnostic tool which allows to identify the environmental condition the meadow experiences.

From a more technical perspective we showed that the minimal numerical discretization for the modelization of the growth of *Posidonia oceanica* accounts only for eight directions of growth compatible with the branching angle. Through the study of the dependence on the angle we have reached the conclusion that the density of apices in

different directions of growth evolves towards an homogeneous configuration. When the branching angle is incommensurable with 2π the homogeneous configuration is the only possible solution, while in the commensurable case neutral modes allow the redistribution of plants in different directions of growth without cost, however, under the influence of noise differences in the angle wipe out with time. In the presence of patterns, or in fact when the gradient of the density is nonzero a preferred direction appears facing outwards the meadow. The associated modulation in the angle has the periodicity of 2π which is well described by eight directions of growth, justifying this minimal approach.

Although the ABD model provides a detailed description of clonal growth, it is computationally limited by the fact of being effectively 3 dimensional. In order to overcome this difficulty we have derived a simplified equation that describes the total density of shoots and reproduces the formation of patterns without taking into account for the direction of growth. In particular, the relation between the intrinsic growth parameters with the parameters in the simplified equation adds an extra value to the derivation. Mainly because the global effect of different mechanisms of growth like branching and elongation of the rhizome is reflected in the effective terms in the resultant equation through the dependence of the coefficients. This fact allows a better understanding of its role in the spatial colonization of the meadow. In particular the contribution of the term $d_1\|\nabla n\|^2$ is new, not appearing in other well know vegetation models and in this sense intrinsic of clonal growth. In fact more work is necessary to really determine the effects of this non-variational term in important features of the growth, like the velocity of vegetation fronts or the stability of stationary solution against drift.

The derivation of a simple equation describing the growth at different levels of simplification allows a deeper study of pattern formation. The simplification allows to apply more sophisticated numerical methods to track stationary solutions, which provide very important information about the dynamics of the meadows and the possible configurations that can be found at the seabottom. Specially important is the characterization of localized structures and its regimes of existence, which determine the evolution of vegetation fronts. In this direction the study of fronts dynamics in two dimensions is much more involved than the one dimensional case. The number of possible fronts increases substantially and multiple regions of coexistence between patterns exits, thus a very detailed characterization of the stability of vegetation fronts is necessary to understand the dynamics of the meadows. Moreover localized structures in two dimensions will play a very important role, in particular localized structures with radial symmetry are accessible with continuation techniques and would provide valuable knowledge to understand the propagation of fronts. However, more efforts are needed in this direction.

The last part of the work, presents a possible specific mechanism to explain the

formation of patterns in *Posidonia oceanica* meadows with applicability to other seagrasses. Using a simple description for the growth of the meadow we couple the equation describing the dynamical evolution of the shoot density to a diffusion equation describing the spreading of hydrogen sulfide concentration. Sulfides in the sediment generated due to decomposition of organic matter from dead plants in the surrounding produces an effective long-range competition that generates spatial patterns. Surprisingly, the consequences of introducing this mechanism go beyond the formation of patterns. The homogeneous meadow becomes also unstable to periodic oscillations. This fact together with the spatial dynamics give raise to a very reach set of dynamical behaviors. Particularly interesting is the presence of an homoclinic bifurcation which creates excitable dynamics. As a result pulse solutions, which form expanding rings like those found in the Danish Kattegat for *Zostera marina*, can be also explained by this mechanism. We have parametrized the model for two species *Z. marina* and *P. oceanica* considering the variability of the experimental measurements. The results show that the considered mechanisms is in fact a plausible explanation of pattern formation, however, the variability is broad and more precise measurements are necessary to corroborate the hypothesis. Clarifying if this mechanism is determining the evolution of the meadows can have important consequences for the study of these ecosystems, mainly because many works of monitoring and long-term forecasting rely on the assumption that no oscillatory dynamics are taking place. In this direction, the models can guide the measurements to determine which quantities are going to be the most relevant. For instance, the measurement of shoots density and sulfide concentration profiles in the radial direction of both localized structures, holes and patches can provide important information about the parameters of the model and, consequently, to confirm or discard the hypothesis.

The model used for the description of the growth of the meadow is a modified version of the simplified equation. The simplicity is very useful to understand general dynamical behaviors, nevertheless, it has important disadvantages in certain parameter regimes, in particular is unable to avoid the generation of negative values of sulfide concentration. Therefore, a more sophisticated version is needed to avoid that effect which we plan to develop in the future.

As a matter of fact, sulfur cycle is a geochemical process present in many seagrass ecosystems. It would not be surprising that many other marine ecosystems behavior can be explained by these or similar equations. In this sense new application of this work to other ecosystems would be an interesting topic of future research.

Other questions not explored in this thesis remain to be answered in the future. For example, fluctuations as a result of demographic noise can have important effects on the dynamics. In particular, demographic noise can shift critical transitions or prevent extinctions [151, 152]. From this perspective a stochastic version of the mod-

els presented in this work can provide important information about the evolution of vegetation.

From a more applied perspective, the model is a practical tool with the potential to study evolutionary features of the plant to improve spreading strategies. Moreover, more research is necessary to understand how the spreading of the meadow is affected by the different growth parameters associated to different species.

Besides different effects, like the role hydrodynamism, need to be analyzed to determine its contribution to spatial self-organization. In fact there is a big need to include vegetation dynamics in oceanographic models applied to coastal zones. Mainly because the change of the coastline due to the hydrodynamics is importantly affected by the presence of vegetation and vice versa. Another important question to address is the effects on the meadows of the expected raise in temperature for the next century. Regarding the oscillatory dynamics of the homogeneous solutions when the presence of sulfide is included, it would be very interesting from the mathematical and ecological point of view to include seasonal forcing and determine the effects on the oscillation. From a more ecological perspective, there is a big concern about the effect of invasive species in the growth of endemic meadows. Some of these proposals need to include new levels of description. In this sense the simplified equation is really appropriate to address these questions.

Summarizing, we have developed different models useful in different regimes of applicability, which give a theoretical framework to study pattern formation in clonal-growth plants. We have applied these tools mainly to *Posidonia oceanica* but other species are expected to be well modeled by this approach. We have contributed to answer specific question using these models but many other challenges remain to be solved.

Linear stability analysis of the ABD model

First we adimensionalize the ABD model scaling time, space and the density of plants, $t = \tau T$, $\vec{r} = \chi \vec{R}$ and $n'_{s,a} = \frac{\eta}{\chi^2} n_{s,a}$. The branching rate fixes the temporal scale. Once we have the temporal scale the spatial scale is determined by the velocity of the rhizome elongation. Finally the scale of the number of shoots is influenced, as expected, by the saturation through the parameter b:

$$\tau = \frac{1}{\omega_b}, \quad \chi = \frac{\nu}{\omega_b}, \quad \eta = \sqrt{\frac{\omega_b}{b} \frac{\nu^2}{\omega_b^2}}. \tag{A.1}$$

Thus we can write the new parameters in terms of the old ones:

$$\omega'_{d0} = \frac{\omega_{d0}}{\omega_b}, \quad \kappa' = \frac{\kappa}{\omega_b}, \quad a' = \sqrt{\frac{\omega_b}{b}} a, \quad \rho' = \frac{\rho \omega_b}{\nu}, \quad \sigma'_i = \frac{\omega_b \sigma_i}{\nu}. \tag{A.2}$$

In the new units $\omega'_b = \nu' = b' = 1$. In the following we drop the primes for simplicity in the notation.

In order to study the stability of the homogeneous solutions we consider perturbations of the form $n_s = n_s^* + n_{sp}$, $n_a = n_a^* + n_{ap}$. The linearized systems reads:

$$\partial_T n_{ap} = - \left[\omega_{d0} + (\kappa - \omega_{d0})(1 - e^{-an_t^*}) + n_t^{*2} \right] n_{ap}$$

$$+ \left[-2n_t^* n_{tp} - ae^{-an_t^*} \int \int \mathcal{K}(\vec{R} - \vec{R'}) n_{tp}(\vec{R'}) d\vec{R} \right] \frac{\rho}{2\pi(1+\rho)} n_t^*$$

$$- \hat{v}(\phi) \cdot \vec{\nabla} n_{ap} + \frac{1}{2} \left[n_{ap}(\phi + \phi_b) + n_{ap}(\phi - \phi_b) \right] \tag{A.3}$$

$$\partial_T n_{sp} = - \left[\omega_{d0} + (\kappa - \omega_{d0})(1 - e^{-an_t^*}) + n_t^{*2} \right] n_{sp}$$

$$+ \left[-2n_t^* n_{tp} - ae^{-an_t^*} \int \int \mathcal{K}(\vec{R} - \vec{R'}) n_{tp}(\vec{R'}) d\vec{R} \right] \frac{n_t^*}{(1+\rho)}$$

$$+ \frac{1}{\rho} \int n_{ap}(\phi) d\phi, \tag{A.4}$$

where $n_{tp} = n_{sp} + \int_0^{2\pi} n_{ap}(\vec{R}, \phi, t)d\phi$ and $\hat{v}(\phi)$ is a unit vector in direction ϕ. Since the advection term is periodic in ϕ [$\hat{v}(\phi) = (\cos\phi, \sin\phi)$], Eqs. (A.3)-(A.4) are a set of linear differential equations with periodic coefficients of periodicity 2π. Because the dependence in ϕ should be periodic, perturbations can be written in the following form:

$$n_{ap}(\vec{R}, \phi, t) = \sum_{q_\phi} \int\int \tilde{n}_{ap,q_\phi}(\vec{q}, t)e^{i\vec{q}\cdot\vec{R}}e^{iq_\phi\phi}d\vec{q} \tag{A.5}$$

$$n_{sp}(\vec{R}, t) = \int\int \tilde{n}_{sp}(\vec{q}, t)e^{i\vec{q}\cdot\vec{R}}d\vec{q}, \tag{A.6}$$

where i is the imaginary unit, and $q_\phi = \ldots, -1, 0, 1, 2\ldots$. Introducing Eqs. (A.5)-(A.6) in (A.3)-(A.4) we obtain the following set of coupled linear ordinary differential equations for the components $\tilde{n}_{ap,q_\phi}$, $\tilde{n}_{sp}$:

$$\partial_T\tilde{n}_{ap,q_\phi} = -\left[\omega_{d0} + (\kappa - \omega_{d0})(1 - e^{-an_t^*}) + n_t^{*2}\right]\tilde{n}_{ap,q_\phi}$$
$$-\frac{iq_+}{2}n_{ap,q_\phi+1} - \frac{iq_-}{2}n_{ap,q_\phi-1} + \cos(q_\phi\phi_b)\tilde{n}_{ap,q_\phi} \tag{A.7}$$

$$\partial_T\tilde{n}_{ap,0} = \left[1 - \omega_{d0} + (\kappa - \omega_{d0})(1 - e^{-an_t^*}) + n_t^{*2}\right]\tilde{n}_{ap,0}$$
$$+ \left[-2n_t^* - ae^{-an_t^*}\tilde{\mathcal{K}}(\vec{q})\right]\frac{\rho}{2\pi(1+\rho)}n_t^*\tilde{n}_{tp}$$
$$-\frac{iq_+}{2}\tilde{n}_{ap,+1} - \frac{iq_-}{2}\tilde{n}_{ap,-1} \tag{A.8}$$

$$\partial_T\tilde{n}_{sp} = -\left(\omega_{d0} + (\kappa - \omega_{d0})(1 - e^{-an_t^*}) + n_t^{*2}\right)\tilde{n}_{sp}$$
$$+ \frac{\left(-2n_t^* - ae^{-an_t^*}\tilde{\mathcal{K}}(\vec{q})\right)}{(1+\rho)}n_t^*\tilde{n}_{tp} + \frac{2\pi}{\rho}\tilde{n}_{ap,0}, \tag{A.9}$$

where $q_\pm = q_x \pm iq_y$.
Eqs. (A.7)-(A.9) describe the linear evolution of the perturbation of the homogeneous solutions. The rsh of this system of equations can be written in a matrix form of infinite dimension. We truncate the matrix operator at order $q_\phi = \pm 4$ (neglecting contributions with $|q_\phi| > 4$), which is equivalent to the numerical discretization of ϕ that has been used for the numerical simulations. Then, diagonalizing numerically we find the growth rate of perturbations with wavenumber $\vec{q} = (q_x, q_y)$. The diagonalization leads to 10 eigenvalues for each $\vec{q}$. The solution is stable if all eigenvalues $\lambda_j(q_x, q_y)$ have negative real part. On the contrary, if the real part of the eigenvalue for a given wave number $\vec{q}$ becomes positive, the homogeneous solution becomes unstable to perturbations with the corresponding spatial periodicity, and a spatial patterns forms.

A.1 Neutral modes for stationary patterns

The content of this appendix is devoted to demonstrate the existence of neutral modes when a pattern in space is formed. Essentially in the commensurable case, given a stationary solution of the model, which can be heterogeneous in space, like a pattern, due to the presence of neutral modes one can redistribute density of apices in different directions provided the total density in a given position does not change.

Let $n_s^*(\vec{r})$, $n_a^*(\vec{r}, \phi)$ be the stationary solution of Eqs. (2.1) and (2.2), as for instance the ones represented in Fig. 2.20. We propose the following ansatz $n_s(\vec{r}, t) = n_s^*(\vec{r})$, $n_a(\vec{r}, \phi, t) = n_a^*(\vec{r}, \phi)(1 + \delta n_a(\phi, t))$, with the condition that $\int_0^{2\pi} n_a^*(\vec{r}, \phi)\delta n_a(\phi, t)d\phi = 0$. Thus the contribution of $\delta n_a(\phi, t)$ to the total density at position $\vec{r}$ is zero, and it can only redistribute density in different directions of growth. Hence, introducing the ansatz in Eqs. (2.1) and (2.2) we obtain:

$$n_a^*(\vec{r}, \phi)\partial_t \delta n_a(\phi, t) =$$
$$-\omega_d(n_t^*)n_a^*(\vec{r}, \phi) - \vec{v}(\phi) \cdot \vec{\nabla} n_a^*(\vec{r}, \phi) + \frac{\omega_b}{2}\left(n_a^*(\vec{r}, \phi + \phi_b) + n_a^*(\vec{r}, \phi - \phi_b)\right)$$
$$-\omega_d(n_t^*)n_a^*(\vec{r}, \phi)\delta n_a(\phi, t) - \vec{v}(\phi) \cdot \vec{\nabla} n_a^*(\vec{r}, \phi)\delta n_a(\phi, t)$$
$$+\frac{\omega_b}{2}\left(n_a^*(\vec{r}, \phi + \phi_b)\delta n_a(\phi + \phi_b, t) + n_a^*(\vec{r}, \phi - \phi_b)\delta n_a(\phi - \phi_b, t)\right) \qquad \text{(A.10)}$$

$$0 = -\omega_d(n_t^*)n_s^*(\vec{r}) + \frac{\nu}{\rho}\int_0^{2\pi} n_a^*(\vec{r}, \phi)d\phi. \qquad \text{(A.11)}$$

The first three terms in the rhs of Eq. (A.10) correspond to the stationary condition and they cancel each other. The fourth and fifth terms are equal to

$$-\frac{\omega_b}{2}\left(n_a^*(\vec{r}, \phi + \phi_b) + n_a^*(\vec{r}, \phi - \phi_b)\right)\delta n_a(\phi, t), \qquad \text{(A.12)}$$

according to the stationary condition. Eq. (A.11) corresponds to the stationary condition for Eq. (2.2). Thus one obtains the following expression:

$$n_a^*(\vec{r}, \phi)\partial_t \delta n_a(\phi, t) = -\frac{\omega_b}{2}\left(n_a^*(\vec{r}, \phi + \phi_b) + n_a^*(\vec{r}, \phi - \phi_b)\right)\delta n_a(\phi, t)$$
$$+\frac{\omega_b}{2}\left(n_a^*(\vec{r}, \phi + \phi_b)\delta n_a(\phi + \phi_b, t) + n_a^*(\vec{r}, \phi - \phi_b)\delta n_a(\phi - \phi_b, t)\right). \qquad \text{(A.13)}$$

One can write $n_a(\vec{r}, \phi) = \sum_{q_\phi} b_{q_\phi}(\vec{r})e^{iq_\phi\phi}$ and $\delta n_a(\phi, t) = \sum_{q'_\phi} \delta b_{q'_\phi}(t)e^{iq'_\phi\phi}$ as a Fourier series and substitute in Eq. (A.13). Rearranging terms with the same exponential term $q = q_\phi + q'_\phi$ one obtains a set of ordinary differential equations labeled by $q \in \mathbb{Z}$ of the following form:

$$\sum_{q'_\phi} b_{q-q'_\phi}(\vec{r})\partial_t \delta b_{q'_\phi}(t) = \sum_{q'_\phi} \omega_b(\cos(q\phi_b) - \cos((q - q'_\phi)\phi_b))b_{q-q'_\phi}(\vec{r})\delta b_{q'_\phi}(t) \qquad \text{(A.14)}$$

The eigenvalues of the problem are difficult to obtain from the previous expression, and they may not have an analytical closed form, however, a more simple strategy is to impose the condition that the modes of the perturbation are those with $q'_{\phi,n} = \frac{2\pi}{\phi_b}n$, which makes the rhs of (A.14) zero. Hence, these modes are neutral independently of the stationary solution, meaning one can redistribute density in different directions as long as it is periodic with ϕ_b and does not change the total density of apices.

A.2   Time dependence of the fluctuations

In this part we present and derive some expressions which are necessary in chapter 2 to understand the evolution of the size of the fluctuations. The fluctuations of white noise given by the Dirac delta diverge locally, to implement it numerically one has to consider the coarse-grained noise defined as

$$\xi_j^{cg}(t) = \frac{1}{\Delta\phi} \int_{j\Delta\phi}^{(j+1)\Delta\phi} \xi(\phi,t)d\phi. \tag{A.15}$$

The average is $< \xi_j^{cg}(t) >= 0$ and the fluctuations are given by

$$
\begin{aligned}
< \xi_j^{cg}(t)\xi_{j'}^{cg}(t') > &= \frac{1}{\Delta\phi^2} \int_{j\Delta\phi}^{(j+1)\Delta\phi} \int_{j'\Delta\phi}^{(j'+1)\Delta\phi} < \sqrt{\epsilon}\xi(\phi,t)\sqrt{\epsilon}\xi(\phi',t') > d\phi d\phi' \\
&= \frac{\epsilon}{\Delta\phi}\delta_{j,j'}\delta(t-t'). \tag{A.16}
\end{aligned}
$$

As a result one can compute the noise in Fourier space just applying the discrete Fourier transform $\tilde{f}_n = \frac{1}{N}\sum_j f_j e^{-i\frac{2\pi}{N}nj}$ where f_j are the values of the field and $\tilde{f}_n$ the amplitude of the n Fourier mode.

$$
\begin{aligned}
< \tilde{\xi}_n(t)\tilde{\xi}_{n'}(t') > &= \frac{1}{N^2}\sum_{j,j'} e^{-i\frac{2\pi}{N}(nj+n'j')} < \xi_j^{cg}(t)\xi_{j'}^{cg}(t') > \\
&= \frac{1}{N^2}\sum_{j,j'} e^{-i\frac{2\pi}{N}(nj+n'j')}\frac{\epsilon}{\Delta\phi}\delta_{j,j'}\delta(t-t') \\
&= \frac{1}{N^2}\sum_{j} e^{-i\frac{2\pi}{N}(n+n')j)}\frac{\epsilon}{\Delta\phi}\delta(t-t') \\
&= \frac{\epsilon}{2\pi}\delta_{n,-n'}\delta(t-t'). \tag{A.17}
\end{aligned}
$$

The fluctuations of the real part of $\tilde{\xi}_n(t)$, which we represent in Fig. 2.16 can be

computed as previously

$$
\begin{aligned}
< Re[\tilde{\xi}_n(t)]Re[\tilde{\xi}_{n'}(t')] > &= \frac{1}{N^2}\sum_{j,j'}\cos\left(-i\frac{2\pi}{N}nj\right)\cos\left(-i\frac{2\pi}{N}n'j'\right) < \xi_j^{cg}(t)\xi_{j'}^{cg}(t') > \\
&= \frac{1}{N^2}\sum_{j,j'}\cos\left(-i\frac{2\pi}{N}nj\right)\cos\left(-i\frac{2\pi}{N}n'j'\right)\frac{\epsilon}{\Delta\phi}\delta_{j,j'}\delta(t-t') \\
&= \frac{\epsilon\delta(t-t')}{4N^2\Delta\phi}\sum_j e^{-i\frac{2\pi}{N}(n+n')j} + e^{i\frac{2\pi}{N}(n+n')j} \\
&\qquad\qquad +e^{-i\frac{2\pi}{N}(n-n')j} + e^{i\frac{2\pi}{N}(n-n')j} \\
&= \frac{\epsilon}{4\pi}\delta(t-t')(\delta_{n,n'}+\delta_{n,-n'}).
\end{aligned}
\tag{A.18}
$$

In the Fourier space the linear dynamics can be written as $\frac{db_n}{dt} = \lambda_n b_n + \tilde{\xi}_n(t)$. Damped modes follow an Ornstein-Uhlenbeck process with zero mean and variance $\frac{1-e^{2\lambda_n t}}{-2\lambda_n}$. While neutral modes will follow a diffusive process with variance $\frac{\epsilon t}{2\pi}$ and zero mean. Thus, since we know the evolution of the fluctuations of all modes in Fourier, for the linear regime we can compute the fluctuation in real space. The discretized field can be written in terms of the Fourier amplitudes $n_{a,j} = \sum_n b_n(t)e^{i2\pi nj/N}$ where $b_n(t) = \int_0^t \tilde{\xi}_n(s)ds$ for neutral modes and $b_n(t) = e^{\lambda_n t}\int_0^t e^{-\lambda_n s}\tilde{\xi}_n(s)ds$ for damped modes. The fluctuations in real space are the result of products between modes, neutral with neutral, damped with damped, and neutral with damped. Notice the third group does not contribute mainly because from (A.17) opposite index n is needed. Thus, written in terms of the sums between neutral modes and between damped modes it follows

$$
\begin{aligned}
< n_{a,j}(t)^2 > &= < b_0(t)^2 > + \sum_{\substack{n,n' \\ neutral}} e^{i\frac{2\pi}{N}(n+n')j}\iint_0^t < \xi_n(s)\xi_{n'}(s') > dsds' \\
&\quad + \sum_{\substack{n,n' \\ damped}} e^{i\frac{2\pi}{N}(n+n')j}e^{(\lambda_n+\lambda_{n'})t}\iint_0^t e^{\lambda_n s+\lambda_{n'}s'} < \tilde{\xi}_n(s)\tilde{\xi}_{n'}(s') > dsds' \\
&= < b_0(t)^2 > + \sum_{\substack{n \\ neutral}}\frac{\epsilon t}{2\pi} + \sum_{\substack{n \\ damped}}\frac{\epsilon}{2\pi}\frac{1-e^{2\lambda_n t}}{-2\lambda_n}.
\end{aligned}
\tag{A.19}
$$

The homogeneous mode is not an eigenmode of the linear system, therefore the fluctuations are a combination of the contribution of apices and shoots. Consider the vector space formed by vectors $\vec{n} = (n_1, n_2)$ where the first component corresponds to shoot density and the second to the homogeneous mode of apices density. Essentially, the solution to the linear problem is a linear combination of the eigenvectors

and $b_0(t) = a_1(t)A_{21} + a_2(t)A_{22}$ is the second component of this linear combination which corresponds to apices. A_{ij} are the matrix elements of the basis change matrix with the two eigenvectors written in columns, and $a_i(t)$ the amplitude of each eigenvectors which we are going to obtain in the next lines. The linear problem can be written in the form $\partial_t a_i(t)n_j^i = J_{jk}a_i(t)n_k^i + \tilde{\xi}_0(t)\delta_{2,j}$, where n_j^i is the ith eigenvector and J_{jk} the elements of the Jacobian evaluated around the homogeneous solutions. Thus, applying A^{-1} to change to the diagonal basis and projecting on each eigenvector one obtains the equation for the time evolution of the amplitudes $\partial_t a_i(t) = \lambda_i a_i(t) + A_{i2}^{-1}\tilde{\xi}_0(t)$, which again leads to $a_i(t) = e^{\lambda_i t} \int_0^t e^{-\lambda_i s}\tilde{\xi}_0(s)ds$ where λ_i are the eigenvalues of the Jacobian. As a result one can compute the fluctuations of the homogeneous mode in terms of the basis change matrix and its inverse, which at the end are computed numerically since they depend on the homogeneous solution which does not have an analytical expression.

$$
\begin{aligned}
< b_0(t)^2 > \ &= \ (a_1(t)A_{21})^2 + (a_2(t)A_{22})^2 + 2(a_1(t)a_2(t)A_{21}A_{22}) \\
&= \ (A_{21}A_{12}^{-1})^2 e^{2\lambda_1 t} \iint_0^t e^{-\lambda_1(s+s')} < \tilde{\xi}_0(s)\tilde{\xi}_0(s') > dsds' \\
&\quad + (A_{22}A_{22}^{-1})^2 e^{2\lambda_2 t} \iint_0^t e^{-\lambda_2(s+s')} < \tilde{\xi}_0(s)\tilde{\xi}_0(s') > dsds' \\
&\quad + 2(A_{21}A_{22}A_{12}^{-1}A_{22}^{-1}) e^{(\lambda_1+\lambda_2)t} \iint_0^t e^{-\lambda_1 s - \lambda_2 s'} < \tilde{\xi}_0(s)\tilde{\xi}_0(s') > dsds' \\
&= \ \frac{\epsilon}{2\pi} \left((A_{21}A_{12}^{-1})^2 \frac{1 - e^{2\lambda_1 t}}{-2\lambda_1} + (A_{22}A_{22}^{-1})^2 \frac{1 - e^{2\lambda_2 t}}{-2\lambda_2} \right. \\
&\quad \left. + 2(A_{21}A_{22}A_{12}^{-1}A_{22}^{-1}) \frac{1 - e^{(\lambda_1+\lambda_2)t}}{-(\lambda_1 + \lambda_2)} \right).
\end{aligned}
\tag{A.20}
$$

According to Eq. (A.19) the size of the fluctuations in real space depends on the number of modes considered in the integration, or equivalently on $\Delta\phi$. This essentially is a result of the numerical implementation of the noise. For an appropriate numerical implementation of the noise instead of describing $n_a(i\Delta\phi)$, the standard procedure requires describing the average density in the interval $\Delta\phi$ as $n_{a,i} = \int_{i\Delta\phi}^{(i+1)\Delta\phi} n_a(\phi)d\phi/\Delta\phi$. Thus, assuming the variance of the field is $\sigma[n_a(\phi)]^2\delta(\phi - \phi')$ the variance of the discretized field reads

$$
\begin{aligned}
< n_{a,i} n_{a,i} > & = \frac{1}{\Delta\phi^2} \int_{i\Delta\phi}^{(i+1)\Delta\phi} \int_{i\Delta\phi}^{(i+1)\Delta\phi} < n_a(\phi)n_a(\phi') > d\phi d\phi' \\
& = \frac{1}{\Delta\phi^2} \int_{i\Delta\phi}^{(i+1)\Delta\phi} \int_{i\Delta\phi}^{(i+1)\Delta\phi} \sigma[n_a(\phi)]^2 \delta(\phi - \phi') d\phi d\phi' \\
& = \frac{\sigma[n_a(\phi)]^2}{\Delta\phi}.
\end{aligned}
\tag{A.21}
$$

which explains the dependence on the number of modes in Eq. (A.19). We plot in Fig. 2.16 $\sigma[n_a(\phi)] = \sqrt{< n_{a,i} n_{a,i} > \Delta\phi}$.

The real Discrete Fourier transform due to technical details stores in the last mode n the sum of the amplitudes b_n and b_{-n} which are equal between them as $DFT_n = b_n + b_{-n}$. When we represent the last mode we apply a correction factor $1/2$ such that $b_n = DFT_n/2$ and we compute averages and standard deviations. It is easy to prove that the standard deviation has the correction factor $\sigma[b_n] = \sqrt{2}\sigma[\frac{DFT_n}{2}] = \sqrt{2}\sigma[\frac{b_n + b_{-n}}{2}]$.

A.3 Pseudospectral integration with noise

According to Eq. (C.3) one can obtain a simpler algorithm for the integration of Eqs. (2.5), (2.6) and (2.7) which account for the noise.

$$
\tilde{A}(q, t+\delta t) = e^{-\alpha(q)(t+\delta t)} \left(\tilde{A}(q,t)e^{\alpha(q)t} + \int_t^{t+\delta t} \tilde{\Phi}(q,t)e^{\alpha(q)s} ds + \int_t^{t+\delta t} \tilde{\xi}(q,t)e^{\alpha(q)s} ds \right).
\tag{A.22}
$$

Similarly to the procedure in appendix C with $t = n\delta t$ and $q = k\Delta q$ (notice $\Delta q = 1$ in this case) and $f(q = k\Delta q) = f_k$. One has that

$$
\tilde{A}_k(n+1) = e^{-\alpha_k \delta t} \tilde{A}_k(n) + \frac{1 - e^{-\alpha_k \delta t}}{\alpha_k} \tilde{\Phi}_k(n) + \mathcal{W}_{\delta t, k}(n),
\tag{A.23}
$$

where $\mathcal{W}_{\delta t, k}(n)$ is not white noise because of the integrating factor. Thus, the average value $< \mathcal{W}_{\delta t, k}(n) > = 0$ and the variance is computed as follows:

$$
\begin{aligned}
< \mathcal{W}_{\delta t,k}(n)\mathcal{W}_{\delta t,k'}(n) > \;&=\; e^{-2\alpha_k(n+1)\delta t}\iint_{n\delta t}^{(n+1)\delta t} e^{(\alpha_k+\alpha_{k'})(s+s')} < \tilde{\xi}_k(s)\tilde{\xi}_{k'}(s') > dsds' \\
&=\; e^{-(\alpha_k+\alpha_{k'})(n+1)\delta t}\int_{n\delta t}^{(n+1)\delta t} e^{(\alpha_k+\alpha_{k'})s} < \tilde{\xi}_k\tilde{\xi}_{k'} > ds \\
&=\; \frac{1-e^{-(\alpha_k+\alpha_{k'})\delta t}}{2\alpha_k} < \tilde{\xi}_k\tilde{\xi}_{k'} > .
\end{aligned}
\tag{A.24}
$$

In order to generate a term with such variance, taking into account the fact that $\tilde{\xi}_k$ is the Fourier transform of the coarse grained noise. The noise term can be computed

$$
\mathcal{W}_{\delta t,k}(n) = \sqrt{\frac{1-e^{-2\alpha_k\delta t}}{2\alpha_k}\frac{\epsilon}{\Delta\phi}}\nu_k(n)
\tag{A.25}
$$

where $\nu_k(n) = \mathcal{F}[u_i(n)]$ are the amplitudes of the Fourier transform of the set of uncorrelated Gaussian random numbers $u_i(n)$ at each iteration n.

Supplementary analytical expressions of the model for coupled vegetation and sulfide concentration

B.0.1   Linear stability analysis

In this appendix we provide some of the expression that can be obtained from the linear stability analysis. In the first place we focus on the Hopf bifurcation which is determined by the eigenvalues at $q = 0$ given by the solution of the second order polynomial:

$$\lambda^2 - \lambda((a - 2bn^*)n^* + c_s\gamma n^* - \delta_s)$$
$$-(a - 2bn^*)n^*\delta_s + c_s\omega_b\gamma n^* = 0, \tag{B.1}$$

which has the form $\lambda^2 - \tau\lambda + \Delta = 0$ and the solutions will be $\lambda = \frac{\tau \pm \sqrt{\tau^2 - 4\Delta}}{2}$. The Hopf bifurcation needs $\tau = 0$ and $\Delta > 0$, if one considers $n^* = n_+^*$ the second condition is immediately satisfied. The first imply

$$(a - 2bn_+^*)n_+^* + c_s\gamma n_+^* - \delta_s = 0 \tag{B.2}$$

Substituting n_+^*, and after some steps of calculation, one obtains a second order polynomial with solutions:

$$\gamma_{Hopf} = \frac{a(\delta_s^2 + 3\delta_s\omega_b + 2\omega_b(\omega_b - \omega_{d0})) \pm (\delta_s + 2(\omega_b - \omega_{d0}))\sqrt{a^2(\delta_s + \omega_b)^2 - 4b\delta_s(\delta_s + 2\omega_b)\omega_{d0}}}{2c_s(\delta_s + 2\omega_b)\omega_{d0}}$$
$$\tag{B.3}$$

For the Turing instability one checks when the eigenvalue of the wavenumber with maximum growth rate becomes positive. We haven't found an analytical expression

for the Turing bifurcation but we can obtain the critical wavenumber. To do so we derive implicitly Eq. (5.6) and introduces the condition $Re[\lambda(q_c)] = 0$ and $\frac{\partial \lambda(q)}{\partial q}|_{q=q_c} = 0$. Thus one can easily obtain

$$q_c^2 = \frac{(a - 2bn^*)n^*D_s + (d_0 + d_1n^*)c_s\gamma n^* - \delta_s(d_0 + d_1n^*)}{2D_s(d_0 + d_1n^*)} \tag{B.4}$$

B.0.2   Adimensionalization

It can be helpful in the analysis to remove some parameters performing an adimensionalization of the equations. We have used one similar to the presented in chapter 1 for convenience, where $n' = \eta/\chi^2 n$, $S' = \sigma S$, $x' = \chi x$, $t' = \tau t$ being $\eta = \sqrt{\frac{\omega_b}{b}}\frac{\nu^2}{\omega_b^2}$, $\sigma = c_s\sqrt{\frac{\omega_b}{b}}$, $\chi = \frac{\nu^2}{\omega_b^2}$, $\tau = \frac{1}{\omega_b}$. Thus the new set of parameters is $\omega_b' = 1$, $\omega_{d0}' = \frac{\omega_{d0}}{\omega_b}$, $a' = \frac{a}{\sqrt{b\omega_b}}$, $b' = 1$, $d_0' = d_0\frac{\omega_b}{\nu^2}$, $d_1' = d_1\frac{\omega_b}{\nu^2}\sqrt{\frac{\omega_b}{b}}$, $\delta_s' = \frac{\delta_s}{\omega_b}$, $D_s' = D_s\frac{\omega_b}{\nu^2}$, $c_s' = 1$, $\gamma' = \gamma\frac{c_s}{\omega_b}\sqrt{\frac{\omega_b}{b}}$.

Pseudospectral integration method

In this thesis we integrate different partial differential equations, and integro-differential equations. In this appendix we describe the integration method used, which is adapted from [153]. All equations in the thesis can be written in the following form using the Einstein summation convention,

$$\partial_t A_i(\vec{x}, t) = \hat{\mathcal{L}}_i^j A_j(\vec{x}, t) + \mathcal{N}_i(\mathbf{A}, \nabla^{(k)} \mathbf{A}), \tag{C.1}$$

where $\mathbf{A}$ is the vector formed by all fields $A_i(\vec{x}, t)$, with $\vec{x} \in \mathbb{R}^n$ being $n = 1, 2$. Generally $\hat{\mathcal{L}}_i^j$ is a linear differential operator and $\mathcal{N}_i$ a nonlinear function of $\mathbf{A}$ and its derivatives. The pseudospectral method solves Eq. (C.1) in Fourier space with periodic boundary conditions,

$$\partial_t \tilde{A}_i(\vec{q}, t) = -\alpha_i^j(\vec{q}) \tilde{A}_j(\vec{q}, t) + \tilde{\Phi}_i(\vec{q}, t), \tag{C.2}$$

where $\tilde{A}_i(\vec{q}, t) = \mathcal{F}[A_i(\vec{x}, t)]$, $-\alpha_i^j(\vec{q})$ is the Fourier transform of the linear operator $\mathcal{L}_i^j$, where the minus sign is taken for convenience and $\tilde{\Phi}_i(\vec{q}, t)$ is the Fourier transform of $\mathcal{N}_i$ computed in real space. For those equations with convolution terms in the nonlinear part we use the convolution theorem to compute the integral integral in real space. First, we do the product of the field with the analytical expression of the kernel in Fourier space and we antitransform to real space. Finally we compute the resultant nonlinear term and transform to Fourier space again. Nonlinear terms with derivatives are also computed in this fashion. We use Fast Fourier transform from Intel math kernel libraries to compute Fourier transforms. Except one of the equations studied in this thesis, all have only diagonal terms in the linear term, so we consider for simplicity $\alpha_i^j = 0$ for $i \neq j$ and $\alpha_i^i = \alpha_i$. The model which has off-diagonal can be integrated with the same method including these terms in the nonlinear part. Equation (C.2) is integrated with a two-step method. For convenience the time step in each iteration is defined as $2\delta_t$. Thus, the linear part can be integrated effectively

using the exact formal solution obtained multiplying by the integrating factor $e^{\alpha_i(\vec{q})t}$ at both sides and in integrating in time.

$$\tilde{A}_i(\vec{q}, t) = e^{-\alpha_i(\vec{q})t} \left(\tilde{A}_i(\vec{q}, t_0)e^{\alpha_i(\vec{q})t_0} + \int_{t_0}^{t} \tilde{\Phi}_i(\vec{q}, s)e^{\alpha_i(\vec{q})s}ds \right) \tag{C.3}$$

where the following expression can be obtained.

$$\frac{\tilde{A}_i(\vec{q}, t + \delta t)}{e^{-\alpha_i(\vec{q})\delta t}} - \frac{\tilde{A}_i(\vec{q}, t - \delta t)}{e^{\alpha_i(\vec{q})\delta t}} = e^{-\alpha_i(\vec{q})t} \int_{t-\delta t}^{t+\delta t} \Phi_i(\vec{q}, s)e^{\alpha_i(\vec{q})s}ds \tag{C.4}$$

The rhs can be approximated with a Taylor expansion around $s = t$ to give

$$\Phi_i(\vec{q}, t)\frac{e^{\alpha_i(\vec{q})\delta t} - e^{-\alpha_i(\vec{q})\delta t}}{\alpha_i(\vec{q})} + O(\delta t^3) \tag{C.5}$$

Substituting in Eq. (C.4) and replacing $t = n\delta t$ one obtains

$$\tilde{A}_i(\vec{q}, n + 1) = e^{-2\alpha_i(\vec{q})\delta t}\tilde{A}_i(\vec{q}, n - 1) + \frac{1 - e^{-2\alpha_i(\vec{q})\delta t}}{\alpha_i(\vec{q})}\Phi_i(\vec{q}, n) + O(\delta t^3) \tag{C.6}$$

Eq. (C.6) is the so called slaved leap frog [154] which is unstable and a corrective algorithm must be applied. The correction expression can be determined following steps similar to the previous case.

$$\tilde{A}_i(\vec{q}, n) = e^{-\alpha_i(\vec{q})\delta t}\tilde{A}_i(\vec{q}, n - 1) + \frac{1 - e^{-\alpha_i(\vec{q})\delta t}}{\alpha_i(\vec{q})}\Phi_i(\vec{q}, n - 1) + O(\delta t^2) \tag{C.7}$$

Eqs. (C.6) and (C.7) constitute the two-step method, where the error is $O(\delta t^3)$ although the intermediate step has error $O(\delta t^2)$. The algorithm follows the following steps:

1. Compute $\tilde{A}_i(\vec{q}, n - 1)$ and $\Phi_i(\vec{q}, n - 1)$ as the Fourier transform of $A_i(\vec{x}, n - 1)$ and $\mathcal{N}_i(\mathbf{A}(n - 1), \nabla^{(k)}\mathbf{A}(n - 1))$ computed in real space.

2. Obtain $\tilde{A}_i(\vec{q}, n)$ using Eq. (C.7).

3. Using the inverse Fourier transform of $\tilde{A}_i(\vec{q}, n)$ compute $\mathcal{N}_i(\mathbf{A}(n), \nabla^{(k)}\mathbf{A}(n))$ and obtain $\Phi_i(\vec{q}, n)$ with the direct Fourier transform.

4. Obtain $\tilde{A}_i(\vec{q}, n + 1)$ using Eq. (C.6).

With the previous four steps one iteration is performed where the time increment is $2\delta t$.

Continuation methods

D.1 Newton-Raphson method

The method explained here is a generalization of Newton's method designed to find the solution u of a nonlinear problem $F[u] = 0$. We use it to find stationary solutions of a nonlinear partial differential equation of the form

$$\partial_t u(\vec{x}, t) = F[u(\vec{x}, t)], \tag{D.1}$$

where F is a nonlinear function of the field $u(\vec{x}, t)$ and its derivatives. Therefore, we are interested in finding the solution of $F[u(\vec{x}, t)] = 0$. Considering $u^{(0)}$ the first estimate of the solution we can use a first order Taylor expansion to write

$$F[u] = F[u^{(0)}] + \mathcal{D}F[u^{(0)}](u - u^{(0)}) + \mathcal{O}(2), \tag{D.2}$$

where $\mathcal{D}F[u^{(0)}]$ is the functional derivative of F with respect to the field u evaluated at the estimate $u^{(0)}$. Thus, realizing that $F[u] = 0$ one can find a new estimate u as the solution of the linear problem

$$u = u^{(0)} - \mathcal{D}F[u^{(0)}]^{-1} F[u^{(0)}] + \mathcal{O}(2) \tag{D.3}$$

Applying recursively this relation one can refine the estimate to be arbitrary close to the stationary solution. The recurrence relation can be written

$$u^{(n+1)} = u^{(n)} - \mathcal{D}F[u^{(n)}]^{-1} F[u^{(n)}] + \mathcal{O}(2). \tag{D.4}$$

Numerically the field $u(\vec{x})$ is discretized in space $u_j = u((j_x-1)\Delta x, (j_y-1)\Delta y)$ where $j = j_x + (j_y-1)N_x$, $j_x = 1, ..., N_x$ and $j_y = 1, ..., N_y$. Thus, the field can be considered a vector $\mathbf{u}$ of components u_j in a $N = N_x N_y$ dimensional space. Equivalently there is

a vector $\mathbf{F}[\mathbf{u}] = 0$ with components $F_k[u_1, ..., u_N] = 0$. Including that the algorithm reads

$$u_j^{(n+1)} = u_j^{(n)} - \mathcal{D}F[u^{(n)}]_{jl}^{-1} F_l[u^{(n)}].$$ (D.5)

In this way the problem is reduced to a linear problem, which can be solved with standard libraries. After a number of iterations the approximation converges to the solution $\mathbf{u}$, such that $\mathbf{F}[\mathbf{u}^{(n)}] < \epsilon$.

The effectiveness of the method is clear when one considers the dependence of the stationary solution with a parameter μ. Thus, using the solution $\mathbf{u_k}$ for a given value of the parameter μ_k as first estimate we can compute the solution $\mathbf{u_{k+1}}$ for the value of μ_{k+1}. In other words, as long as we are close enough to the original solution we can use $\mathbf{u_{k+1}} = \mathbf{u_k}$ as initial seed and make it converge with the Newton-Raphson method.

Following this procedure it is possible to continue the solution for all values of the parameter μ in which the solution exists. In general, this allows to reconstruct the parametric curve $\mathbf{u}(\mu)$ in $\in \mathbb{R}^{N+1}$, which is the solution of $\mathbf{F}[\mathbf{u}, \mu] = 0$. Unfortunately, the method fails when the curve folds, basically because $\frac{d\mathbf{u}}{d\mu} = \infty$.

D.2 Keller's pseudo-arclength continuation

The alternative method to avoid the limitations of the Newton-Raphson method is to reparametrize the curve $\mathbf{u}(\mu)$ with arclength parameter s defined by the condition

$$\left\| \frac{d\mathbf{u}}{ds} \right\|^2 + \left(\frac{d\mu}{ds} \right) = 1.$$ (D.6)

The aim is to continue the curve starting with an initial stationary solution $\mathbf{v_k}(s_k) = (\mathbf{u_0}(s_k), \mu(s_k))$ to reach $\mathbf{v_{k+1}}(s_{k+1}) = (\mathbf{u_{k+1}}(s_{k+1}), \mu(s_{k+1}))$. However, introducing the arclength parameter the problem needs an additional constrain in order to have a unique solution. The standard condition is written as follows

$$Q[\mathbf{u_{k+1}}, \mu_{k+1}, \Delta s] = (\mathbf{u_{k+1}} - \mathbf{u_k}) \cdot \dot{\mathbf{u}}_\mathbf{k} + (\mu_{k+1} - \mu_k)\dot{\mu}_k - \Delta s = 0,$$ (D.7)

where $\dot{\mathbf{v}}_\mathbf{k} = (\dot{\mathbf{u}}_\mathbf{k}, \dot{\mu}_k)$ is the tangent vector to the curve at $\mathbf{v_k}$. The condition essentially imposes that the new solution $\mathbf{v_{k+1}}$ must be in an hyperplane perpendicular to the tangent vector $\dot{\mathbf{v}}_\mathbf{k}$ at a distance Δs of the original solution $\mathbf{v_k}$. If the increment Δs is small enough the intersection of the hyperplane with the curve $\mathbf{v}(s)$ is guaranteed. We usually consider a more general condition given by:

$$Q[\mathbf{u_{k+1}}, \mu_{k+1}, \Delta s] = \theta(\mathbf{u_{k+1}} - \mathbf{u_k}) \cdot \dot{\mathbf{u}}_\mathbf{k} + (2 - \theta)(\mu_{k+1} - \mu_k)\dot{\mu}_k - \Delta s = 0,$$ (D.8)

which for $\theta = 1$ recovers the condition in Eq. (D.7). Essentially this allows to modify the orientation of the plane to enhance the importance of the parameter or the field, which can be useful when the convergence is difficult.

As a result we have to find the solution of the following system

$$\mathbf{G}[\mathbf{v}] = \begin{bmatrix} \mathbf{F}[\mathbf{v}] \\ Q[\mathbf{v}, \Delta s] \end{bmatrix} = \begin{bmatrix} 0 \\ 0 \end{bmatrix}, \tag{D.9}$$

which can be solved applying an improved Newton-Raphson method.
In the first iteration of the field the tangent vector to the curve $\dot{\mathbf{v}}_0$ is computed solving the linear problem.

$$\mathcal{D}\mathbf{F}[\mathbf{u_0}, \mu_0]\frac{\dot{\mathbf{u}}_0}{\dot{\mu}_0} = -\partial_\mu \mathbf{F}[\mathbf{u_0}, \mu_0], \tag{D.10}$$

$$\dot{\mu}_0 = \frac{1}{\sqrt{\left(\frac{\dot{\mathbf{u}}_0}{\dot{\mu}_0}\right)^2 + 1}}. \tag{D.11}$$

Once we have $\mathbf{v_0}$ and $\dot{\mathbf{v}}_0$ we can compute the following solutions along the curve with the following procedure. We use a predictor-corrector method, in particular the Euler predictor as the first step to obtain an approximation of the next solution

$$\mathbf{v_{k+1}}^{(0)} = \mathbf{v_k} + \dot{\mathbf{v}}_\mathbf{k}\Delta s. \tag{D.12}$$

The second step makes use of the Newton-Raphson method as corrector

$$\begin{bmatrix} \mathcal{D}\mathbf{F} & \partial_\mu \mathbf{F} \\ \delta_u Q & \partial_\mu Q \end{bmatrix}_{(\mathbf{u_{k+1}}^{(n)}, \mu_{k+1}^{(n)})} \begin{bmatrix} \Delta\mathbf{u_{k+1}}^{(n)} \\ \Delta\mu_{k+1}^{(n)} \end{bmatrix} = -\begin{bmatrix} \mathbf{F}[\mathbf{u_{k+1}}^{(n)}, \mu_{k+1}] \\ Q[\mathbf{u_{k+1}}^{(n)}, \mu_{k+1}, \Delta s] \end{bmatrix}, \tag{D.13}$$

which in a more compact form can be written

$$\mathcal{D}\mathbf{G}[\mathbf{v}_{k+1}^{(n)}]\Delta\mathbf{v}_{k+1}^{(n)} = -\mathbf{G}[\mathbf{v}_{k+1}^{(n)}], \tag{D.14}$$

where the next approximation $n + 1$ to the solution can be found in terms of the increment $\Delta\mathbf{v}_{k+1}^{(n)}$, which is the solution of the previous linear problem.

$$\mathbf{v}_{k+1}^{(n+1)} = \mathbf{v}_{k+1}^{(n)} + \Delta\mathbf{v}_{k+1}^{(n)}. \tag{D.15}$$

After a number of iterations the approximation converges to the solution $\mathbf{v}_{k+1}$, such that $\mathbf{G}[\mathbf{v}_{k+1}^{(n)}] < \epsilon$. Finally, the last step computes the tangent vector to the curve at the obtained solution with the following linear problem.

$$\begin{bmatrix} \mathcal{D}\mathbf{F} & \partial_\mu \mathbf{F} \\ \dot{\mathbf{u}}_\mathbf{k} & \dot{\mu}_k \end{bmatrix}_{(\mathbf{u_{k+1}}, \mu_{k+1})} \begin{bmatrix} \dot{\mathbf{u}}_\mathbf{k+1} \\ \dot{\mu}_\mathbf{k+1} \end{bmatrix} = \begin{bmatrix} 0 \\ 1 \end{bmatrix} \tag{D.16}$$

And the vector is rescaled to be unitary.

$$\dot{\mathbf{v}}_{\mathbf{k+1}} = \frac{\dot{\mathbf{v}}_{\mathbf{k+1}}}{\|\dot{\mathbf{v}}_{\mathbf{k+1}}\|} \tag{D.17}$$

Thus, iteratively, the process can be repeated starting from Eq. (D.12). Further information can be found in [155–159].

Bibliography

[1] A. M. Turing, The chemical basis of morphogenesis. *Bulletin of Mathematical Biology* **52**, 153–197 (1990).

[2] M. C. Cross, P. C. Hohenberg, Pattern formation outside of equilibrium. *Reviews of modern physics* **65**, 851 (1993).

[3] D. Walgraef, *Spatio-temporal pattern formation: with examples from physics, chemistry, and materials science.* (Springer-Verlag, New York, 1997).

[4] M. Rietkerk, S. C. Dekker, P. C. de Ruiter, J. van de Koppel, Self-organized patchiness and catastrophic shifts in ecosystems. *Science* **305**, 1926–1929 (2004).

[5] R. V. Solé, J. Bascompte, *Self-organization in complex ecosystems* (Princeton University Press, 2006).

[6] M. Rietkerk, J. van de Koppel, Regular pattern formation in real ecosystems. *Trends in Ecology & Evolution* **23**, 169–175 (2008).

[7] M. Scheffer, *et al.*, Early-warning signals for critical transitions. *Nature* **461**, 53–59 (2009).

[8] K. Siteur, *et al.*, Beyond Turing: The response of patterned ecosystems to environmental change. *Ecological Complexity* **20**, 81–96 (2014).

[9] R. Bastiaansen, *et al.*, Multistability of model and real dryland ecosystems through spatial self-organization. *Proceedings of the National Academy of Sciences* **115**, 11256–11261 (2018).

[10] R. Lefever, O. Lejeune, On the origin of tiger bush. *Bulletin of Mathematical Biology* **59**, 263–294 (1997).

[11] C. A. Klausmeier, Regular and irregular patterns in semiarid vegetation. *Science* **284**, 1826–1828 (1999).

[12] P. Couteron, O. Lejeune, Periodic spotted patterns in semi-arid vegetation explained by a propagation-inhibition model. *Journal of Ecology* **89**, 616–628 (2001).

[13] J. von Hardenberg, E. Meron, M. Shachak, Y. Zarmi, Diversity of vegetation patterns and desertification. *Physical Review Letters* **87**, 198101 (2001).

[14] M. Rietkerk, *et al.*, Self-organization of vegetation in arid ecosystems. *The American Naturalist* **160**, 524–530 (2002).

[15] O. Lejeune, M. Tlidi, P. Couteron, Localized vegetation patches: a self-organized response to resource scarcity. *Physical Review E* **66**, 010901 (2002).

[16] O. Lejeune, M. Tlidi, R. Lefever, Vegetation spots and stripes: Dissipative structures in arid landscapes. *International Journal of Quantum Chemistry* **98**, 261–271 (2004).

[17] G. G. Penny, K. E. Daniels, S. E. Thompson, Local properties of patterned vegetation: quantifying endogenous and exogenous effects. *Philosophical Transactions of the Royal Society A: Mathematical, Physical and Engineering Sciences* **371**, 20120359 (2013).

[18] R. Lefever, N. Barbier, P. Couteron, O. Lejeune, Deeply gapped vegetation patterns: On crown/root allometry, criticality and desertification. *Journal of Theoretical Biology* **261**, 194–209 (2009).

[19] J. M. Thiéry, J. M. D'Herbès, C. Valentin, A model simulating the genesis of banded vegetation patterns in Niger. *Journal of Ecology* **83**, 497–507 (1995).

[20] N. Barbier, P. Couteron, J. Lejoly, V. Deblauwe, O. Lejeune, Self-organized vegetation patterning as a fingerprint of climate and human impact on semi-arid ecosystems. *Journal of Ecology* **94**, 537–547 (2006).

[21] V. Deblauwe, P. Couteron, O. Lejeune, J. Bogaert, N. Barbier, Environmental modulation of self-organized periodic vegetation patterns in Sudan. *Ecography* **34**, 990–1001 (2011).

[22] P. Gandhi, L. Werner, S. Iams, K. Gowda, M. Silber, A topographic mechanism for arcing of dryland vegetation bands. *Journal of the Royal Society, Interface* **15**, 20180508 (2018).

[23] E. Meron, E. Gilad, J. von Hardenberg, M. Shachak, Y. Zarmi, Vegetation patterns along a rainfall gradient. *Chaos, Solitons & Fractals* **19**, 367–376 (2004).

[24] E. Meron, Pattern-formation approach to modelling spatially extended ecosystems. *Ecological Modelling* **234**, 70–82 (2012).

[25] S. E. Thompson, K. E. Daniels, A porous convection model for grass patterns. *The American Naturalist* **175**, E10—-E15 (2010).

[26] N. Juergens, The biological underpinnings of Namib Desert fairy circles. *Science* **339**, 1618–1621 (2013).

[27] T. Becker, S. Getzin, The fairy circles of Kaokoland (North-West Namibia) - origin, distribution, and characteristics. *Basic and Applied Ecology* **1**, 149–159 (2000).

[28] C. E. Tarnita, *et al.*, A theoretical foundation for multi-scale regular vegetation patterns. *Nature* **541**, 398–401 (2017).

[29] W. R. Tschinkel, Experiments testing the causes of Namibian fairy circles. *PLoS ONE* **10**, 1–22 (2015).

[30] S. Getzin, *et al.*, Adopting a spatially explicit perspective to study the mysterious fairy circles of Namibia. *Ecography* **38**, 1–11 (2015).

[31] M. D. Cramer, N. N. Barger, Are Namibian "fairy circles" the consequence of self-organizing spatial vegetation patterning? *PLoS ONE* **8**, e70876 (2013).

[32] C. Fernandez-Oto, M. Tlidi, D. Escaff, M. G. Clerc, Strong interaction between plants induces circular barren patches: fairy circles. *Philosophical Transactions of the Royal Society A: Mathematical, Physical and Engineering Sciences* **372**, 20140009 (2014).

[33] W. R. Tschinkel, The life cycle and life span of Namibian fairy circles. *PLoS ONE* **7**, e38056 (2012).

[34] S. Getzin, *et al.*, Discovery of fairy circles in Australia supports self-organization theory. *Proceedings of the National Academy of Sciences* **113**, 3551–3556 (2016).

[35] K. Gowda, H. Riecke, M. Silber, Transitions between patterned states in vegetation models for semiarid ecosystems. *Physical Review E* **89**, 022701 (2014).

[36] Y. R. Zelnik, S. Kinast, H. Yizhaq, G. Bel, E. Meron, Regime shifts in models of dryland vegetation. *Philosophical Transactions of the Royal Society A: Mathematical, Physical and Engineering Sciences* **371**, 20120358 (2013).

[37] E. Meron, H. Yizhaq, E. Gilad, Localized structures in dryland vegetation: Forms and functions. *Chaos* **17**, 037109 (2007).

[38] E. Siero, *et al.*, Striped pattern selection by advective reaction-diffusion systems: Resilience of banded vegetation on slopes. *Chaos* **25**, 036411 (2015).

[39] E. Gilad, J. von Hardenberg, A. Provenzale, M. Shachak, E. Meron, Ecosystem engineers: From pattern formation to habitat creation. *Physical Review Letters* **93**, 098105 (2004).

[40] E. Gilad, J. von Hardenberg, A. Provenzale, M. Shachak, E. Meron, A mathematical model of plants as ecosystem engineers. *Journal of Theoretical Biology* **244**, 680–691 (2007).

[41] C. Fernandez-Oto, O. Tzuk, E. Meron, Front instabilities can reverse desertification. *Physical Review Letters* **122**, 048101 (2019).

[42] Y. R. Zelnik, P. Gandhi, E. Knobloch, E. Meron, Implications of tristability in pattern-forming ecosystems Yuval. *Chaos: An Interdisciplinary Journal of Nonlinear Science* **28**, 033609 (2018).

[43] D. K. Swanson, D. F. Grigal, A simulation model of mire patterning. *Oikos* **53**, 309–314 (1988).

[44] J. Couwenberg, H. Joosten, Self-organization in raised bog patterning: The origin of microtope zonation and mesotope diversity. *Journal of Ecology* **93**, 1238–1248 (2005).

[45] M. B. Eppinga, M. Rietkerk, M. J. Wassen, P. C. de Ruiter, Linking habitat modification to catastrophic shifts and vegetation patterns in bogs. *Plant Ecology* **200**, 53–68 (2009).

[46] L. G. Larsen, C. Thomas, M. B. Eppinga, T. Coulthard, Exploratory modeling: Extracting causality from complexity. *Eos* **95**, 285–286 (2014).

[47] L. G. Larsen, *et al.*, Appropriate complexity landscape modeling. *Earth-Science Reviews* **160**, 111–130 (2016).

[48] M. Rietkerk, S. C. Dekker, M. J. Wassen, A. W. M. Verkroost, M. F. P. Bierkens, A putative mechanism for bog patterning. *The American Naturalist* **163**, 699–708 (2004).

[49] M. B. Eppinga, *et al.*, Regular surface patterning of peatlands: Confronting theory with field data. *Ecosystems* **11**, 520–536 (2008).

[50] M. B. Eppinga, P. C. de Ruiter, M. J. Wassen, M. Rietkerk, Nutrients and hydrology indicate the driving mechanisms of peatland surface patterning. *The American Naturalist* **173**, 803–818 (2009).

[51] J. Leifeld, L. Menichetti, The underappreciated potential of peatlands in global climate change mitigation strategies. *Nature Communications* **9**, 1071 (2018).

[52] M. B. Eppinga, *et al.*, Resource contrast in patterned peatlands increases along a climatic gradient. *Ecology* **91**, 2344–2355 (2010).

[53] C. Den Hartog, The dynamic aspect in the ecology of seagrass communities. *Thalassia Jugoslavica* **7**, 101–1127 (1971).

[54] M. S. Frederiksen, D. Krause-Jensen, M. Holmer, J. S. Laursen, Spatial and temporal variation in eelgrass (Zostera marina) landscapes: influence of physical setting. *Aquatic Botany* **78**, 147–165 (2004).

[55] T. van Der Heide, *et al.*, Spatial self-organized patterning in seagrasses along a depth gradient of an intertidal ecosystem. *Ecology* **91**, 362–369 (2010).

[56] J. Borum, *et al.*, Eelgrass fairy rings: sulfide as inhibiting agent. *Marine Biology* **161**, 351–358 (2014).

[57] V. Pasqualini, C. Pergent-Martini, G. Pergent, Environmental impact identification along the Corsican coast (Mediterranean sea) using image processing. *Aquatic Botany* **65**, 311–320 (1999).

[58] M. Bonacorsi, C. Pergent-Martini, N. Breand, G. Pergent, Is Posidonia oceanica regression a general feature in the Mediterranean Sea? *Mediterranean Marine Science* **14**, 193–203 (2013).

[59] D. Ruiz-Reynés, *et al.*, Fairy circle landscapes under the sea. *Science Advances* **3**, e1603262 (2017).

[60] M. A. Hemminga, C. M. Duarte, *Seagrass ecology* (Cambridge University Press, 2000).

[61] G. Benoit, A. Comeau, *A sustainable future for the mediterranean: The blue plan's environment and development outlook* (2012).

[62] M. Waycott, *et al.*, Accelerating loss of seagrasses across the globe threatens coastal ecosystems. *Proceedings of the National Academy of Sciences* **106**, 12377–12381 (2009).

[63] C. M. Duarte, J. J. Middelburg, N. Caraco, Major role of marine vegetation on the oceanic carbon cycle. *Biogeosciences Discussions* **1**, 659–679 (2004).

[64] J. Terrados, C. M. Duarte, Experimental evidence of reduced particle resuspension within a seagrass (Posidonia oceanica L.) meadow. *Journal of Experimental Marine Biology and Ecology* **243**, 45–53 (2000).

[65] G. De Falco, E. Molinaroli, M. Baroli, S. Bellacicco, Grain size and compositional trends of sediments from Posidonia oceanica meadows to beach shore, Sardinia, western Mediterranean. *Estuarine, Coastal and Shelf Science* **58**, 299–309 (2003).

[66] T. Koftis, P. Prinos, V. Stratigaki, Wave damping over artificial Posidonia oceanica meadow: A large-scale experimental study. *Coastal Engineering* **73**, 71–83 (2013).

[67] C. M. Duarte, *et al.*, Seagrass community metabolism: Assessing the carbon sink capacity of seagrass meadows. *Global Biogeochemical Cycles* **24**, GB4032 (2010).

[68] C. M. Duarte, Seagrass nutrient content. *Marine Ecology Progress Series* **6**, 201–207 (1990).

[69] S. Enriquez, C. M. Duarte, K. Sand-Jensen, Patterns in decomposition rates among photosynthetic organisms: the importance of detritus C: N: P content. *Oecologia* **94**, 457–471 (1993).

[70] J. W. Fourqurean, *et al.*, Seagrass ecosystems as a globally significant carbon stock. *Nature Geoscience* **5**, 505–509 (2012).

[71] C. M. Duarte, T. Sintes, N. Marbà, Assessing the CO_2 capture potential of seagrass restoration projects. *Journal of Applied Ecology* **50**, 1341–1349 (2013).

[72] C. M. Duarte, I. J. Losada, I. E. Hendriks, I. Mazarrasa, N. Marbà, The role of coastal plant communities for climate change mitigation and adaptation. *Nature Climate Change* **6**, 802 (2016).

[73] A. M. Folkard, Hydrodynamics of model Posidonia oceanica patches in shallow water. *Limnology and Oceanography* **50**, 1592–1600 (2005).

[74] E. Infantes, J. Terrados, A. Orfila, B. Cañellas, A. Álvarez-Ellacuria, Wave energy and the upper depth limit distribution of Posidonia oceanica. *Botanica Marina* **52**, 419–427 (2009).

[75] C. M. Duarte, The future of seagrass meadows. *Environmental Conservation* **29**, 192–206 (2002).

[76] J. M. Ruiz, J. Romero, Effects of disturbances caused by coastal construc-tions on spatial structure, growth dynamics and photosynthesis of the seagrass Posidonia oceanica. *Marine Pollution Bulletin* **46**, 1523–1533 (2003).

[77] N. Marbà, *et al.*, Growth and population dynamics of Posidonia oceanica on the Spanish Mediterranean coast: elucidating seagrass decline. *Marine Ecology Progress Series* **137**, 203–213 (1996).

[78] N. Marbà, E. Díaz-Almela, C. M. Duarte, Mediterranean seagrass (Posidonia oceanica) loss between 1842 and 2009. *Biological Conservation* **176**, 183–190 (2014).

[79] L. Telesca, *et al.*, Seagrass meadows (Posidonia oceanica) distribution and trajectories of change. *Scientific Reports* **5**, 12505 (2015).

[80] L. Eriander, E. Infantes, M. Olofsson, J. L. Olsen, P. O. Moksnes, Assessing methods for restoration of eelgrass (Zostera marina L.) in a cold temperate re-gion. *Journal of Experimental Marine Biology and Ecology* **479**, 76–88 (2016).

[81] G. R. Bastyan, M. L. Cambridge, Transplantation as a method for restoring the seagrass Posidonia australis. *Estuarine, Coastal and Shelf Science* **79**, 289–299 (2008).

[82] J. Terrados, A. Marín, D. Celdrán, Use of Posidonia oceanica seedlings from beach-cast fruits for seagrass planting. *Botanica Marina* **56**, 185–195 (2013).

[83] M. M. van Katwijk, *et al.*, Global analysis of seagrass restoration: the impor-tance of large-scale planting. *Journal of Applied Ecology* **53**, 567–578 (2016).

[84] J. L. Sánchez-Lizaso, *et al.*, Salinity tolerance of the Mediterranean seagrass Posidonia oceanica: recommendations to minimize the impact of brine dis-charges from desalination plants. *Desalination* **221**, 602–607 (2008).

[85] O. Invers, J. Romero, M. Pérez, Effects of pH on seagrass photosynthesis: a laboratory and field assessment. *Aquatic Botany* **59**, 185–194 (1997).

[86] M. Ø. Pedersen, O. Serrano, M. Á. Mateo, M. Holmer, Temperature effects on decomposition of a Posidonia oceanica mat. *Aquatic Microbial Ecology* **65**, 169–182 (2011).

[87] E. Díaz-Almela, N. Marbà, R. Martínez, R. Santiago, C. M. Duarte, Seasonal dynamics of Posidonia oceanica in Magalluf bay (Mallorca, Spain): Temperature effects on seagrass mortality. *Limnology and Oceanography* **54**, 2170–2182 (2009).

[88] N. Marbà, C. M. Duarte, Mediterranean warming triggers seagrass (Posidonia oceanica) shoot mortality. *Global Change Biology* **16**, 2366–2375 (2010).

[89] C. M. Duarte, Seagrass depth limits. *Aquatic Botany* **40**, 363–377 (1991).

[90] T. Sintes, N. Marbà, C. M. Duarte, G. A. Kendrick, Nonlinear processes in seagrass colonisation explained by simple clonal growth rules. *Oikos* **108**, 165–175 (2005).

[91] N. Marbà, C. M. Duarte, Rhizome elongation and seagrass clonal growth. *Marine Ecology Progress Series* **174**, 269–280 (1998).

[92] G. A. Kendrick, N. Marbà, C. M. Duarte, Modelling formation of complex topography by the seagrass Posidonia oceanica. *Estuarine, Coastal and Shelf Science* **65**, 717–725 (2005).

[93] S. Journal, N. Jun, Growth rules in clonal plants and environmental predictability – A simulation study **82**, 341–351 (2018).

[94] T. Sintes, N. Marbà, C. M. Duarte, Modeling nonlinear seagrass clonal growth: Assessing the efficiency of space occupation across the seagrass flora. *Estuaries and Coasts* **29**, 72–80 (2006).

[95] S. Arnaud-Haond, *et al.*, Implications of extreme life span in clonal organisms: millenary clones in meadows of the threatened seagrass Posidonia oceanica. *PLoS ONE* **7**, e30454 (2012).

[96] C. M. Duarte, Submerged aquatic vegetation in relation to different nutrient regimes. *Ophelia* **41**, 87–112 (1995).

[97] C. M. Duarte, Temporal biomass variability and production/biomass relationships of seagrass communities. *Marine Ecology Progress Series* **51**, 269–276 (1989).

[98] C. M. Duarte, J. Kalff, Latitudinal influences on the depths of maximum colonization and maximum biomass of submerged angiosperms in lakes. *Canadian Journal of Fisheries and Aquatic Sciences* **44**, 1759–1764 (1987).

[99] D. G. Patriquin, "Migration" of blowouts in seagrass beds at Barbados and Carriacou, West Indies, and its ecological and geological implications. *Aquatic Botany* **1**, 163–189 (1975).

[100] J. L. Gutiérrez, *et al.*, *Physical ecosystem engineers and the functioning of estuaries and coasts*, vol. 7 (Elsevier Inc., 2011).

[101] M. S. Fonseca, M. A. R. Koehl, B. S. Kopp, Biomechanical factors contributing to self-organization in seagrass landscapes. *Journal of Experimental Marine Biology and Ecology* **340**, 227–246 (2007).

[102] C. Boström, E. L. Jackson, C. A. Simenstad, Seagrass landscapes and their effects on associated fauna: a review. *Estuarine, Coastal and shelf science* **68**, 383–403 (2006).

[103] C. D. Cornelisen, F. I. M. Thomas, Water flow enhances ammonium and nitrate uptake in a seagrass community. *Marine Ecology Progress Series* **312**, 1–13 (2006).

[104] S. Pigolotti, C. López, E. Hernández-García, K. H. Andersen, How Gaussian competition leads to lumpy or uniform species distributions. *Theoretical Ecology* **3**, 89–96 (2010).

[105] P. Colet, M. A. Matías, L. Gelens, D. Gomila, Formation of localized structures in bistable systems through nonlocal spatial coupling. I. General framework. *Physical Review E* **89**, 012914 (2014).

[106] L. Gelens, *et al.*, Formation of localized structures in bistable systems through nonlocal spatial coupling. II. the nonlocal Ginzburg-Landau equation. *Physical Review E* **89**, 12915 (2014).

[107] C. Fernandez-Oto, M. G. Clerc, D. Escaff, M. Tlidi, Strong nonlocal coupling stabilizes localized structures: an analysis based on front dynamics. *Physical Review Letters* **110**, 174101 (2013).

[108] S. Pigolotti, C. López, E. Hernández-García, Species clustering in competitive Lotka-Volterra models. *Physical Review Letters* **98**, 258101 (2007).

[109] R. Martínez-García, J. M. Calabrese, E. Hernández-García, C. López, Vegetation pattern formation in semiarid systems without facilitative mechanisms. *Geophysical Research Letters* **40**, 6143–6147 (2013).

[110] N. Akhmediev, A. Ankiewicz, *Dissipative solitons: From optics to biology and medicine* (Springer-Verlag, 2008).

[111] P. D. Woods, A. R. Champneys, Heteroclinic tangles and homoclinic snaking in the unfolding of a degenerate reversible Hamiltonian–Hopf bifurcation. *Physica D: Nonlinear Phenomena* **129**, 147–170 (1999).

[112] P. Coullet, C. Riera, C. Tresser, Stable static localized structures in one dimension. *Physical Review Letters* **84**, 3069–3072 (2000).

[113] J. H. Dawes, J. L. Williams, Localised pattern formation in a model for dryland vegetation. *Journal of Mathematical Biology* **73**, 63–90 (2016).

[114] J. Burke, E. Knobloch, Localized states in the generalized Swift-Hohenberg equation. *Physical Review E* **73**, 056211 (2006).

[115] O. Lejeune, M. Tlidi, A model for the explanation of vegetation stripes (tiger bush). *Journal of Vegetation Science* **10**, 201–208 (1999).

[116] A. J. Alvarez-Socorro, M. G. Clerc, G. González-Cortés, M. Wilson, Nonvariational mechanism of front propagation: Theory and experiments. *Physical Review E* **95**, 010202 (2017).

[117] F. Schönsberg, Pattern formation in clonal plants, Master thesis (2016).

[118] J. D. Murray, *Mathematical biology: I: An Introduction* (2004).

[119] P. Gandhi, *et al.*, Spatially localized structures in the Gray–Scott model. *Philosophical Transactions of the Royal Society A: Mathematical, Physical and Engineering Sciences* **376**, 20170375 (2018).

[120] Y. R. Zelnik, H. Uecker, U. Feudel, E. Meron, Desertification by front propagation? *Journal of Theoretical Biology* **418**, 27–35 (2017).

[121] A. Yochelis, Y. Tintut, L. L. Demer, A. Garfinkel, The formation of labyrinths, spots and stripe patterns in a biochemical approach to cardiovascular calcification. *New Journal of Physics* **10**, 055002 (2008).

[122] D. Wetzel, Tristability between stripes, up-hexagons, and down-hexagons and snaking bifurcation branches of spatial connections between up- and down-hexagons. *Physical Review E* **97**, 062221 (2018).

[123] E. Sheffer, H. Yizhaq, E. Gilad, M. Shachak, E. Meron, Why do plants in resource-deprived environments form rings? *Ecological Complexity* **4**, 192–200 (2007).

[124] Y. Pomeau, Front motion, metastability and subcritical bifurcations in hydrodynamics. *Physica D: Nonlinear Phenomena* **23**, 3–11 (1986).

[125] W. van Saarloos, Front propagation into unstable states. *Physics Reports* **386**, 29–222 (2003).

[126] W. van Saarloos, P. C. Hohenberg, Fronts, pulses, sources and sinks in generalized complex Ginzburg-Landau equations. *Physica D* **56**, 303–367 (1992).

[127] W. van Saarloos, Front propagation into unstable states: Marginal stability as a dynamical mechanism for velocity selection. *Physical Review A* **37**, 211–229 (1988).

[128] E. W. Koch, J. D. Ackerman, J. J. Verduin, M. van Keulen, *Seagrasses: Biology, ecology and conservation* (Springer, Dordrecht, 2006).

[129] T. M. Scanlon, K. K. Caylor, S. A. Levin, I. Rodriguez-Iturbe, Positive feedbacks promote power-law clustering on Kalahari vegetation. *Nature* **449**, 209–213 (2007).

[130] T. van der Heide, *et al.*, Ecosystem engineering by seagrasses interacts with grazing to shape an intertidal landscape. *PLoS ONE* **7**, e42060 (2012).

[131] J. de Fouw, *et al.*, A facultative mutualistic feedback enhances the stability of tropical intertidal seagrass beds. *Scientific Reports* **8**, 12988 (2018).

[132] N. Marbà, C. M. Duarte, Coupling of seagrass (Cymodocea nodosa) patch dynamics to subaqueous dune migration. *Journal of Ecology* **83**, 381–389 (1995).

[133] L. P. M. Lamers, *et al.*, Sulfide as a soil phytotoxin-a review. *Frontiers in plant science* **4**, 268 (2013).

[134] B. B. Jørgensen, The sulfur cycle of a coastal marine sediment (Limfjorden, Denmark). *Limnology and Oceanography* **22**, 814–832 (1977).

[135] M. L. Calleja, N. Marbà, C. M. Duarte, The relationship between seagrass (Posidonia oceanica) decline and sulfide porewater concentration in carbonate sediments. *Estuarine, Coastal and Shelf Science* **73**, 583–588 (2007).

[136] M. Holmer, C. M. Duarte, N. Marbà, Sulfur cycling and seagrass (Posidonia oceanica) status in carbonate sediments. *Biogeochemistry* **66**, 223–239 (2003).

[137] M. S. Frederiksen, M. Holmer, J. Borum, H. Kennedy, Temporal and spatial variation of sulfide invasion in eelgrass (Zostera marina) as reflected by its sulfur isotopic composition. *Limnology and Oceanography* **51**, 2308–2318 (2006).

[138] B. B. Jørgensen, Mineralization of organic matter in the sea bed—the role of sulphate reduction. *Nature* **296**, 643–645 (1982).

[139] O. Pedersen, T. Binzer, J. Borum, Sulphide intrusion in eelgrass (Zostera marina L.). *Plant, Cell and Environment* **27**, 595–602 (2004).

[140] M. Holmer, P. Storkholm, Sulphate reduction and sulphur cycling in lake sediments: a review. *Freshwater Biology* **46**, 431–451 (2001).

[141] M. Holmer, C. M. Duarte, N. Marbà, Iron additions reduce sulfate reduction rates and improve seagrass growth on organic-enriched carbonate sediments. *Ecosystems* **8**, 721–730 (2005).

[142] N. Marbà, *et al.*, Iron additions reduce sulfide intrusion and reverse seagrass (Posidonia oceanica) decline in carbonate sediments. *Ecosystems* **10**, 745–756 (2007).

[143] N. Marbà, *et al.*, Sedimentary iron inputs stimulate seagrass (Posidonia oceanica) population growth in carbonate sediments. *Estuarine, Coastal and Shelf Science* **76**, 710–713 (2008).

[144] M. S. Frederiksen, M. Holmer, E. Díaz-Almela, N. Marbà, C. M. Duarte, Sulfide invasion in the seagrass Posidonia oceanica at Mediterranean fish farms: assessment using stable sulfur isotopes. *Marine Ecology Progress Series* **345**, 93–104 (2007).

[145] M. Holmer, M. S. Frederiksen, Stimulation of sulfate reduction rates in Mediterranean fish farm sediments inhabited by the seagrass Posidonia oceanica. *Biogeochemistry* **85**, 169–184 (2007).

[146] M. Holmer, *et al.*, Sedimentation of organic matter from fish farms in oligotrophic Mediterranean assessed through bulk and stable isotope ($\delta13C$ and $\delta15N$) analyses. *Aquaculture* **262**, 268–280 (2007).

[147] M. Holmer, *et al.*, Effects of fish farm waste on Posidonia oceanica meadows: synthesis and provision of monitoring and management tools. *Marine Pollution Bulletin* **56**, 1618–1629 (2008).

[148] C. M. Duarte, C. L. Chiscano, Seagrass biomass and production: a reassessment. *Aquatic botany* **65**, 159–174 (1999).

[149] M. Holmer, E. J. Bondgaard, Photosynthetic and growth response of eelgrass to low oxygen and high sulfide concentrations during hypoxic events. *Aquatic Botany* **70**, 29–38 (2001).

[150] H. Höffle, M. S. Thomsen, M. Holmer, High mortality of Zostera marina under high temperature regimes but minor effects of the invasive macroalgae Gracilaria vermiculophylla. *Estuarine, Coastal and Shelf Science* **92**, 35–46 (2011).

[151] J. Realpe-Gomez, M. Baudena, T. Galla, A. J. McKane, M. Rietkerk, Demographic noise and resilience in a semi-arid ecosystem model. *Ecological Complexity* **15**, 97–108 (2013).

[152] P. Villa Martín, J. A. Bonachela, S. A. Levin, M. A. Muñoz, Eluding catastrophic shifts. *Proceedings of the National Academy of Sciences* **112**, E1828–E1836 (2015).

[153] R. Montagne, E. Hernández-García, A. Amengual, M. San Miguel, Wound-up phase turbulence in the complex Ginzburg-Landau equation. *Physical Review E* **56**, 151–167 (1997).

[154] U. Frisch, Viscoelastic behaviour of cellular solutions to the Kuramoto—Sivashinsky model. *Journal of Fluid Mechanics* **168**, 221–240 (1986).

[155] P. Parra-Rivas, Dynamics of dissipative localized structures in driven nonlinear optical cavities, Ph.D. thesis (2017).

[156] H. B. Keller, *Lectures on numerical methods in bifurcations problems* (Springer-Verlag, 1986).

[157] B. Krauskopf, H. M. Osinga, J. Galán-Vioque, *Numerical continuation methods for dynamical systems* (Springer, 2007).

[158] H. D. Mittelmann, A pseudo-arclength continuation method for nonlinear eigenvalue problems. *SIAM Journal on Numerical Analysis* **23**, 1007–1016 (1986).

[159] T. F. C. Chan, H. B. Keller, Arc-length continuation and multi-grid techniques for nonlinear elliptic eingenvalue problems. *SIAM Journal on Scientific and Statistical Computing* **3**, 173–194 (1982).